Universidade Federal do Ceará
Centro de Ciências
Departamento de Física
Programa de Pós-Graduação em Física

Tese de Doutorado

Electronic Transport in Molecular Systems

Aldilene Saraiva Souza

Fortaleza

July 2012

Universidade Federal do Ceará
Centro de Ciências
Programa de Pós-Graduação em Física

Electronic Transport in Molecular Systems

Aldilene Saraiva Souza

Thesis submitted to the Departament of Graduate Studies in Physics, in partial fulfillment of requirements for the degree of Doctor of Science.

Fortaleza

July 2012

Dados Internacionais de Catalogação na Publicação
Universidade Federal do Ceará
Biblioteca Universitária
Gerada automaticamente pelo módulo Catalog, mediante os dados fornecidos pelo(a) autor(a)

S713e Souza, Aldilene Saraiva.
Electronic transport in molecular systems / Aldilene Saraiva Souza. – 2012.
89 f. : il. color.

Tese (doutorado) – Universidade Federal do Ceará, Centro de Ciências, Programa de Pós-Graduação em Física , Fortaleza, 2012.
Orientação: Prof. Dr. Antonio Gomes de Souza Filho.
Coorientação: Prof. Dr. Mark A. Ratner.

1. Medidas via microscopia de tunelamento. 2. Transporte eletrônico de dispositivos moleculares. I. Título.

CDD 530

Universidade Federal da Ceará
Centro de Ciências
Programa de Curso de Pós-Graduação em Física

Electronic Transport in Molecular Systems

Aldilene Saraiva Souza

Examiners:

Professor Antonio Gomes de Souza Filho (Advisor-UFC)

Professor Mark A. Ratner (Advisor-Northwestern University, USA)

Professor Josué Mendes Filho (Inner member-UFC)

Profesor Humberto Terrones (External member-Penn State University, USA)

Professor Andréa Latgé (External member-UFF)

Professor Jordan Del Nero (External member-UFPA)

Fortaleza

July 2012

to my sister

Acknowledgements

Eu aprendi na sala de aula com pequeno grande senhor, dez anos atrás, que uma pessoa pra ter exito na vida precisa ter coragem, talento e sorte. Eu acredito sem reservas que sempre tive coragem e muita sorte. Coragem de ter deixado minha casa muito cedo e sorte de ter ao meu lado, sempre, pessoas muito especiais. Este é o lugar mais oportuno de agradecê-las.

Primeiramente, gostaria de agradecer meu orientador Professor Antonio Gomes pela oportunidade, conversas, direcionamento e paciência (muita paciêcia). Pela tranqüilidade, harmonia, sabedoria e amizade nos momentos mais difíceis desses anos, por me abrir portas e por me proporcionar uma família quando estive tão longe da minha, serei eternamente grata.

Agradecer também ao professor Mark Ratner, pela mavilhosa oportunidade de aprender coisas novas. Por me proporcionar um ambiente de trabalho caloroso sempre disposto a ouvir e incentivar mesmo as coisas mais simples.

Dizer ao meu querido e amado professor Josué Mendes Filho, que ele sempre esteve certo e agradecê-lo por deixar o chão seguro pra que eu pudesse caminhar, obrigada professor!

Ao meu amigo pra todas as horas e sempre professor Jordan Del Nero. Mesmo depois de dez anos de muitos altos e baixos sempre me ouviu. Obrigada pelos incentivos, conversas, puxões de orelha e paciência. Obrigada por estar lá no início e obrigada por estar agora no fim desta etapa.

Gostaria de agradecer também à dois grandes amigos e colaboradores, professor Fabricio Macêdo e Manuel Smeu que estiveram presente em momentos importantes e decisivos dos trabalhos que compõe esta tese, gostaria de dizer obrigada pelas longas conversas em problemas arduos e pela paciência com a minha incredulidade.

Obrigada também ao meu bom e querido amigo Sergio Vizeu que mesmo "longe do

meu lado" sempre foi meu fiel confidente.

Aos professores do departamento de Física (UFC) em especial ao professor Jeanlex pelas conversas e atenção.

Gostaria de agradecer também aos meus grandes amigos Arian Morais e Valdenir Silveira (macho) pelo apoio incondicional.

Aos velhos bem velhos amigos e irmãos lá do tempo da graduação mas que me acompanham até hoje, Ezequiel Belo, Thiago da Possa, Saulo Martins, Rudson Ferreira, Shirsley e Alessandre Sampaio. Aos velhos não tão velhos assim: Agmael Mendonça, Danila Tavares, Janilson, Saulo Davi (meu querido), Eduardo Girão (dudu), Acrisío Lins, Abraão Cefas, Vagner, Neudson, Gardenia e Erlania.

Às minhas amigas Katiane Pereira e Adriana Barros (bixas) pelas longas e agradáveis conversas, presença incondicional e confusões (sentirei saudades das confusões) foram muitos momentos especiais.

A minha querida amiga Rejane, pela ajuda, pela disposição em ajudar sempre, pela atenção e pelo carinho pra comigo. sentirei saudades!

Àqueles que ficaram lá na minha terrinha, Sergio Pereira (irmã), Jarlene e Wilde.

E por fim não menos importante mas sim todo o meu chão, meu ar, minha serenidade, meu motivo pra caminhar minha amada irmã Aucilene Saraiva, por tudo de bom, por existir na minha vida. Ainda bem que você vive comigo.

Minha amada mãe por ter me ensinado respeito para com os outros, por mostrar que honestidade é uma virtude e que perseverança é uma condição pra se manter de pé. te amo!

Aos meus filhos que sempre me trouxeram grande alegria: Kika (velha rabugenta), Lili (um doce), Gaveta (a promessa) e Pancinha (o terror em quatro patas).

À CAPES pelo suporte financeiro e ao Centro de Apoio de Auto Desempenho (CENPAD-SP).

Meus oito anos

Oh! que saudades que tenho
Da aurora da minha vida,
Da minha infância querida
Que os anos não trazem mais!
Que amor, que sonhos, que flores,
Naquelas tardes fagueiras
À sombra das bananeiras,
Debaixo dos laranjais!
Como são belos os dias
Do despontar da existência
Respira a alma inocência
Como perfumes a flor;
O mar é - lago sereno,
O céu - um manto azulado,
O mundo - um sonho dourado,
A vida - um hino d'amor!
Que aurora, que sol, que vida,
Que noites de melodia
Naquela doce alegria,
Naquele ingênuo folgar!
O céu bordado d'estrelas,
Oh! dias da minha infância!
Oh! meu céu de primavera!
Que doce a vida não era
Nessa risonha manhã!
Em vez das mágoas de agora,
Eu tinha nessas delícias
De minha mãe as carícias
E beijos de minha irmã!
Naqueles tempos ditosos
Trepava a tirar as mangas,
Achava o céu sempre lindo.
Adormecia sorrindo
E despertava a cantar!
Oh! que saudades que tenho
Da aurora da minha vida,
Da minha infância querida
Que os anos não trazem mais!
Que amor, que sonhos, que flores,
Naquelas tardes fagueiras
À sombra das bananeiras, Debaixo dos laranjais!
Casimiro de Abreu

Abstract

The thesis presents the treoretical studies of electronic transport in molecular devices for two different systems. Firstly we report a comparison between modeling and experimental current-voltage characteristics of self-assembled monolayers of 5-(4-pyridine)-1,3,4-oxadiazole-2-thiol (HPYT) and 5-(4-phenyl)-1,3,4-oxadiazole-2-thiol (HPOT) molecules deposited on Au (111). The formation of these self-assembled monolayers was confirmed by scanning tunneling microscopy (STM) measurements. DFT calculations were performed to obtain the most stable conformation of the molecular film. To compare with these results, STM images were calculated using a model based on a master equation technique. Striking similarity was found between the calculated and measured STM images, thus indicating the applicability of the model. From this comparison, we suggest that both HPYT and HPOT thiol molecules are attached to the Au surface by a bond between the sulfur and single gold atoms . A simple quantum model is proposed for describing the tunneling current along the molecular monolayer assembly on the Au(111) surface. Secondly we investigate spin transport properties in a junction composed of a polyacetylene chain bridging two zigzag graphene nanoribbon (ZGNRs) electrodes. The transport calculations are carried out using a non-equilibrium Green's function (NEGF) technique combined with density functional theory (DFT). Previous works have demonstrated that the ZGNRs exhibit a special antiferromagnetic (AF) ordering and half-metallicity at edge states, which can both be destroyed by applying a strong external electric field. Here we demonstrate that the connection between the molecular bridge and non-equivalent carbon atoms (A/B) in the graphene sublattice of ZGNRs may occur in two bonding arrangements and can produce metallic and semiconducting systems strongly dependent on the local coupling. By considering the carbon ring where the chain is linked, one connection resembles a *para*-linkage in benzene, whereas the other connection is similar to a *meta*-linkage. This results in different conductances for these configurations, which may be controlled by field-effect gating. Finally, the spin filter efficiency for these systems as a function of electric field is discussed. We also demonstrated that donor (D) and acceptor (A) groups attached to molecular bridge offer the possibility to modify the transmission probability of *para*-linkage and *meta*-linkage systems in a controlled way with a destructive quantum interference (QI) effective. In our calculation was demonstrated it is possible, for instance, by introducing the DA groups with magnetic properties and keep the spin polarized, such that spin-up and spin-down orbitals have different energies. This facilitates the construction of a spin valve that lets either spin-up or spin-down electrons to move while one is blocked.

Resumo

Nesta tese apresentamos o estudo teórico de transporte eletrônico de dispositivos moleculares em dois problemas distintos. No primeiro, comparamos medidas via microscopia de tunelamento (STM) com cálculos de primeiros princípios onde a tensão aplicada em uma mono camada de moléculas auto-montadas, denominadas: 5-(4-piridina)-1,3,4-oxadiazol-2-tiol (HPYT) e 5-(4-fenil)-1,3,4-oxadiazol-2-tiol (HPOT) mostram a distribuição local de carga. Essas moléculas são depositadas sobre um substrato de ouro tipo (111). A formação destas camadas moleculares foi confirmada por medidas de STM. Cálculos baseados na teoria do funcional da densidade (DFT) foram realizados para obter a conformação mais estável da interação molécula/substrato. Verificamos uma grande semelhança entre os resultdos teóricos e as medidas de imagem de STM. A partir desta comparação, sugerimos que o átomo de enxofre na molécula HPYT e HPOT está ligado à superfície de ouro por uma ligação direta à um único átomo de ouro. Para descrever a corrente de tunelamento ao longo da mono camada molecular sobre a superfície de Au (111) foi proposto um modelo quântico baseado na técnica de equação mestra. Nós investigamos também, propriedades de transporte de spin em uma cadeia de poliacetileno (como ponte) acoplada à uma nano fita de carbono tipo zigue-zague (ZGNRs) funcionando como eletrodos. Os cálculos de transporte foram efetuados usando técnica de funções de Green fora do equilíbrio (NEGF), combinada com a teoria do funcional da densidade (DFT). Trabalhos anteriores demonstraram que as ZGNRs exibem um ordenamento antiferromagnético (AF) e meia-metalicidade nos estados provenientes da borda, que podem ser destruídos com aplicação de um forte campo elétrico externo. Neste trabalho, nós demonstramos que a ligação entre a ponte molecular e átomos não-equivalentes de carbono (A/B) na sub rede de grafeno ZGNRs pode ocorrer de duas formas produzindo um sistema metálico ou semicondutor fortemente dependente do acoplamento local. Ao considerar o anel de carbono onde a cadeia está ligada, uma ligação se assemelha a uma ligação *para* no benzeno, enquanto a outra ligação é semelhante a uma ligação *meta*. Estas geometrias geram transmissão eletrônica distinta, que pode ser controlada sob um campo eletrico tranversal.

Contents

Introduction **1**

1 Electronic transport calculation methods **7**

1.1 Introduction 7

1.1.1 LCAO Hamiltonian Matrix Representation 8

1.1.2 Born-Oppenheimer Approximation 10

1.1.3 Density Functional Theory 11

1.1.4 Non-Equilibrium Green's Function (NEGF) Theory 18

1.1.5 The NEGF-DFT Method 24

2 Electronic properties of self-assembled arrays **29**

2.1 Introduction 29

2.2 Basic STM Theory 30

2.3 Atomic Geometry 33

2.3.1 Experiments 34

2.3.2 Electronic Structure Calculation 36

2.4 Experimental and Theoretical Images 38

2.5 Charge Transport 39

2.5.1 Electronic Transport 41

3 Electronic transport in conjugated chains **44**

3.1 Introduction 44

3.2 Lattice structure 44

3.3 The properties of graphene nanoribbon 49
3.4 ZGNRs and polyacetylene coupling 51
3.4.1 Computational details 52
3.4.2 The BC-P and BC-M systems 54
3.4.3 The spectrum of transmission 56

4 Electronic transport in conjugated chains with DA groups 62
4.1 Introduction 62
4.1.1 The donor/acceptor groups 66
4.1.2 Hybridization in PC-DA and M-DA 67
4.1.3 PC-DA and MC-DA organic devices 70

5 Conclusions 74

A Publication 77
A.1 List of papers included in the thesis 77
A.2 List of papers not included in the thesis 77

References 79

List of Figures

1.1 Comparison of the all-electron (solid black) and pseudo (dashed black) potential, along with the corresponding wave function [29]. 18

1.2 Flowchart of self-consistent solution of Kohn-Sham equations 19

1.3 Flowchart of DFT-NEGF 28

2.1 STM imaging modes. (a) constant current mode and (b) Constant height. 31

2.2 Schematics of the molecule ((a) HPOT and (b) HPYT) chemisorbed on the first atomic plane of the Au(111) surface, respectively. $R_0 \approx 0.51$nm is the distance between molecules which is similar for HPOT. Density of States (DOS) plots for HPOT and HPYT molecule in gas phase (black) and chemisorbed (red) are plot. The shift in Fermi energy is due mostly to image charge formation and strong coupling between molecule/metal. The color scheme for the atoms is: C (green), N (blue), O (red), H (white), S (dark yellow), Au (yellow) and tip (brown). 34

2.3 (a) Large scale STM image of HPYT on Au(111). Bias voltage (BV) 500 mV. Tunneling current of 5 pA. Image size: 100 x 100nm^2. (b) Low resolution STM image of HPOT. Bias voltage (BV) 500 mV. Tunneling current of 80 pA. Image size: 100 x 100nm^2. 35

2.4 The LDOS of the metal-molecule coupling reflects the spacial distribution of electronic states of the molecule on the electrode surface. (a) Unit cell used in the ab initio simulations showing the molecule sitting on top of the Au atom. The ab initio simulations are in good agreement with the actual measurements, but the assumed molecule position differs from current models. (b) The formation of an ordered monolayer on the surface providing parallel columns of molecules oriented orthogonally to the gold surface. Schematics of the molecule position (shaded circles) with respect to the Au atoms (open circles) as usually interpreted in the literature. In this model, the molecule sits on the three fold hollow site between Au atoms. In (c) and (d) for HPOT and HPYT respectively the profile shows the density of electrons on the atom in the molecule, covering the whole molecule with shading in the region of coupling Au-S. 37

2.5 (a) STM image of HPOT on Au(111), section profile. Bias Voltage (BV) 200 mV, Tunneling current of 100 pA. Image size: 8.0 x 8.0 nm^2 . (b) STM image of HPYT on Au(111), section profile. (BV) 500 mV, Tunneling current of 5 pA. Image size: 11.0 x 11.0 nm^2. Their respective LDOS ab initio simulations are shown in (c) and (d). The current and the image size for HPOT and HPYT are diferent due the termination, CH and N, respectively. 38

2.6 (a) Current through HPOT on Au(111) with section profile (Bias Voltage 200 mV) and tunneling current of 0.1 nA. (b) computed STM current HPOT, $x \approx 0.53$nm. (c) Current through HPYT on Au(111), section profile (Bias Voltage 500 mV) and tunneling current of 0.005 nA and (d) computed of the STM current of HPOT, $y \approx 0.56$nm. The molecules are sitting on Au(111) and the calculated currents were found using the transport model proposed in this work. 43

3.1 Honeycomb lattice for a single plane of grafhite. (a) Carbon atoms are located at each crossings and the lines indicate the chemical bonds, the length of the carbon-carbon bond is known to be 1.42Å , which are derived from sp^2-orbitals. Also shown are the primitive lattice vectors $\vec{a}_1$ and $\vec{a}_2$ und the unit-cell. There are two carbon atoms per unit-cell, denoted by A and B. (b) Reciprocal lattice of graphene with the Brillouin zone, $\vec{b}_1$ and $\vec{b}_1$ are the primitive lattice vectors. 45

3.2 Representation for honeycomb lattice where the x-axis produce the zigzag graphene nanorribon and y-axis produce a graphene armchair nanoribbon. 50

3.3 (a) Two-probe transport geometry. The central scattering region contains the polyacetylene bridge as well as several buffer layers of each electrode. The shaded regions include the two semi-infinite electrodes. Geometries showing (b) the connection of the polyacetylene bridge to ZGNR to make the BC-P (*para* / *ortho*-linkages) system and (c) the connection to form the BC-M (*meta*-linkage to both A and B atoms). A and B represent the different A/B sublattice carbon atoms. 53

3.4 Electronic band structure and projected density of states (arb. unit.) for (a) BC-P and (b) BC-M systems at zero electric field. The solid (dark blue) lines and solid (light red) lines denote spin-up and spin-down, respectively. Note the difference in the bands around the Fermi energy ($E_{\mathrm{F}} = 0$) in the BC-P and BC-M system. 55

3.5 Projected density of states for (a) BC-P and (b) BC-M systems under different electric fields. Both systems exposed to electric field exhibit large projections around the Fermi energy. Plots of spin density isosurfaces for the (c) BC-P and (d) BC-M systems. Note that there is a magnetic moment in the bridge, and that the different couplings change the ordering and the extent of the magnetization. The colors blue and red correspond to spin-up and spin-down (orbital contour value is 0.001). 57

3.6 The transmission spectra for two-probe systems. Solid lines show spin-up/down (blue/red) transmission through (a) BC-P and (b) BC-M connected to AF electrodes; and (c) BC-P and (d) BC-M connected to FM electrodes. Dotted show transmission through perfect ZGNR for comparison. 58

3.7 The scattering state wave functions for BC-P (I-IV) and BC-M (V-VI) systems. The selected energies correspond to the transmission peaks in 3.6. 59

3.8 Spin dependent transmission spectra under external electric field 0.0, 0.3 and 0.5 V/nm. (a) and (b) the BC-P system. (c) and (d) the BC-M system, for spin-up and spin-down, respectively. 61

4.1 Systematic two-probe transport geometry. The central scattering region contains the polyacetylene bridge as well as several buffer layers of each electrode with betaines gorups coupled on the bridge. The shaded regions include the two semi-infinite electrodes. Geometries showing (top) the connection of the polyacetylene bridge to ZGNR to make the PC-DA (*para* connection with donor (D) and acceptor (A) in the bridge) system and (bottom) the connection to form the MC-DA (*meta* connection with DA). . 65

4.2 A zwitterionic betaine molecule with an imidazol donor (D) and a pyridine acceptor (A) separated by alternating C=C bridge. 66

4.3 The BCP-DA (•) and BCM-DA (○) systems (left side). The charge accumulations for different parts (a) donor, (b) bridge and (c) acceptor. (d) The magnetic moment (μ_B) for DA groups and bridge. Both (charge and μ_B) as a function transverse of electric field. 68

4.4 Projected density of states for (a) PC-DA and (b) MC-DA systems under the transverse electric field (x-axis). The different parts of system are: 4-ZGNRs (dash-dot-dot), π-bridge (shot-dot), D (short-dash-dot green) and A (dash-dot black). The solid lines (positive and negative) represent the total DOS for spin-up and spin-down respectively. 69

4.5 Transmission spectrum as a function of energy and current as a function of voltage for the PC-DA and MC-DA. Spin-up and spin-down are represented in short-dash blue and solid line red respectively. 71

4.6 The transmission spectra for two-probe systems.(a) and (b) corre 72

List of Tables

2.1 Phenomenological parameters used in transport calculation. Energies in units of Γ_0. In the present system Γ_0 typically is around 1 eV. 42

3.1 The Spin Filter Efficiency (SFE) for BC-P and BC-M systems with electric field transverse the systems in x-axis. 61

Introduction

The field of molecular electronics has been characterized by the search for single molecule transistors and diodes that might possibly be a basis for a new electronics. Molecular devices promise to minimize size and power consumption and to enhance operation speeds [1]. However, technological applications of such devices are very far from becoming reality because fundamental questions including the thermal stability of devices and the nature of the metal-organic coupling are still not fully addressed. In particular, issues surrounding the contact to the molecular system and its effects on the electron transport properties require better understanding [2, 3]. Since the approach that started in the early seventies with a seminal theoretical study by Aviram and Ratner on current-voltage characteristics of a molecular rectifer, [4] the molecular electronics have shown that a molecular system, if properly designed, may perform a desired function in response to an applied electric field. In the begining, this idea was mostly just an amazing intellectual curiosity, but nowadays experimentalists have come up with several techniques that allow for simple studies of molecular electronic devices, besides reproductitly and scalability were not properly achived. One of the first such experiments was reported [5] for 1,4-benzene-dithiol that was chemically bonded between two gold electrodes like a two probe geometry. This experiment is a very simple approach, where there is just a single molecule between two gold electrodes. In practice, a device has three terminal as transistors and just a few experiments with such configurations have been used, with molecules ranging from being quite small to solid state systems such as carbon nanotubes, graphene and graphene nanoribbons. The experimental approaches have been helped by modeling resulting of the electron transport through molecular devices.

The studies from a quantum chemical point of view today are well established but in electronic transport there are some problems which deserve considerable attention. To describe the electron transport in this devices there is a lot of approaches [6, 7]. The best approach for electronic transport is based on the non-equilibrium Green's function combined with density functional theory (DFT) that treats the electrodes specifically as periodic layers of atoms. One crucial point that is often less properly described in these approaches is the effect of coupling at the molecule-metal interface. To understand that process it is important to not only capture the physics of the bulk electrodes, but also the chemistry that is present at the interfaces. Such studies where this problem is more elaborate shows that the chemical bond affects the I-V characteristics [8–10].

Experiments to address the problem of electronic transport can have some approaches. The break junction technique creates the metal electrodes by slowly pulling at both ends of a metal string until it breaks. This can be done in a solution to get the desired molecule to insert immediately in the gap that is formed, or by trying to get a molecule to bind to one of the contacts after the junction has been formed and then slowly move the two contacts closer and closer together until the bridging molecule binds in both ends and a signal is received [5, 11]. Other experimental way to address the problem of charge transport in single molecules is via scanning tunneling microscopy (STM). This technique can be a powerful candidate to build single molecule devices and it is a suitable tool to manipulate matter on a single atom scale. Besides the scalability is very limited in this method, it is extremely important for producing model devices. In this case, the first thing to notice is that there are no perfect surfaces, so it is necessary to find a reasonable approximation that captures the important chemistry and physics that takes place at the metal-molecule interface. The metal/organic coupling (chemisorption) suggests a shift in electronic energy levels, and it is extremely difficult in to define clearly a purely molecular energy level. In fact, the nature of the metal-organic contact and how the charge flows through the molecule between electrodes is complex, and the most appropriate way to

select which of the many different models best describe this interaction is to compare the theoretical predictions of the models with experimental results [12]. However, these challenges may be overcome by the use of organic materials such as a carbon nanotube, graphene and graphene nanoribbon in lieu of metal electrodes. The exceptional electronic properties of these materials might be a key to molecular electronic development.

Studies have showed that especially the graphene is uniquely material that is neither metallic nor semiconducting [13, 14]. The electronic and structure of graphene is unique and present two special momentum points in reciprocal space, called Dirac Point. Near the Dirac Point the electronic spectrum for graphene is linear, characteristic of massless particles such as photons. Otherwise, metal has a finite density of states at the Fermi energy, but the graphene's density of states vanishes at the Dirac points [15]. Graphene is not strictly a semiconductor, it is not strictly a metal and when is doped the Fermi energy is moved away from the Dirac point becoming metallic. Therefore the electrical current through graphene can never be turned off completly because the gap is zero. That problem can be solved by cutting graphene into a graphene nanorribon (GNR) [16]. The graphene nanoribbons are quite similar to carbon nanotubes (CNTs), which may be either metallic or semiconductor. The semiconducting band gap in CNTs varies inversely with the diameter of nanotube and in the case of GNRs, it is scale with inverse of the ribbon width (L) [17]. The properties of graphene nanorribon are extremely dependent of the edge. There are two basic types of graphene nanoribbons according to their edge configuration: armchair or zigzag. The armchair GNRs are either metallic or semiconducting, depending on its width L [16]. For example, when $L = 3n - 1$ (n is an integer), armchair GNR is metallic, otherwise it is semiconducting. Most notably, GNRs with zigzag edges are predicted to be antiferromagnetic (AF) semiconductors [17], where the polarized electron spins are ferromagnetically aligned along the ribbon edges and antiferromagnetically coupled between the two opposite edges. Such an amazing spin ordering can give rise to many unusual physical properties such as half metallicity [18], giant magnetoresistance

effect [19] and magnetoelectric effect [20], all of them openning avenues for promising applications.

It was shown that quite stable freestanding carbon chains can be connected to two graphene flakes [21, 22]. By employing energetic electron irradiation inside a transmission electron microscope two holes were created in a large graphene sheet. The resulting ribbon separating the two holes was carefully thinned by lower energy electrons until only the monoatomic chain remained. This structure is thus the realization of a unique system in terms of miniaturization, that is, an atomic chain contacted by the thinnest carbon leads instead of the usual case of metallic contacts. Calculations performed by density functional theory (DFT) predict that the zig-zag edge is the energetically most favorable structure for connecting the chain, in agreement with the experimental observations. Therefore, the study of the spin-dependent electronic transport properties of carbon chains connecting two graphene nanoribbon with the zig-zag edges is motivating and might be really interesting.

In this Thesis we worked in two different approach: we use the theoretical results to explain one possible erroneous interpretation of STM images in self assemble monolayers and metal surface. Due to the problems at coupling metal-organic mentioned above and amazing properties of ZGNRs, we study a chain of carbon coupled in ZGNRs as electrodes. The thesis is organized as follows. Chapter 1 presents the background for the theoretical calculation methods used in this work. It begins with the Schrödinger equation and the challenges involved in solving it. DFT is then introduced as an effective way to solve electronic structure problems. In one section we introduce the Landauer-Büttiker theory which describe electric current through a device as a sum of transmission probabilities. Finally, we describe the non-equilibrium Green's function (NEGF) formalism and how it can be used along with DFT.

Chapter 2 describes a comparison between model and experimental current-voltage characteristics of self-assembled monolayers of 5-(4-pyridine)-1,3,4-oxadiazole-2-thiol (HPYT)

and 5-(4-phenyl)-1,3,4-oxadiazole-2-thiol (HPOT) molecules deposited on Au (111). HPYT and HPOT are aromatic thiols that adsorb on gold and are able to lift the 22x$\sqrt{3}$ reconstruction, thus forming a slightly distorted $\sqrt{3}$x$\sqrt{3}$R30^o structure. The formation of these self-assembled monolayers was confirmed by scanning tunneling microscopy experiments. The STM images do not show clear distinction between the two molecules. The images were obtained with high tunneling resistance in order to avoid layer disruption. We use the STM tip to probe electron transport through periodic molecular arrays, and compare the experimental results with a DFT-based model for electron transport. The STM images of HPOT or HPYT adsorbed on gold surfaces were obtained at room temperature. To support the new interpretation, in addition to the DFT calculation of the system local density of states (LDOS), we develop a simple quantum transport model based on the master equation technique that reproduces the current along the surface measured via STM. We suppose that the HPOT and HPYT molecules are attached to the carbon atom by an S-Au bond and that the molecule is tilted relative to the gold surface giving the impression, in the STM measurements, that the molecules are sitting at the three fold hollow site.

Chapter 3 describes a study of spin-polarized transport properties of the molecular junction between polyacetylene and ZGNRs by performing calculations using NEGF technique combined with DFT. This system is a two-probe geometry with a central scattering region containing the molecular bridge and it is connected to the semi-infinite ZGNR electrodes. We focus in spin transport properties, which includes analysis of density spin polarization in different parts of the geometry under an external electric field. The spin degree of freedom of ZGNRs considering their possible application in spintronics, where it is essential to realize electron transport by using only one spin chanel. The half-metallicity in this material shows up when an external transverse electric field is applied. The critical electric field to achieve hal-metallicity decreases with the increase of ribbon width or with the strong electric field ($\vec{E}_{ext} > 0.7V/nm$). We control the width of the ribbon so that

stayed bridge close to edge in one system and in other just continued to be the edge. We control electric field also since our interest is to use the spin polarization at the edge on ZGNRs as prediction may lead to some important aplication of ZGNRs in spintronic as a swithes and spin filters.

Chapter 4 describes a study of donor (D) and accepor (A) groups attached to molecular bridge (C=C) offer the possibility to modify the transmission probability of BCP and BCA syestems in a controlled way. Whereas our study is under the bias in interval of [0.1,-1.0] V in a step of 0.1 V, performing a self-consistent calculation for each bias the systems are completly described. However, there is a strong correlation in the coupling between bridge and DA groups. The conjugation (π) are in general good candidates for exhibiting magnetic order, but in this DA system the magnetic properties are independent of the bridge length and for this groups of position and more importantly than this It is possible, for instance, to introduce the groups with magnetic properties and keep the spin polarized, such that up-spin and down-spin orbitals have different energies. This facilitates the construction of a spin valve that lets spin-up or spin-down electrons to move while one is blocking.

Chapter 1

Electronic transport calculation methods

1.1 Introduction

To model the transport system of interest a local atomic orbital basis is applied. One may represent, to relatively high accuracy, the electronic structure of a group of atoms through a linear combination of atomic orbitals (LCAO) based on DFT with the NEGF where the device leads and the scattering region are treated atomistically on equal footing. Such a NEGF-DFT technique has been widely used in analyzing nonlinear and non-equilibrium quantum transport in molecular electronics [23], and has been adapted to analyze spin-polarized quantum transport recently [24, 25]. The basic idea of the NEGF-DFT technique is to use DFT to calculate the Hamiltonian and electronic structure of a device, use NEGF to determine the non-equilibrium quantum statistics that is needed to populate the electronic structure during current flow, and use real space numerical methods to handle the transport boundary conditions. The NEGF-DFT method provides an useful alternative and supplements other atomistic techniques for analyzing electronic transport and spin-polarized quantum transport. The main advantage of the NEGF-DFT formalism is its close proximity to modern many body theory and quantum transport theory which are largely based on Green's functions. As such, new effects and new transport physics can be readily implemented into the NEGF-DFT software tool.

1.1.1 LCAO Hamiltonian Matrix Representation

The matrix representation of the single electron time independent is described by the Hamiltonian, $\vec{H}$, and atomic orbitals in central real space on all atoms in the system is the wave function [26]. Being ψ_i is an eigenstate, the Schrödinger equation of the system is,

$$\hat{H}|\psi_i\rangle = E|\psi_i\rangle. \tag{1.1-1}$$

Any eigenstate can be represented by a linear combination of local atomic orbitals $|\psi_i\rangle$,

$$|\psi_i\rangle = \sum_j c_{ij}|\phi_j\rangle, \tag{1.1-2}$$

where the $|\phi_i\rangle$ is the atomic orbital representation so that,

$$\hat{H}\left(\sum_j c_{ij}|\phi_j\rangle\right) = E_i\left(\sum_j c_{ij}|\phi_j\rangle\right). \tag{1.1-3}$$

Atomic orbitals on diffrent atomic sites are non-ortogonal and Eq. 1.1-3 can be written in matrix form as:

$$\begin{bmatrix} H_{00} & H_{01} & \dots & H_{0N} \\ H_{10} & H_{11} & \dots & H_{1N} \\ \vdots & \vdots & \ddots & \vdots \\ H_{N0} & H_{N1} & \dots & H_{NN} \end{bmatrix}\begin{bmatrix} c_{i0} \\ c_{i1} \\ \vdots \\ c_{iN} \end{bmatrix} = E_i \begin{bmatrix} S_{00} & S_{01} & \dots & S_{0N} \\ S_{10} & S_{11} & \dots & S_{1N} \\ \vdots & \vdots & \ddots & \vdots \\ S_{N0} & S_{N1} & \dots & S_{NN} \end{bmatrix}\begin{bmatrix} c_{i0} \\ c_{i1} \\ \vdots \\ c_{iN} \end{bmatrix}. \tag{1.1-4}$$

The Schrödinger equation (Eq.1.1-1) describes the space and time-dependence of quantum mechanical systems. Once defined for a particular system, its solution contains all the information about that system. The treatment used in this work deals with the non-relativistic time-independent Schrödinger equation. The Hamiltonian is then written as

$$\hat{H} = \hat{T}_e + \hat{V}_{eN} + \hat{U} + \hat{T}_N + \hat{T}_{NN}, \tag{1.1-5}$$

Where the kinetic energy of the electrons is given as,

$$\hat{T}_e = -\frac{1}{2}\sum_i \nabla_i^2, \tag{1.1-6}$$

where the summation runs over all electrons i and ∇ is the derivative operator in space coordinates. The Coulombic electron-nucleus attraction is given as,

$$\hat{V}_{eN} = -\sum_{i,n} \frac{Z_n}{|\vec{r}_i - \vec{R}_n|}, \tag{1.1-7}$$

where the summation runs over all electrons and nuclei pairs. Z_n and $\vec{R}_n$ are, respectively, the atomic number and coordinates for nucleus n; and $\vec{r}_i$ are the coordinates for electron i. The Coulombic electron-electron repulsion is given as,

$$U = \frac{1}{2} \sum_{i \neq j} \frac{1}{|\vec{r}_i - \vec{r}_j|}, \tag{1.1-8}$$

where the summation runs over all electron pairs (the factor 1/2 is added to compensate for each pair being included twice). The kinetic energy of the nuclei is given as,

$$\hat{T}_N = -\sum_n \frac{1}{2M_n} \nabla_n^2, \tag{1.1-9}$$

where the summation runs over all nuclei and M_n is the mass of nucleus n. The Coulombic nucleus-nucleus repulsion is given as,

$$\hat{V}_{NN} = \frac{1}{2} \sum_{n \neq m} \frac{Z_{nm}}{|\vec{R}_n - \vec{R}_m|}, \tag{1.1-10}$$

where the summation runs over all nucleus pairs. Z_n and Z_m are the charges and $\vec{R}_n$ and $\vec{R}_m$ are the coordinates for nuclei n and m, respectively. Eq.1.1-1 is a many-body problem that cannot be solved exactly for more than one electron. For this reason, many approximations are made to reduce this to a problem that can be solved numerically. Some of these approximations are outlined below. The Hamiltonian of the system is the observable corresponding to the total energy E of the system and it is given as a sum of the kinetic energy of the electrons, the Coulombic electron-nucleus attraction, the Coulombic electron-electron repulsion, the kinetic energy of the nuclei, and the Coulombic nucleus-nucleus repulsion.

1.1.2 Born-Oppenheimer Approximation

The Born-Oppenheimer approximation (or adiabatic approximation) simplifies the Schrödinger equation with the assumption that the nuclei can be treated as being stationary relative to the motion of the electrons. This is valid for most practical materials research problems because the mass of a nucleus is much greater than the mass of an electron. It is also assumed that the electrons will instantaneously relax with respect to the positions of the nuclei whose effect can be included as an external field $\hat{V}_{ext}$. Within the Born-Oppenheimer approximation, Eq.1.1-1 can be separated into an electronic and a nuclear part, and the latter is treated independently. The kinetic and potential energies of the nuclei can be added after the electronic Schrödinger equation has been solved. The Schrödinger equation can now be written as,

$$\hat{H}_{elec}|\psi\rangle_{elec} = \left[\hat{T}_e + \hat{U} + \hat{V}_{ext}\right]|\psi\rangle_{elec} = E_{elec}|\psi\rangle_{elec}, \tag{1.1-11}$$

where the subscript elec is included as a reminder that this is not the full Schrödinger equation. $\hat{T}_T$ and $\hat{V}_{NN}$ are removed and $\hat{V}_{eN}$ is replaced with $\hat{V}_{ext}$ to emphasize that the electrons move under the influence of the nuclei as through an external field. From here on, the subscript it elec will be omited, but the following discussion about the Schrödinger equation does refer to Eq.1.1-11. The difficulty in solving the Schrödinger equation stems from the fact that it is a many-body problem when the system has more than one electron. The reason for this is because the motion of an electron is not independent of other electrons; that is, they are correlated and for some systems strongly correlated. One aspect of this correlation is accounted for by the Pauli's exclusion principle which states that no two electrons of the same spin can occupy the same state at the same time. More generally, this is known as the antisymmetry principle which states that the wave function must change sign when any two electrons are interchanged. The difficult part of electron-electron interactions is to deal with the correlation of electrons of opposing spins. This is the central challenge in electronic structure calculations. Density functional theory is one method that is commonly used in calculations that take these interactions into account

in an approximate manner.

1.1.3 Density Functional Theory

The Hamiltonian of a stationary system of N interacting spin-1/2 particles is used to obtain the central object that is the electronic density $\rho(\vec{r})$. The Kohn-Shan spin-density functional theory (KS-DFT) [29] is given by:

$$E[n^{\alpha\beta}(r)] = T_s[n^{\alpha\beta}(r)] + \frac{e^2}{2}\int\int \frac{n(r)n(r')}{|r-r'|}drdr' + \sum_{\alpha\beta}\int V_{ext}^{\alpha\beta}(r)n^{\alpha\beta}dr \quad (1.1\text{-}12)$$

which is the sum of the kinetic energy T_S of non-interacting electrons, the electron-electron interaction in the Hartree approximation, the interaction energy with the external potential $V_{ext}^{\alpha\beta}$ and the exchange-correlation energy. The external potential $V_{ext}^{\alpha\beta}$ is described by the Coulomb potential of the nuclei. The functional (Eq. 1.1-12) is obtained by inserting the ground-state spin density matrix and yields the ground-state energy. The variation of Eq. 1.1-12 with respect to $\rho^{\alpha\beta}(\vec{r})$ cannot be performed directly, since the explicit form of the density functional $T_S[\rho^{\alpha\beta}(\vec{r})]$ is not know. The solution for this problem is using wave functions (orbitals) of single-particle $\varphi_i^{\alpha}(r)$, which allow to write the kinetic energy functional $T_S[\rho^{\alpha\beta}(\vec{r})]$ and spin-density matrix $\rho^{\alpha\beta}(\vec{r})$ as

$$T_S[\rho^{\alpha\beta}(r)] = \sum_{\alpha i}\int \varphi_i^{*\alpha}(\vec{r})\left(-\frac{\hbar^2}{2m}\nabla_{\vec{r}}^2\varphi_i^{\alpha}(\vec{r})\right)dr \quad (1.1\text{-}13)$$

and

$$\rho^{\alpha\beta}(\vec{r}) = \sum_i \varphi_i^{*\alpha}(\vec{r})\varphi_i^{\beta}(\vec{r}), \quad (1.1\text{-}14)$$

respectively,with the sum over i including all occupied orbitals. The last two equations provide an implicit representation of the kinetic energy in terms of the spin-density matrix. The minimum of Eq.1.1-12 can now be found by variation of $E[\rho^{\alpha\beta}]$ with respect to the single particle wavefunction. This leads to the Kohn-Sham equations:

$$-\frac{\hbar^2}{2m}\nabla_{\vec{r}}^2\varphi_i^{\alpha}(\vec{r}) + \sum_{\beta} V_{eff}^{\alpha\beta}(\vec{r})\varphi_i^{\beta}(\vec{r}) = \epsilon_i\varphi_i^{\alpha}(\vec{r}), \quad (1.1\text{-}15)$$

where the ϵ_i stand for Lagrange parameters, which guarantee that the wavefunctions are normalized as $\sum_\alpha(\varphi_i^\alpha, \varphi_i^\alpha) = 1$. The potential $V_{eff}^{\alpha\beta}$, which is defined as

$$V_{eff}^{\alpha\beta}(\vec{r}) = \delta^{\alpha\beta}e^2 \int \frac{\rho(\vec{r}^{'})}{\mid \vec{r} - \vec{r}^{'} \mid} \, d\vec{r}^{'} + V_{ext}^{\alpha\beta}(\vec{r}) + V_{xc}^{\alpha\beta}(\vec{r}), \tag{1.1-16}$$

stands for an effective one-particle potential. Useful approximations for the exchange-correlation energy functional can be given in terms of the eigenvalues $\rho^+(\vec{r})$ and $\rho^-(\vec{r})$ of the density matrix $\rho^{\alpha\beta}(\vec{r})$. This matrix can be diagonalized as

$$\sum_{\alpha^{'}\beta^{'}} U^{\alpha\alpha^{'}}(\vec{r}) \; \rho^{\alpha^{'}\beta^{'}}(\vec{r}) U^{\beta\beta^{'}}(\vec{r}) = \delta^{\alpha\beta}\rho^\alpha(\vec{r}), \tag{1.1-17}$$

where $U^{\alpha\beta}(\vec{r})$ are spin-1/2 rotation matrices and $\rho^\alpha(\vec{r})$ the eigenvalues. In terms of the spin up and down orbitals $\varphi_i^+(\vec{r})$ and $\varphi_i^-(\vec{r})$, the spin densities $\rho^+(\vec{r})$ and $\rho^-(\vec{r})$ can be represent

$$\rho^\pm(\vec{r}) = \sum_i |\varphi_i^\pm(\vec{r})|^2. \tag{1.1-18}$$

The Kohn-Sham Eq.1.1-15 for orbitals can be written as

$$\left[-\frac{\hbar^2}{2m}\nabla_{\vec{r}}^2 + V_{eff}^\pm(\vec{r}) \right] \varphi_i^\pm(\vec{r}) = \varepsilon_i^\pm(\vec{r}) \tag{1.1-19}$$

with the effective potential bling

$$V_{eff}^\pm(\vec{r}) = e^2 \int \frac{\rho^{'}}{\mid \vec{r} - \vec{r}^{'} \mid} d^{'}\vec{r} + V_{ext}^\pm + V_{xc}^\pm, \tag{1.1-20}$$

where $V_{xc}^\pm$ is the exchange-correlation functional and $V_{ext}^\pm$ is any external potential (electric field, magnetic field, etc...) including the pseudopotential that defines the atomic core and the applied bias potential that drives current flow. We have also introduced the exchange-correlation potential

$$V_{xc}^\pm(\vec{r}) = \frac{\delta E_{xc}[\rho^+(\vec{r}), \rho^-(\vec{r})]}{\delta\rho^\pm(\vec{r})}. \tag{1.1-21}$$

The spin-density-functional theory presented above is exact in principle. The strength of DFT lies in the fact that the interacting many-electron problem has been reduced to a

set of KS equations involving non-interacting electrons moving in the effective potential of the other electrons. Furthermore, this mapping is exact provided that the exact exchange-correlation functional is known. In principle, the exact exchange-correlation functional is far too complicated to ever express in a closed form, and therefore approximations must be used. However the functionals E_{xc} and $V_{xc}^{\pm}$, in which all complication of the many electrons system are hidden, are not know and must be approximated. Useful approximation like the local-spin-density aproximation (LSDA), wich depends locally on the spin densities, and the generalized gradient approximation (GGA), which also depends on the gradients os the spin densities.

Local Spin Density Approximation (LSDA)

The simplest approximation to the exchange-correlation functional is the local density approximation (LDA) [32, 33], in which one approximates the non-classical corrections to the energy with the energy density of a homogeneous electron gas. The LDA assumes that the exchange-correlation energy at a position r in an electron gas can be approximated by the exchange-correlation energy in a homogeneous electron gas, ϵ_{xc}^{0} having the same density as the electron gas at position r:

$$E_{xc}^{LDA}[\rho(\vec{r})] = \int \epsilon_{xc}^{0}[\rho(\vec{r})]\rho(\vec{r})d\vec{r}. \tag{1.1-22}$$

The energy density is typically calculated for high and low density limits and interpolated as a function of the density $\rho(\vec{r})$.

The calculation begins with a trial electron density. The KS Hamiltonian is calculated within a chosen basis set using this density. The Hamiltonian is then diagonalized to calculate the eigenvalues and eigenvectors of the system. A new electron density is calculated by populating the eigenvectors according to a Fermi distribution in energy:

$$\rho(\vec{r}) = \sum_{i} f(\epsilon_i, \mu)|\varphi_i(\vec{r})|^{2}, \tag{1.1-23}$$

where μ is the chemical potential of the system and chosen such that the total system has a natural charge. Once a new electron density is calculated, the cycle is repeated

until self-consistency is achieved. It is critical to point out that Fermi-Dirac statistics are only valid for systems at thermal equilibrium. In magnetic systems or, in general, in systems where open electronic shells are involved, better approximations to the exchange-correlation functional can be obtained by introducing the two spin densities, $\rho^{\alpha}(\vec{r})$ and $\rho^{\beta}(\vec{r})$, such that $\rho(\vec{r}) = \rho^{\alpha}(\vec{r}) + \rho^{\beta}(\vec{r})$. The non-interacting kinetic energy splits trivially into spin up and spin down contributions, and the external and Haetree potential depend on the full density $\rho(\vec{r})$, but the approximate xc functional- even if the exact functional should depend only on $\rho(\vec{r})$- will depend on both spin densities independently, $E_{xc} = E_{xc}[\rho(\vec{r}) = \rho^{\alpha}(\vec{r}), \rho^{\beta}(\vec{r})]$. KS equations then read exactly as in Eq.1.1-15, but the effective potential $V_{eff}(\vec{r})$ now acquires a spin index:

$$V_{eff}^{\alpha} = V(\vec{r}) + \int \frac{\rho(\vec{r}')}{\mid \vec{r} - \vec{r}' \mid} \, d\vec{r}' + \frac{\delta E_{xc}[\rho^{\alpha}(\vec{r}), \rho^{\beta}(\vec{r})]}{\delta n^{\alpha}(r)}, \tag{1.1-24}$$

and

$$V_{eff}^{\beta} = V(r) + \int \frac{n(r')}{\mid r - r' \mid} \, dr' + \frac{\delta E_{xc}[n^{\alpha}(r), n^{\beta}(r)]}{\delta n^{\beta}(r)}, \tag{1.1-25}$$

The density given by Eq.1.1-18 contains summation over the spin state. The latter have to be determined according to the single-particle eigenvalues, by asking for lowest $\rho = \rho^{\alpha} + \rho^{\beta}$ to be occupied. This defines a Fermi energy E_F such that the occupied eigenstates have $E_{i,spin} < E_F$.

In the case of non-magnetic system, $\rho^{\alpha}(\vec{r}) = \rho^{\beta}(\vec{r})$, and everything reduces to the simple case of double occupancy of the single-particle orbitals. The equivalent of the LDA in spin-polarized systems is the *local spin density approximation* (LSDA), which basically consists of replacing the xc energy density with a spin-polarized expression:

$$E_{xc}^{LSDA}[\rho^{\alpha}(\vec{r}), \rho^{\beta}(\vec{r})] = \int [\rho^{\alpha}(\vec{r}) + \rho^{\beta}(\vec{r})] \epsilon_{xc}[\rho^{\alpha}(\vec{r}) + \rho^{\beta}(\vec{r})] d\vec{r}. \tag{1.1-26}$$

Generalized-gradient approximation (GGA)

The exchange-correlation energy has a gradient expansion of the type:

$$\begin{aligned} E_{xc}^{GGA}[\rho^{\alpha},\rho^{\beta}] &= \int d^3\vec{r}\ \rho(\vec{r})\epsilon_{xc}(\rho^{\alpha}\rho^{\beta},|\nabla\rho^{\alpha}|,|\nabla\rho^{\beta}|,...) \\ &\equiv \int d^3\vec{r}\ \rho(\vec{r})\epsilon_{xc}F_{xc}(\rho^{\alpha}\rho^{\beta},|\nabla\rho^{\alpha}|,|\nabla\rho^{\beta}|,...) \end{aligned} \tag{1.1-27}$$

where the functional F_{xc} is to satisfy a number of formal conditions for the exchange-correlation role, such as sum rules, long-range decay and so on. This cannot be done by considering directly the bare gradient expansion. What is needed from the functional is a form that mimics a re-summation to infinite order, and this is the main idea behind the GGA.

Basis Sets

In order to obtain numerical solutions to the Kohn-Sham equations, a set of basis functions must be employed to efficiently expand the electronic wave functions. For molecular systems, the basis tends to be localized in real space. A common approach is to use basis functions that resemble atomic orbitals in order to construct wave functions for the system as a linear combination of atomic orbitals (LCAO). The wave functions can either be analytic or numerical.

For the analytic approach, Gaussian functions are very popular. The Gaussian function, centered at $\overrightarrow{R}_A$, has the form

$$\phi^{GF}(\alpha,\vec{r},\vec{R}_A) = \left(\frac{2\alpha}{\pi}\right)^{\frac{3}{4}}\ e^{-\alpha|\vec{r}-\vec{R}_A|}, \tag{1.1-28}$$

where α is the Gaussian orbital exponent. Gaussian functions are commonly used because they possess the property that the product of two Gaussians is also a Gaussian, which can be exploited to greatly reduce the time it takes to evaluate two-electron integrals [26]. Since a Gaussian function is not an adequate representation of an atomic orbital, a contraction (linear combination) of Gaussian functions or "primitives" is used to represent

the atomic orbital

$$\phi(\vec{r}, \vec{R}_A) = \sum_{p=1}^{L} d_p \, \phi_p^{GF}(\alpha_p, r - \vec{R}_A), \tag{1.1-29}$$

with L being the length of the contraction and d_p is a contraction coefficient [26].

A common notation for representing basis sets in chemistry is X-YZG; for example, 6-31G(d) and 3-21G are often used. X is the number of primitive Gaussians (Eq.1.1-29) making up each core atomic orbital basis function, while Y and Z each represents the number of basis functions making up each valence orbital. Therefore, it represents a double-ζ (split-valence) basis set with the first one being composed of Y primitive Gaussians and the second one being composed of Z primitive Gaussians. The (d) in 6-31G(d) represents the addition of a polarization function, meaning an auxiliary function with one additional node (d-type function added to a basis set with p-orbitals valence). These ingredients add more flexibility within the basis set.

In the numerical representation, the orbitals used are similar to atomic orbitals with the exception that a potential is used to eliminate the long range tails of the orbital function [29], and the orbital is localized nearby the nucleus. The wave function is expanded on a mesh of points in real space. Although some information is lost by discretizing the wave function in this manner, accurate results can be obtained by using a sufficiently fine grid [28]. However, this will always be at the expense of computing speed. The greatest advantage of the grid-based approach is that the molecular orbitals (MOs) that are represented on the grid have a higher flexibility to take their proper values. The accuracy of the grid-based MOs is only limited by the grid spacing, while the analytic basis function method depends on the number and type of functions in a less straightforward way [29].

For periodic systems, the above procedure is not feasible because an infinite number of atomic orbitals would be required. Instead, a supercell approach is used where only a single repeating cell of the periodic system is considered. Bloch's theorem states that in a periodic solid each wave function can be written as the product of a wave-like part and

a cell periodic part f_i [30].

$$\varphi_i(\vec{r}) = e^{[i\vec{k}.\vec{r}]} f_i(\vec{r}), \tag{1.1-30}$$

where $\vec{k}$ is a vector in k-space (the reciprocal space of the periodic lattice) and $\vec{r}$ is a vector in real space. The cell-periodic part of the wave function can be expressed as an expansion of a set of plane waves whose wave vectors are reciprocal lattice vectors of the crystal [29],

$$f_i(\vec{r}) = \sum_{\vec{G}} c_{i\vec{G}}\ e^{[i\vec{G}.\vec{r}]} \tag{1.1-31}$$

where $\vec{G}$ is a reciprocal lattice vector defined by $\vec{G}.\vec{l} = 2\pi m$ with $\vec{l}$ being a lattice vector of the crystal and m is an integer. Therefore, with the use of Bloch's theorem, each wave function φ_i can be represented as a sum of plane waves [31]

$$\varphi_i = \sum_{\vec{G}} c_{i,\vec{k}+\vec{G}}\ e^{[i(\vec{k}+\vec{G}).\vec{r}]}. \tag{1.1-32}$$

The number of plane waves is infinite but an energy cutoff is introduced to reduce their number to a finite value. The sampling is then done at the k-points that are in the Brillouin zone [31]. The accuracy can always be improved by increasing this cutoff energy.

Pseudopotentials

As atoms come together to form a solid or a molecule, the core electrons will only interact weakly with other atoms. It is the valence electrons that strongly participate in bonding. In the pseudopotential (PS) approximation, the properties of a system are determined by the valence electrons while the core electrons do not participate. In other words, the total external potential of the all-electron atom, including the nuclear core and the core electrons, is replaced by a smooth, non-singular potential (the PS), which acts only on the valence electrons [29]. This greatly reduces the number of electrons for which the Kohn-Sham equations need to be solved and this is especially significant for metallic atoms which have a large number of core electrons. In constructing the pseudopotential,

several criteria need to be met. (1) the pseudopotential radial wave function needs to match the all-electron wave function outside a cutoff radius, r_c. (2) There should be no radial nodes in the pseudopotential wave function inside, r_c. (3) The wave function must be norm-conserving, thus meaning that the core charge should be the same for the pseudo and the all-electron wave functions. Figure1.1 illustrates the pseudopotential compared to the all-electron potential, and their corresponding wave functions.

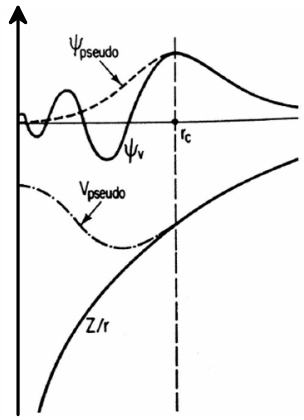

Figure 1.1: Comparison of the all-electron (solid black) and pseudo (dashed black) potential, along with the corresponding wave function [29].

Furthermore, the equations are derived using the variational principle and therefore only valid for the ground-state energy of a system. Note that the effective potential of Kohn-Sham is from 1.1-24 depends of $\rho(\vec{r})$ that consequently depends on $V_s(\vec{r})$??.

After convergence the postprocessing generates: Bandstructure, (P)DOS, population analysis, etc. Electron transport is neither a ground-state nor an equilibrium problem, and hence an accurate study of electron transport must go beyond standard DFT by correctly treating the non-equilibrium and non-ground state nature of the system. The non-equilibrium Green's function formalism is a powerful framework that can be used to address these problems.

1.1.4 Non-Equilibrium Green's Function (NEGF) Theory

Since the original development by L. V. Keldysh [34] and L. Kadanok and G. Baym [35]. The non-equilibrium Green's functions is an amazing theory applied to electron

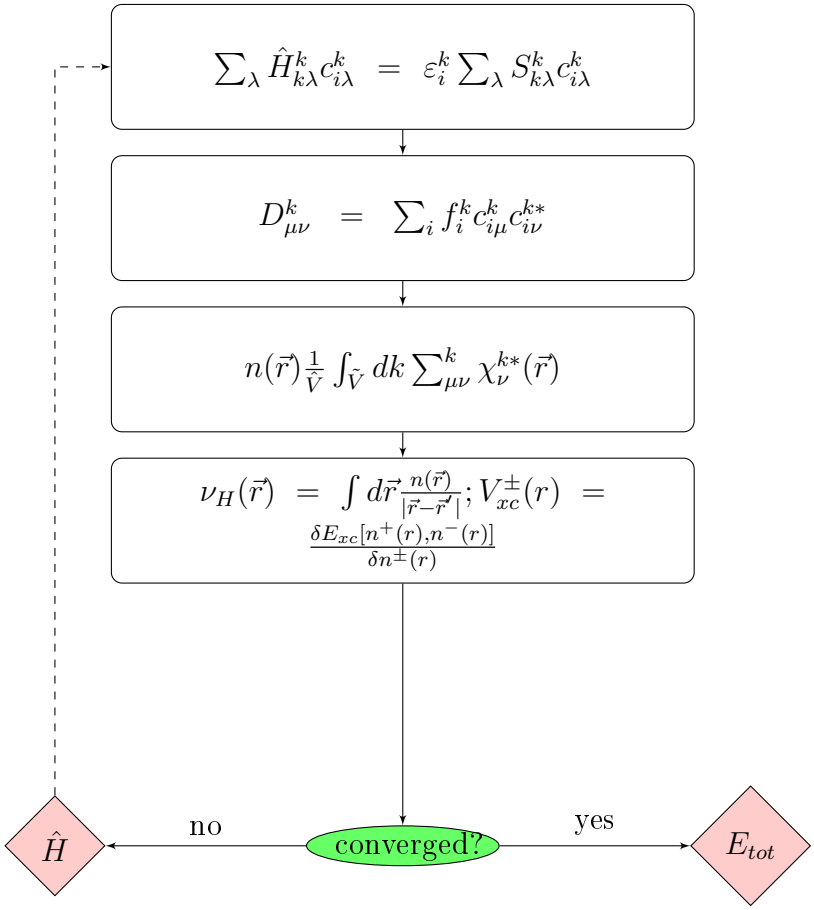

Figure 1.2: Flowchart of self-consistent solution of Kohn-Sham equations

transport. The transmission properties of a given system sandwiched between leads, namely to the probability for electrons "cross" the system in going from one lead to the other. The first concept that scatterers can induce, self-consistently, local fields which "act-back" on the carrier dynamics was pointed out by Landauer [36–39]. A common approach for measuring the conductance of a material is by connecting it to two metallic contacts to which a bias is applied, thereby inducing a current to pass through the material. If the sample is of macroscopic dimensions with length L and cross sectional area A, the conductance is given by

$$G = \frac{\sigma A}{L}, \tag{1.1-33}$$

where σ is the electrical conductivity of the material. If the length is reduced, the conductance in Eq.1.1-33 should increase proportionally. However, experiments have found that the conductance approaches a limiting value (or a multiple of it) $G_0 = \frac{2e^2}{h}$ [6] once the length is smaller than a certain value. Conductors of such dimensions belong to the mesoscopic regime.

An object is considered to be in the mesoscopic regime if L is smaller than certain characteristic length scales. These include the (inelastic) mean free path L_m, which is the distance the electron travels before its initial momentum is lost and the phase relaxation length L_ϕ, which is the distance that an electron travels before its initial phase is lost [6]. These length scales can vary widely for different materials and they are also dependent on factors such as temperature and magnetic field. For this reason, mesoscopic transport phenomena have been observed for dimensions ranging from a few nanometers to hundreds of microns [40]. There are different approaches that might be employed to formulate the transport problems [7]. Here we will briefly discuss about the formulation answering an important question about how to describe a transport problem. In this section we outline the key results of the NEGF theory and after we will shown very briefly how to combine DFT+NEGF.

The Hamiltonian for the non-equilibrium system is:

$$\hat{H}_T = h + \hat{H}^{'}(t), \tag{1.1-34}$$

where h is the time-independent Hamiltonian that describe the particle-free H_0 and the many-body interaction $\hat{H}^i$ as the electro-electron interaction. Where the h is a equilibrium term that does not generate charge flux. $\hat{H}^{'}(t)$ is a non-equilibrium time-dependent term and can be an electric field, light excitation and coupling between leads with different chemical potential. In particular, in this thesis this term is a transmission function. $\hat{H}^{'}$ is activated in t_0, i.e, for $t < t_0$ the $\hat{H}^{'} = 0$ ($\hat{H}_T = h$). Usually in steady-state $t \longrightarrow \infty$.

The equilibrium density matrix is given by

$$\rho_0 = \frac{e^{-\eta h}}{\mathrm{Tr}(e^{-\eta h})}, \tag{1.1-35}$$

where η is related to the temperature by $\eta = 1/(k_B T)$ and Tr is the trace of matrix which is a sum over a complete basis of states:

$$Tr \equiv \sum \langle i, t_0 | ... | i, t_0 \rangle. \tag{1.1-36}$$

Two-probe Formulation

A general system consisting of a central scattering region connected by two leads is said to be in a two-probe geometry. The Hamiltonian for this system can be generally expressed as:

$$\hat{H} = \hat{H}_{L/R} + \hat{H}_{scatt} + \hat{H}_{hib}, \tag{1.1-37}$$

where $\hat{H}_{L/R}$ is the Hamiltonian of the left (L) and right (R) leads:

$$\hat{H}_{L/R} = \sum_k \ \varepsilon_k \ c^{\dagger}_{k,L/R} c_{k,L/R}, \tag{1.1-38}$$

where $c^{\dagger}_{k,L/R}$ is a creation operator. Here $\varepsilon_k = \varepsilon^0_k + qV_{L/R}$ where ε^0_k are the energy levels in the left/right leads and $V_{L/R}$ is the external voltage. The $\hat{H}_{scatt}$ term is the Hamiltonian of the central scattering region.

$$\hat{H}_{scatt} = \sum_{\rho} (\varepsilon_\rho + q \ U_\rho) \ \ d^{\dagger}_{\rho} d, \tag{1.1-39}$$

where $d_n^\dagger$ creates an electron in the central scattering region. The term U_ρ is the Self-energy Coulomb potential of the scattering region which within the mean-field approximation,

$$U_\rho = \sum V_{nm} \langle d_m^\dagger d_m \rangle \tag{1.1-40}$$

where V_{nm} is the matrix element of Hartree and exchange-correlation potential. In the real space the Hartree potential is given by $V(\vec{r}, \vec{r}^{\,\prime}) = q/|\ \vec{r} - \vec{r}^{\,\prime}\,|$.

The $\hat{H}_{hib}$ describes the coupling between the scattering region and the left/right leads respectively, being written as

$$\hat{H}_{hib} = \sum_{kn} [t\ c_{kL}^\dagger d_n + t^* d_n^\dagger c_{kL} + t c_{kR}^\dagger d + t^* d_n^\dagger c_{kR}], \tag{1.1-41}$$

where ε_k and ε_n are the leads and scattering levels, respectively, t is the coupling constant.

In practice, $\hat{H}$ is usually calculated self-consistently. Once an $\hat{H}$ is determined, one may calculate the transmission coefficient by using the Landauer-Buttiker equation [7].

$$T(\varepsilon) = Tr[\Gamma_L(\varepsilon - qV_L) G^r(\varepsilon) \Gamma_R(\varepsilon - qV_R) G^a(\varepsilon)]. \tag{1.1-42}$$

Here, G^r and G^a are the retarded and advanced Green's functions of the central scattering:

$$G^{r,a}(\varepsilon) = \frac{1}{\varepsilon I - H_{hib} - \sum_L^{r,a}(\varepsilon) - \sum_R^{r,a}(\varepsilon) \pm E^+}. \tag{1.1-43}$$

where $E^+ = \lim_{\eta \to 0} + E + i\eta$ is the energy plus an infinitesimal imaginary part. The effect of the leads on the central scattering is included through the self-energy terms $\sum_L^{r,a}(\varepsilon)$ and $\sum_R^{r,a}(\varepsilon)$, which are calculated from the surface Green's function of the leads:

$$\Sigma_L^r(\varepsilon) = \hat{H}_{hib} (\varepsilon I - \hat{H}_L)^{-1} \hat{H}_{hib}^\dagger, \tag{1.1-44}$$

$$\Sigma_R^r(\varepsilon) = \hat{H}_{hib} (\varepsilon I - \hat{H}_R)^{-1} \hat{H}_{hib}^\dagger. \tag{1.1-45}$$

The terms $\Gamma_{L/R}$ in Eq.1.1-42 are defined as

$$\Gamma_{L/R}(\varepsilon - qV_{L/R}) = i(\Sigma^r_{L/R}(\varepsilon) - \Sigma^a_{L/R}(\varepsilon)). \tag{1.1-46}$$

The important result of NEGF theory is that under non-equilibrium conditions the density of matrix of the scattering region, ρ, is given by:

$$\rho = \frac{i}{2\pi}\int_{-\infty}^{+\infty} G^<(\varepsilon)\, d\varepsilon, \tag{1.1-47}$$

where $G^<(\varepsilon)$ is calculated using the Keldysh equation:

$$G^<(\varepsilon) = G^r(\varepsilon)\Sigma^<(\varepsilon), \tag{1.1-48}$$

and

$$\Sigma^<(\varepsilon) = i\Gamma_L(\varepsilon - qV_L)f_\alpha(\varepsilon - \mu_L) + i\Gamma_R(\varepsilon - qV_R)f_\alpha(\varepsilon - \mu_R). \tag{1.1-49}$$

The $f_{L/R}$ is the Fermi distribution,

$$f_{L/R}(\varepsilon) = \frac{1}{e^{(E-\mu_{L/R})/kT}+1}, \tag{1.1-50}$$

and the electrochemical potential difference between left and right electrodes is $eV = \mu_L - \mu_R$.

The power of NEGF lies in the fact that Eq.1.1-47 correctly includes all information about the non-equilibrium quantum statistics of the device, which are in general not described by Fermi-Dirac. Hence the NEGF framework provides an unique advantage over standard DFT calculations in that it applies to transport calculations where systems are intrinsically under non-equilibrium conditions. The combined use of NEGF with DFT is a powerful method that draws upon the advantages of both techniques. In such a calculation, the electronic structure of a device is calculated within DFT, and NEGF is used to determine the non-equilibrium quantum statistics that are needed to populate the electronic structure during current flow.

1.1.5 The NEGF-DFT Method

Traditionally, DFT was limited to two classes of problems at equilibrium: finite systems such as an isolated molecule and periodic systems such as a perfect solid. An electronic device is however neither finite nor periodic, and is typically operating under nonequilibrium conditions. It is not finite because a device must connect to electrodes and interact with an environment involving infinite number of degrees of freedom; it is not periodic because devices have no translational symmetry; it is a nonequilibrium problem because external bias voltages drive a current flow. These issues must be solved for any viable nanoelectronic device theory and modelling method. The general device where two semi-infinite electrodes sandwich a central scattering region. The device is x-y periodic such that the left and right electrodes are fully 3D in a half plane. It is important to note that for magnetic systems, 3D leads are necessary in order to correctly describe both the surface and bulk magnetism. When applied to molecular spintronic systems involving a single molecule as tunnel barrier, the central scattering region must contain enough vacuum so that images of the molecule do not interact. Along the transport direction (z-axis), the two leads extend to reservoirs at $z = \pm\infty$ The central scattering region is chosen sufficiently large in the z-direction such that: I) the potentials outside the central region are taken as equivalent to bulk and II) the matrix elements coupling the left and right leads are zero. The electrochemical potentials of the left and right electrodes, μ_L and μ_R, are given by the bulk Fermi level that can be calculated by DFT at equilibrium, and the applied external bias voltage.

Because the device is x-y periodic, the eigenstates of the system can be labeled according to their transverse momentum:

$$\psi^k(R+r) = e^{ik}.R \times \ e^{ik}.r\phi^k(r). \tag{1.1-51}$$

where k is a Block wave vector, $R = n_x\hat{a} + n_y\hat{b}$ is a lattice vector, and ϕ^k s the x-y periodic Bloch function. Using the Bloch ansatz, the Schrödinger equation can be written

in matrix form as:

$$\tilde{H}^k \phi^k = E \tilde{S}^k \phi^k, \tag{1.1-52}$$

where $\tilde{H}^k$ is the folded Hamiltonian defined as

$$\tilde{H}^k = \sum_{n_x, n_y} H_{n_x, n_y} \, e^{ik \, \cdot \, R}, \tag{1.1-53}$$

and the overlap matrix $\tilde{S}^k$, which has been included because we are assuming a non orthogonal basis set, is defined analogously to Eq.1.1-53. In this equation, $\hat{H}_{n_x,n_y}$ is the Hamiltonian matrix connecting two unit cells separated by R. It is important to note that these matrices correspond to the entire device and therefore are infinite in dimension.

At the heart of the NEGF-DFT formalism [23] is the Keldysh Green's functions which are required for the calculation of electron density matrix at non-equilibrium and transport properties of the system. Analogous to Eq.1.1-43, the finite part of the retarded Green's function in k-space corresponding to the L-C-R (left, central, and right) region of the device is given by:

$$G_k^r(\epsilon) = \begin{pmatrix} \epsilon I - \tilde{H}_L^k - \epsilon \tilde{S}_L^k + \Sigma_L^k(\epsilon) & \tilde{V}_L^k - \epsilon \tilde{S}_{CL}^k & 0 \\ (\tilde{V}_L^k - \epsilon \tilde{S}_{CL}^k)^\dagger & \epsilon I - \tilde{H}_C^k - \epsilon \tilde{S}_C^k & \tilde{V}_R^k - \epsilon \tilde{S}_{CR}^k \\ 0 & (\tilde{V}_R^k - \epsilon \tilde{S}_{CR}^k)^\dagger & \epsilon I - \tilde{H}_R^k - \epsilon \tilde{S}_R^k + \Sigma_R^k(\epsilon) \end{pmatrix}^{-1}$$

where I is the identity matrix, $\tilde{H}_L^k$, $\tilde{H}_R^k$ and $\tilde{H}_C^k$ are the finite sub-matrices of $\tilde{H}^k$ corresponding to the L, R and C regions, respectively. $\tilde{S}_{CL}^k$ and $\tilde{S}_{CR}^k$ are the finite sub-matrices of $\tilde{S}^k$ connecting the C region to the L and R regions, respectively. $\tilde{V}_L^k$ ($\tilde{V}_R^k$) are the finite sub-matrices connecting the L(R) and C regions. The coupling of the L and R to the remaining part of the semi-infinite electrodes is fully taken into account by the self-energies, Σ_L^k and Σ_R^k. It is important to note the distinction between H_L, the Hamiltonian of the unit cell of the left lead and is *finite* in dimension compared to H_{ll}, the Hamiltonian of the entire lead used in the last section which has *infinite* dimension.

To analyse spin-polarized transport, the matrices above have been extended into spin-space. Each matrix element in the non-spin formalism [23] becomes a two-by-two matrix

which specifies spin-up, spin-down, and the connection between the two spin spaces [41]:

$$H_{ij} = \begin{pmatrix} H_{ij,\uparrow\uparrow} & H_{ij,\uparrow\downarrow} \\ H_{ij,\downarrow\uparrow} & H_{ij,\downarrow\downarrow} \end{pmatrix} . \tag{1.1-54}$$

There is no restriction of spin collinearity, hence the left and right leads (and possibly any other part of the system) can have arbitrary relative magnetic orientation. The example applications in this thesis are restricted to spin collinear systems.

The Hamiltonian of each region is calculated self-consistently within DFT by solving the Kohn-Sham equation [42]. A flowchart illustrating a self-consistent NEGF-DFT calculation is shown in Fig.1.2. The spin-dependent exchange-correlation potential is treated at the local spin density approximation (LSDA) level where one distinguishes spin-up (ρ^{α}) and spin-down (ρ^{β}) density is given by $\rho = \rho^{\alpha} + \rho^{\beta}$.

The central scattering region includes enough layers of lead atoms, the electronic structure of the left and right regions can be safely considered as that of bulk, which can be calculated with a super-cell DFT analysis. In other words, in $G_k^r(\epsilon)$ the upper and lower parts of the Hamiltonian $\tilde{H}_L^k + \tilde{H}_R^k$ corresponding to the left and right electrodes, are calculated as isolated bulk material whose electron density is given by 1.1-23 using the Fermi-Dirac distribution we have assumed that the left and right ferromagnetic leads are in equilibrium contact with their corresponding reservoirs, as is well established in the Landauer-Büttiker transport formulation [39]. The Hamiltonian of the left (right) region is obtained by a separate calculation where the left (right) region is taken as the unit cell of a fully period bulk system, and hence will have the magnetic properties of a bulk system. The k-dependent retarded self-energies of each lead, Σ_L^k, Σ_R^k are determined using the recursion method of periodic systems In constructing the self-energies and potential matrices for each lead, the reference spin direction is rotated to specify the relative spin orientation.

The remaining parts of the Hamiltonian in $G_k^r(\epsilon)$ are for the central region: $\tilde{V}_L^k$, $\tilde{V}_R^k$ and $\tilde{H}_C^k$ that are calculated self-consistently using the non-equilibrium electron density

matrix [23]. The non-equilibrium density matrix is calculated by integrating over the 2D (in x-y direction) Brillouin zone (BZ) for contributions of each transverse Bloch state:

$$\rho = \int_{BZ} dk\ \rho_k, \tag{1.1-55}$$

Where density matrix ρ_k is constricted using the non-equilibrium Green's function $G_k^<$:

$$\rho_k = -\frac{i}{2\pi}\int_{-\infty}^{\infty} d\epsilon G_k^<(\epsilon). \tag{1.1-56}$$

Here $G_k^<$ is calculated using the Keldysh equation:

$$G_k^< = G_k^a \Sigma_k^< G_k^a \tag{1.1-57}$$

where $G_k^a = (G_k^r)^\dagger$ is the advanced Green's function. Within a mean field type theory such as DFT, the lesser self-energy $\Sigma_k^<$ is given by a linear combination of the Fermi-Dirac functions of the two leads [6]. The term of $\Sigma_k^<(\epsilon) = i\Gamma_{L,k}(\epsilon)f(\epsilon-\mu_L + i\Gamma_R, k(\epsilon)f(\epsilon-\mu_R)$, where the linewidth functions of left and right leads are related to the retarded self-energies, for instance $\Gamma_{L,k} = \frac{i}{2}[\Gamma_{L,}^k - (\Gamma_{L,}^k)^\dagger]$.

Finally, the spin currents (spin-polarized charge currents) are calculated by integrating the contributions from each transverse Bloch state using the Landauer formula. In this work we are interesting just in transmission at zero bias $T(E, V = 0$:

$$I_\sigma = \frac{q}{h}\int_{BZ} dk \int d\epsilon[f(\epsilon-\mu_L - f(\epsilon-\mu_R)]T_\sigma(\epsilon, k), \tag{1.1-58}$$

where the k resolved transmission coefficient for a particular spin, σ, is given by

$$T_\sigma(E, V) = \mathrm{Tr}[\Gamma_{L,\sigma}(\epsilon)G_\sigma^a(\epsilon)\Gamma_{R,\sigma}G_\sigma^r(\epsilon)], \tag{1.1-59}$$

where the trace is taken over orbital space. Note that each quantity in the right hand side is defined in spin-space 1.1-54. The diagram represent this process, is shown in Fig. 1.3.

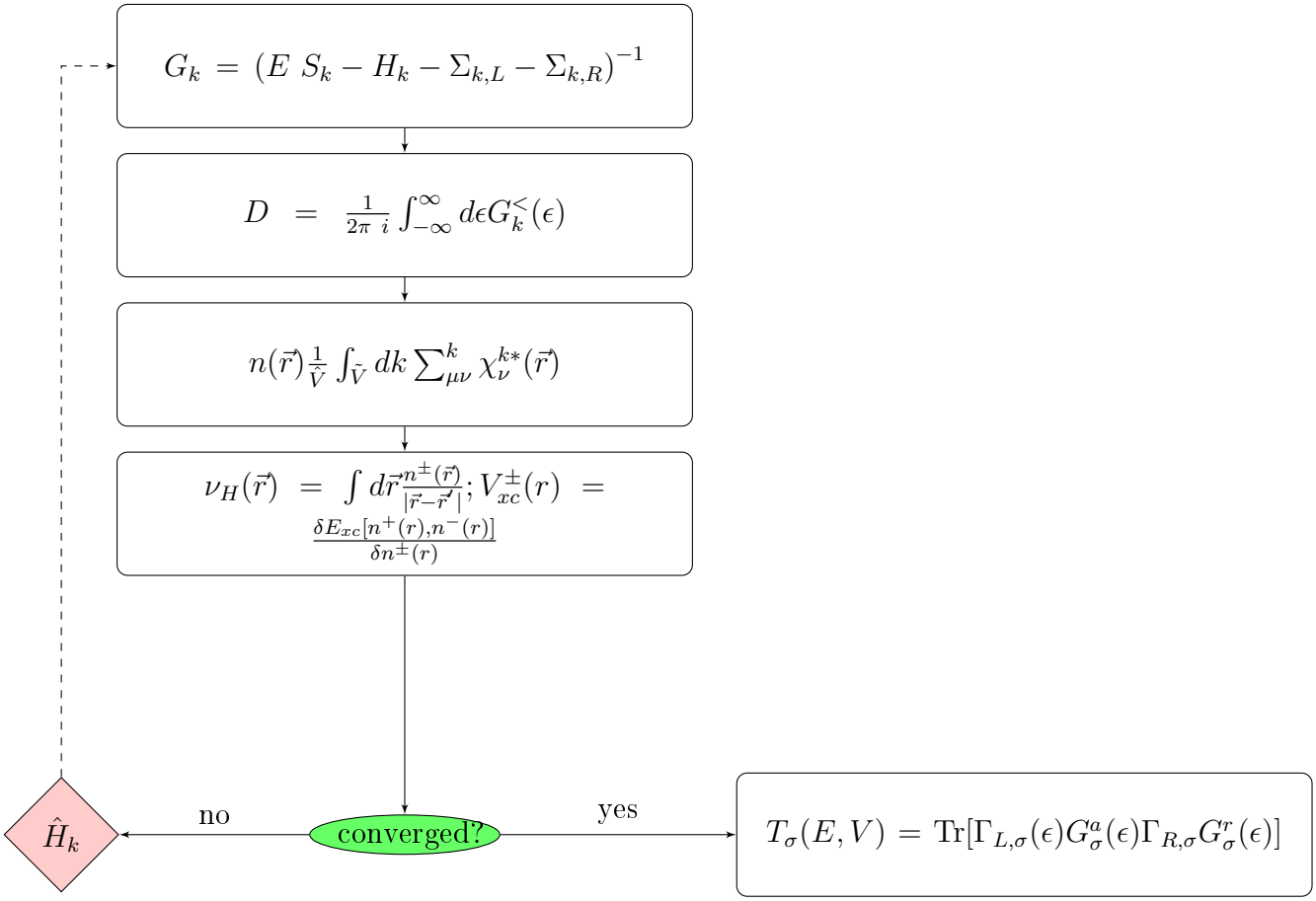

Figure 1.3: Flowchart of DFT-NEGF

Chapter 2

Electronic properties of self-assembled arrays

2.1 Introduction

When molecules interact with metallic electrodes, the system conductance is strongly dependent on many variables, such as surface charge distribution, chemical composition and the molecule-metal coupling, which is responsible for charge transfer and reflection effects [47, 86–89]. Charge transport can also be affected by strong Coulomb interaction and electronic hopping involving frontier orbitals [48]. In fact, the nature of the metal-organic contact and how the charge flows through the molecule between electrodes is complex, and the most appropriate way to select which of the many different models best describes this interaction is to compare the theoretical predictions of the models with experimental results [12]. One experimental way to address the problem of charge transport in single molecules is via scanning tunnelling microscopy (STM). STM can be a powerful candidate to build single molecule devices and it is a powerful tool to manipulate matter on a single atom scale [49]. The STM has been an indispensable scientific tool since its inception at IBM Zurich in 1982 [50]. This work focuses upon theoretical modeling we use the STM tip to probe electron transport through periodic molecular arrays, and compare the experimental results with a DFT-based model for electron transport considering a single molecule interacting with the tip.

2.2 Basic STM Theory

In essence the scanning tunneling microscope operates by setting a very sharp metallic tip in close proximity to a surface and applying a voltage difference between the tip and surface. The distance between the tip and surface is not very large (d $\approx$ several Å) and the bias voltage is small. The current is very much dependent upon the distance between the surface and the tip, with detectible variations in surface height on the order of 0.1 Å [51]. The STM can be operated in either the constant-current mode or the constant-height mode. In the first of two STM image generation methods, the tip moves up and down (z-axis) across a surface (xy-axis) at constant tunnelling current and as it passes across the surface can reading atomic corrugations in the sample (2.1(a)). Additionally, this mode allows to measure the height differences between various surface features. This leads to a height variation and thus the image comes from the tip topography across the sample and gives a constant charge density surface; this means contrast on the image is due to variations in charge density. Alternatively, in the constant-height mode (2.1(b)) the voltage and height are both held constant while the current changes to keep the voltage from changing; this leads to an image made of current changes over the surface, which can be related to charge density. The benefit to using a constant height mode is that it is faster, as the piezoelectric movements require more time to register the change in constant current mode than the voltage response in constant height mode.

The tunnelling effects originates from the wavelike properties of the particles. In quantum mechanics the one-dimensional time-independent Schrödinger equation is defined as

$$-\frac{\hbar^2}{2m}\frac{d^2}{dz^2}\psi(z) + U(z)\psi(z) = E\psi(z). \tag{2.2-1}$$

If one considers a free electron incident against a square potential, the solution to Eq.2.2-1 is

$$\psi(z) = \psi(0)\ e^{\pm ikz}, \tag{2.2-2}$$

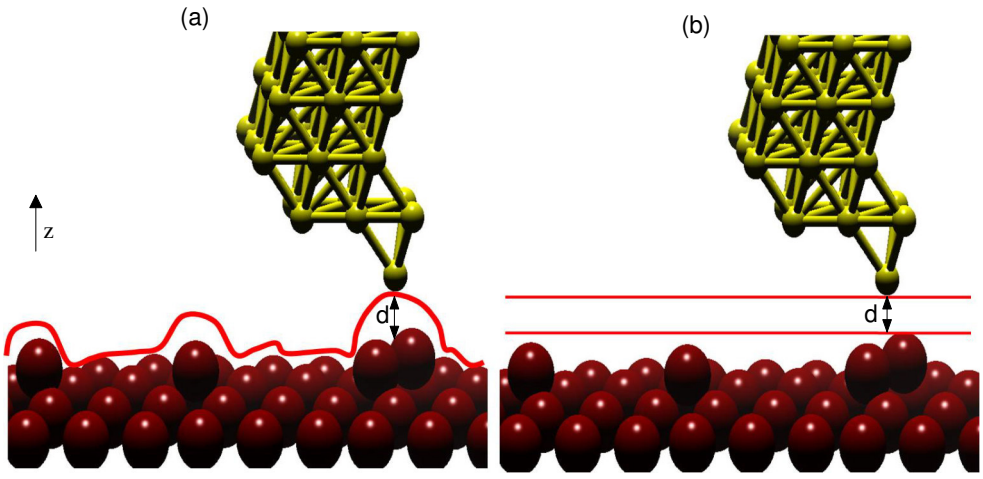

Figure 2.1: STM imaging modes. (a) constant current mode and (b) Constant height.

for $E > U$, where

$$k = \frac{\sqrt{2m(E-U)}}{\hbar}. \tag{2.2-3}$$

For $E < U$ the electron is no longer free but may tunnel through barrier U. The solution to Eq.2.2-1 for an electron traveling in the z-direction then becomes

$$\psi(z) = \psi(0)\ e^{-kz}, \tag{2.2-4}$$

where

$$k = \frac{\sqrt{2m(E-U)}}{\hbar}. \tag{2.2-5}$$

represents the decay of an incident electron wavefunction into the barrier. There is a finite probability of the electron residing on the other side of the barrier given by $|\psi|^2\ e^{-2kz}$. For a condensed matter system we define μ_S and μ_{tip} to be the electrochemical potentials of the sample and STM tip, respectively. At equilibrium these two electrochemical potentials are equal and no current flows. An electron in the sample will tunnel to the tip through a vacuum barrier when a voltage is applied and there is a non-equilibrium difference between μ_S and μ_{tip}. If the vacuum barrier height is defined as ϕ and has width W, then the probability of state ψ_n in the sample tunneling into the tip is proportional to

$$p \propto |\psi_n(0)|^2\ e^{-2kW}, \tag{2.2-6}$$

and,

$$k = \frac{\sqrt{2m\phi}}{\hbar}. \tag{2.2-7}$$

A summation over all electrons tunneling from the surface to the tip provides the total tunneling current and is limited to the energy range exposed by the applied voltage V. An occupied state in the sample may only tunnel into an unoccupied state in the tip and vice- versa. The current therefore is proportional to a summation over all occupied states tunneling between μ_S and μ_{tip}

$$I \propto \sum_{E_n=\mu_{tip}}^{\mu_S} |\psi_n(0)|^2 \; e^{-2kW}. \tag{2.2-8}$$

By using a feedback loop the tip is vertically adjusted in such a way that the current always stays constant. As the current is proportional to the local density of states (LDOS), the tip follows a contour of a constant density of states during scanning. A kind of a topographic image of the surface is generated by recording the vertical position of the tip. The local density of states (LDOS) at energy E on the sample is a three dimensional quantity defined as

$$\rho_S(x, y, z, E) = \frac{1}{\epsilon} \sum_{E_n=\mu_{tip}-\epsilon}^{\mu_S} |\psi_n(x, y, z)|^2, \tag{2.2-9}$$

which has units of electrons per unit volume per unit energy. Under low bias conditions, such as 50 meV, suitable to this simplified STM model, the LDOS may be regarded to be constant around the sample electrochemical potential leading to a simplified expression for the tunneling current

$$I(x, y) \propto V \rho_S(x, y, 0, \mu_S) \; e^{-2kW}. \tag{2.2-10}$$

We consider the LDOS at $z = 0$. The LDOS varies with the electron cloud around individual surface atoms and therefore so does the tunneling current, thereby giving rise to STM images in the (x,y) plane. The Tersoff-Hamann approximation [52], arrives though a more rigorous arguments, to

$$I(x, y) \propto \sum_{E_n=\mu_{tip}-\epsilon}^{\mu_S} |\psi_n(x, y, z = W)|^2, \tag{2.2-11}$$

which states that the current is proportional to the sum over the surface LDOS in the bias range at the tip apex atom position $z = W$.

2.3 Atomic Geometry

In our work we use the STM tip to probe electron transport through periodic molecular arrays, and compare the experimental results with a DFT-based model for electron transport. The DFT work is based on a B3LYP hybrid functional with DZP basis set and GGA approximation and TM pseudopotentials. Two similar molecular systems are investigated, namely, 5-(4-phenyl)-1,3,4-oxadiazole-2-thiol (HPOT) and 5-(4-pyridine)-1,3,4-oxadiazole-2-thiol (HPYT). In each case, the molecules are adsorbed on a A_u (111) surface deposited on mica. The computed density of states of the isolated HPOT and HPYT molecule in gas phase is shown in Fig.2.2 (a and b).

The metal/organic coupling (chemisorbed) in this case suggests a shift in electronic energy levels, and it is difficult to define clearly a purely molecular energy level (Fig.2.2). The HPYT has a pyridine while HPOT has a phenyl. These molecules present a rigid skeleton and have been used as multi-binding ligands in coordination chemistry [53, 54]. The adsorption process of thiol on a gold surface is still not completely addressed in the literature. Recently, mixed alkyl thiol layers were investigated using different imaging techniques [55]. This helps to resolve the uncertainty around of STM image interpretation and measured the molecular polar tilt and azimuthal angles. The measurements demonstrated that ordered domains with different superstructures also may reflect change distribution in group structures. In the present work we obtain the STM images of HPOT or HPYT adsorbed on gold surfaces, at room temperature. To support the new interpretation, in addition to the DFT calculation of the system local density of states (LDOS), we develop a simple quantum transport model based on the master equation technique that reproduces the current along the surface measured via STM.

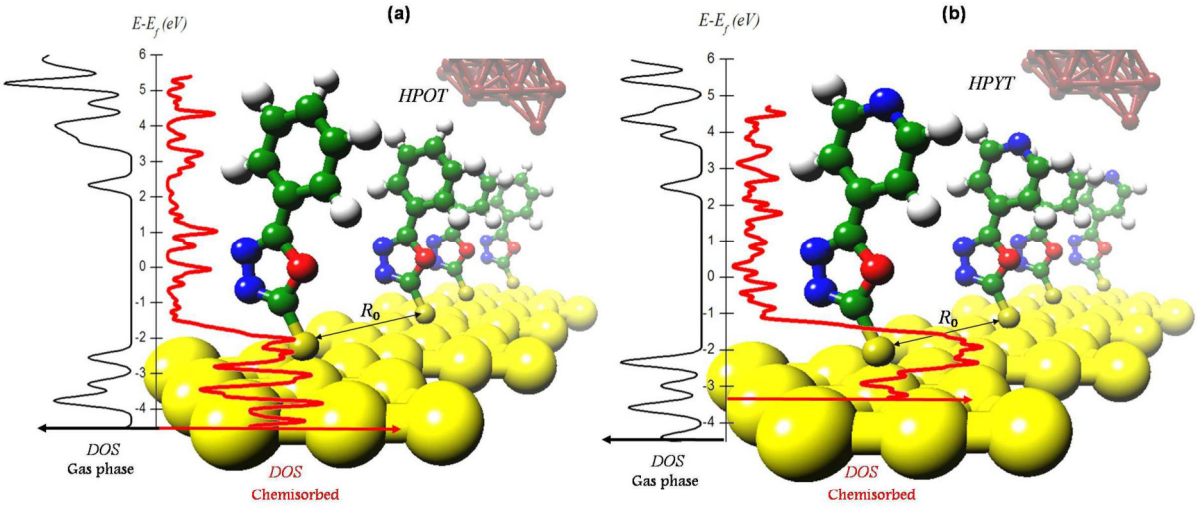

Figure 2.2: Schematics of the molecule ((a) HPOT and (b) HPYT) chemisorbed on the first atomic plane of the Au(111) surface, respectively. $R_0 \approx 0.51$nm is the distance between molecules which is similar for HPOT. Density of States (DOS) plots for HPOT and HPYT molecule in gas phase (black) and chemisorbed (red) are plot. The shift in Fermi energy is due mostly to image charge formation and strong coupling between molecule/metal. The color scheme for the atoms is: C (green), N (blue), O (red), H (white), S (dark yellow), Au (yellow) and tip (brown).

2.3.1 Experiments

The experimental procedure consists of cleaning by flame annealing with a butane torch. Then the sample was fabricated on the $Au(111)$ surface as HPYT or HPOT are deposited. The HPYT and HPOT molecules were purchased from Aldrich and used as received. The molecules were self-assembled on gold from 1 mM solutions made in ethanol for HPOT and in a mixture of water and ethanol at 50 : 50 (v/v) for HPYT. The solution of HPYT was sonicated for 30 minutes to increase solubility. The thiols adsorbed on a thin film of gold deposited on mica. The films were grown by evaporation of gold on muscovite mica at a base pressure of 10^{-6} torr. The mica was heated at $\sim 300°C$ before

evaporating the gold. Gold on mica was flame annealed prior to molecular adsorption and the sample was then quickly transferred for the thiol solution. The incubation period was 30 minutes. The samples were briefly rinsed after removal from solution with pure solvent to eliminate loosely bound molecules. The STM equipment employed was a Nanoscope IIIA with a standard or a low current STM head able to reach a tunneling current of 1 pA. The scanner was employed to acquire the images. Tips were prepared by mechanically cutting a 0.25 mm tungsten wire. The images were collected in constant current for low resolution and in constant height mode for high resolution. Images were submitted to a flattening tool and low pass filtering. The low resolution STM images of the adsorption of HPYT and HPOT on gold show that the molecules modify the $22 \times \sqrt{3}$ reconstruction forming several clusters on the surface. Typical images of the gold surface after HPYT and HPOT adsorption are presented in Fig. 2.3 (a) showing that the clusters are scattered on the terrace for HPYT, but they also form on the steps as seen in Fig. 2.3 (b) upon HPOT adsorption. The mean height of the clusters is $0.25nm$, indicating that they are gold atoms freed from the $22 \times \sqrt{3}$ reconstruction. The molecular structure is formed with low corrugation height and can only be observed in very high resolution, capturing the data in constant height mode.

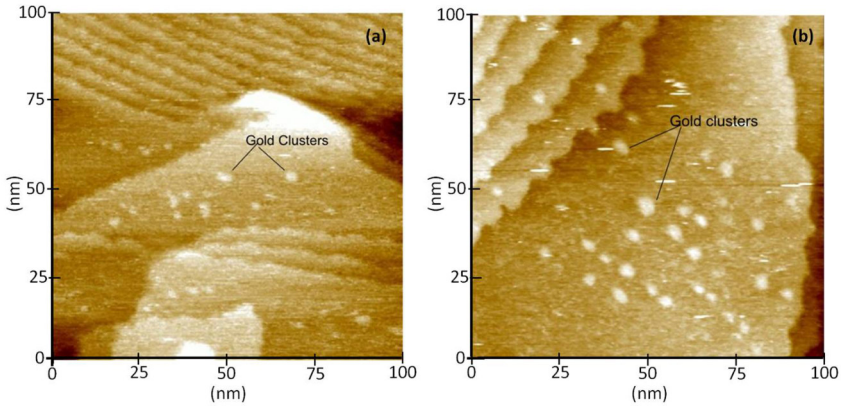

Figure 2.3: (a) Large scale STM image of HPYT on Au(111). Bias voltage (BV) 500 mV. Tunneling current of 5 pA. Image size: 100 x $100nm^2$. (b) Low resolution STM image of HPOT. Bias voltage (BV) 500 mV. Tunneling current of 80 pA. Image size: 100 x $100nm^2$.

2.3.2 Electronic Structure Calculation

The electronic structure geometry optimizations were obtained using (DFT) (details in chapter 1) with the SIESTA code, which provides self-consistent calculations expanding the Kohn-Sham (KS) orbitals as a linear combination of pseudoatomic orbitals for valence electrons. The valence electrons for all systems were described using a double zeta pseudo atomic basis with polarization (DZP) with an energy shift of 0.05 eV. Exchange-correlation is taken into account within the generalized gradient approximation (GGA) using a B3LYP functional. Troulier-Martins norm-conserving pseudopotentials were also employed. A cut-off energy of 150 Ry was used in representing the charge density. In all cases, the relaxed atomic configuration was obtained using a convergence criterion of 0.05 eV/Ang on each atom.

Our calculations suggest that the thiol group $-SH$ is attached to the gold surface via a covalent bond S-Au of $\simeq$ 0.243nm and $\simeq$ 0.248nm for HPOT and HPYT, respectively. This distance regime is often found for the Au-S coupling [56]. In the geometry optimization, the S atom is fixed on a specific adsorption to gold and can move in the z direction perpendicular to the surface. All atoms except the bottom Au layer were then fully relaxed subsequent the geometry optimization calculations to obtain the equilibrium structure for the adsorbed molecules. The bonding between the anchor group and metal surface can be a serious problem and may limit the performance in our computations and stability of organic electronic devices. The HPOT and HPYT molecules are attached to a gold electrode Au(111) with a fixed distance between Au atoms (0.289 nm). The molecule is attached to a single Au atom via the thiol group. Fig.2.4(a) shows the binding molecule-Au atom from the top view (z-axis) and from the lateral side in axis-xy. It is usually accepted that STM currents are proportional to the local density of states (LDOS) [57]. To understand our STM measurements, we computed the LDOS (for a fixed energy near the Fermi level). Fig. 2.4(b) shows the LDOS for the molecules oriented orthogonally to the gold surface in this case the molecules are adsorbed at the three fold

hollow site.

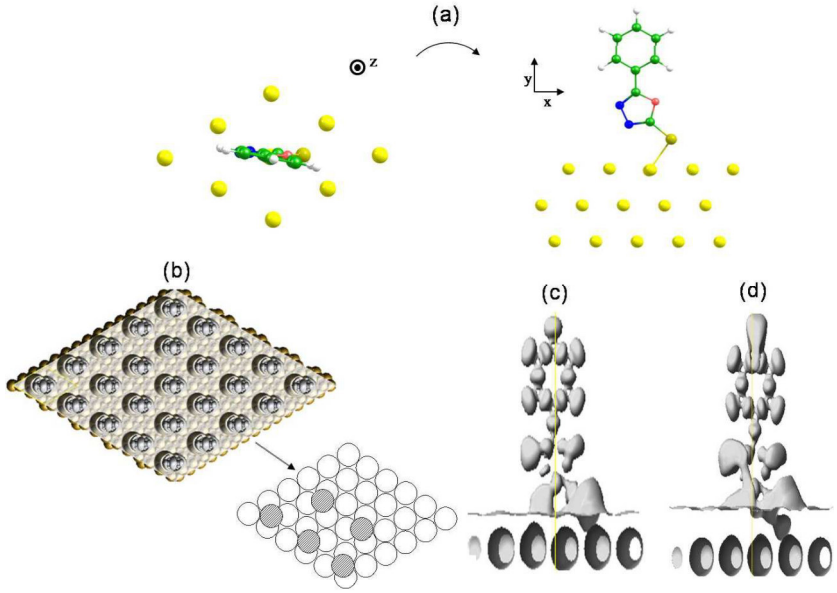

Figure 2.4: The LDOS of the metal-molecule coupling reflects the spacial distribution of electronic states of the molecule on the electrode surface. (a) Unit cell used in the ab initio simulations showing the molecule sitting on top of the Au atom. The ab initio simulations are in good agreement with the actual measurements, but the assumed molecule position differs from current models. (b) The formation of an ordered monolayer on the surface providing parallel columns of molecules oriented orthogonally to the gold surface. Schematics of the molecule position (shaded circles) with respect to the Au atoms (open circles) as usually interpreted in the literature. In this model, the molecule sits on the three fold hollow site between Au atoms. In (c) and (d) for HPOT and HPYT respectively the profile shows the density of electrons on the atom in the molecule, covering the whole molecule with shading in the region of coupling Au-S.

However, from the top view of the LDOS in Fig.2.4(b) (the orientation that the STM tip interacts with the surface), one clearly sees that the electronic cloud spreads around the molecule in such a way that one cannot precisely infer how the molecule binds to the gold surface. From the side axis-xy view of the LDOS isosurface in Fig.2.4(c) for HPOT and (d)for HPYT systems, it is clearly seen that both molecules are connected to the surface by a S-Au bond. The LDOS broadening combined with tilted position of the molecule may lead to erroneous interpretation of STM images, namely, to assume that the molecule sits in the three-fold hollow site of the gold surface, instead of attached to a single Au atom.

2.4 Experimental and Theoretical Images

The STM profile sections of HPYT and HPOT in high resolution are presented in Fig.2.5(a and b). The structure is hexagonal with a periodicity of 0.54 ± 0.04 nm. The observed periodicity is larger than expected, which could be due to thermal drift of the system although the equipment was turned on for a long time before imaging in order to prevent thermal drift. Another parameter that can contribute to misfit with the $\sqrt{3} \times \sqrt{3}R30°$ is the presence of the aromatic groups on top of the thiol. These groups could be all oriented to form a π-stacked connected lattice or they could be oriented randomly, leading to defects in the observed structure.

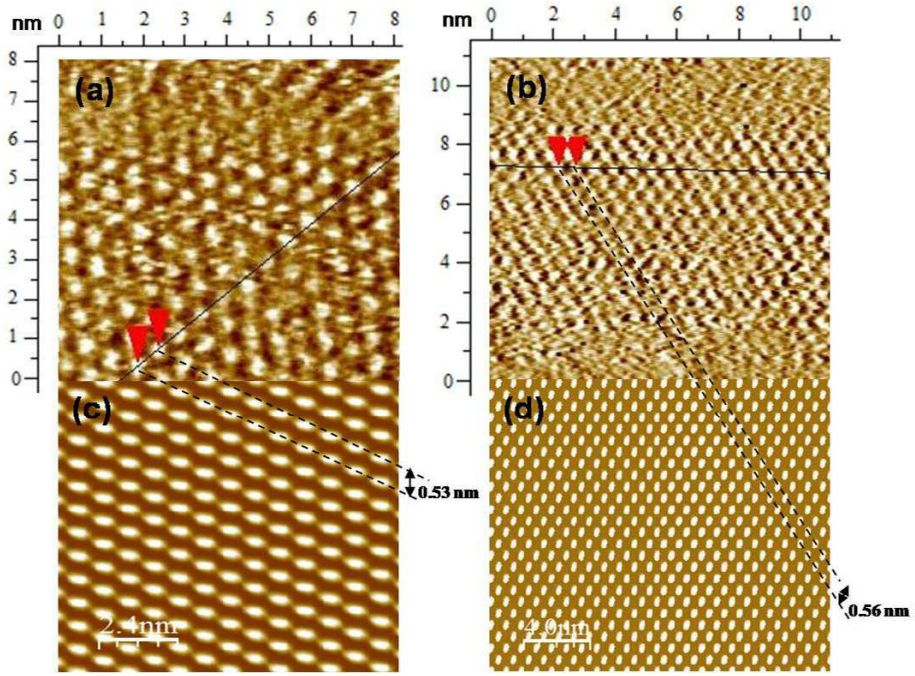

Figure 2.5: (a) STM image of HPOT on Au(111), section profile. Bias Voltage (BV) 200 mV, Tunneling current of 100 pA. Image size: 8.0 x 8.0 nm^2 . (b) STM image of HPYT on Au(111), section profile. (BV) 500 mV, Tunneling current of 5 pA. Image size: 11.0 x 11.0 nm^2. Their respective LDOS ab initio simulations are shown in (c) and (d). The current and the image size for HPOT and HPYT are diferent due the termination, CH and N, respectively.

In Fig. 2.5(c and d) we roughly reproduce the STM image by plotting the projected density of states for electronic states near the Fermi energy obtained from DFT calculations for both HPOT and HPYT systems. The theoretical results agree with the

experimental observation. It can be clearly seen that for both the experimental results and the theoretical predictions the shape of the features are very different for the HPOT and the HPYT. In both, the image of the HPOT molecule is observed as an hexagonal array of large round shaped features while the image for the HPYT is composed of smaller asymmetric rod shaped features. These results indicate that although the structural and electronic properties of the HPOT and HPYT are quite similar, their different interactions with the metallic surface lead to different transport properties. The difference in the effects of the coupling between the molecule and the electrode on the electronic properties of the system is perhaps the first important question about the electronic transport in a nanomolecular device. The discrepancy between the theoretical predictions and the interpretation of the experimental results originates from the fact that the adsorbed molecules are in fact tilted above the substrate (see Fig. 2.5 (c and d)), which, together with the broadening of the thiol density of states leads to an STM image that gives the impression that the molecule is positioned on a three fold hollow site.

2.5 Charge Transport

To gain some physical insight regarding the electron transport properties we propose a simple microscopic physical model. The transport structure is described by the Hamiltonian $H = H_{tip} + H_{host} + H_{molecule} + H_t$, where

$$H_{tip(host)} = \sum_{\mathbf{k}\sigma} \epsilon_{\mathbf{k}\sigma tip(host)} c^{\dagger}_{\mathbf{k}\sigma tip(host)} c_{\mathbf{k}\sigma tip(host)}, \tag{2.5-12}$$

with $\epsilon_{\mathbf{k}\sigma tip(host)}$ being the energy for electrons in the tip (host). The operator $c_{\mathbf{k}\sigma tip(host)}$ ($c^{\dagger}_{\mathbf{k}\sigma tip(host)}$) annihilates (creates) one electron with wave vector $\mathbf{k}$ and spin σ in the tip (host). For the molecule Hamiltonian we use the Anderson model,

$$H_{molecule} = \sum_{\sigma i} \epsilon^{(i)}_{\sigma} d^{(i)\dagger}_{\sigma} d_{\sigma^{(i)}} + \sum_{i} U n^{(i)}_{\uparrow} n^{(i)}_{\downarrow}, \tag{2.5-13}$$

where $\epsilon^{(i)}_{\sigma}$ is a molecular level for spin σ and U the energy penalty for double occupancy energy. The operators $d^{(i)}_{\sigma}$ and $d^{(i)\dagger}_{\sigma}$ annihilate and create, respectively, one electron with

spin σ in the $i-th$ molecule, the molecule is restricted to one site. Finally, the tunneling Hamiltonian is given by

$$H_T = \sum_{\mathbf{k}\sigma\eta i} (V_{\eta\mathbf{k}}^{(i)} c_{\mathbf{k}\sigma\eta}^{\dagger} d_{\sigma}^{(i)} + V_{\eta\mathbf{k}}^{(i)*} d_{\sigma}^{(i)\dagger} c_{\mathbf{k}\sigma\eta}), \tag{2.5-14}$$

where $V_{\eta\mathbf{k}}^{(i)}$ is a matrix element that couples the molecule to the tip ($\eta = t_{tip}$ for tip) or the surface ($\eta = h_{host}$ for host). To calculate transport we follow the master equation formalism [58]. In this approach the current between tip and host through site i is given by [59]

$$I_{\eta}^{(i)} = \epsilon \sum_{\nu} [\Gamma_{\eta}^{(i)} \rho_{\mathbf{0}}^{(i)}]_{\nu}, \tag{2.5-15}$$

with $\rho_{\mathbf{0}}^{(i)}$ being the steady state solution of the matrix equation $\dot{\rho}^{(i)} = \mathbf{M}^{(i)} \rho^{(i)}$, where $\rho^{(i)} = (\rho_0^{(i)}, \rho_{\uparrow}^{(i)}, \rho_{\downarrow}^{(i)}, \rho_d^{(i)})^T$. The components of $\rho^{(i)}$ are the probability of site i being empty, single occupied with spin $\uparrow$ or $\downarrow$ and double occupied, respectively. The matrix $\Gamma_{\eta}^{(i)}$ is defined as follows [60]

$$\Gamma_{\eta}^{(i)} = \begin{pmatrix} 0 & \Gamma_{\eta\uparrow}^{(i)-} & \Gamma_{\eta\downarrow}^{(i)-} & 0 \\ -\Gamma_{\eta\uparrow}^{(i)+} & 0 & 0 & \widetilde{\Gamma}_{\eta\downarrow}^{(i)-} \\ -\Gamma_{\eta\downarrow}^{(i)+} & 0 & 0 & \widetilde{\Gamma}_{\eta\uparrow}^{(i)-} \\ 0 & -\widetilde{\Gamma}_{\eta\downarrow}^{(i)+} & -\widetilde{\Gamma}_{\eta\uparrow}^{(i)+} & 0 \end{pmatrix}, \tag{2.5-16}$$

with the tunneling rates given by

$$\Gamma_{\eta\sigma}^{(i)+} = \Gamma_{\eta\sigma}^{(i)} f_{\eta\sigma} \tag{2.5-17}$$

$$\Gamma_{\eta\sigma}^{(i)-} = \Gamma_{\eta\sigma}^{(i)} (1 - f_{\eta\sigma}) \tag{2.5-18}$$

$$\widetilde{\Gamma}_{\eta\sigma}^{(i)+} = \Gamma_{\eta\sigma}^{(i)} \widetilde{f}_{\eta\sigma} \tag{2.5-19}$$

$$\widetilde{\Gamma}_{\eta\sigma}^{(i)-} = \Gamma_{\eta\sigma}^{(i)} (1 - \widetilde{f}_{\eta\sigma}), \tag{2.5-20}$$

where the Fermi functions $f_{\eta\sigma}$ and $\widetilde{f}_{\eta\sigma}$ are evaluated respectively at $\epsilon_{\sigma^{(i)}}$ and $\epsilon_{\sigma^{(i)}} + U$, i.e., $f_{\eta\sigma} = \{1 + \exp[(\epsilon_{\sigma^{(i)}} - \mu_{\eta})/k_B T]\}^{-1}$ and $\tilde{f}_{\eta\sigma} = \{1 + \exp[(\epsilon_{\sigma^{(i)}} + U - \mu_{\eta})/k_B T]\}^{-1}$. Here μ_{η} is the chemical potential of the tip or the host surface, k_B the Boltzmann constant and T the system temperature. In the presence of bias voltage (eV) the tip and host chemical potentials differ from each other by $\mu_{tip} - \mu_{host} = eV$. The parameter $\Gamma_{\eta\,\sigma}^{(i)}$ is the tunneling

rate between tip ($\eta = t_{tip}$) or host ($\eta = h_{host}$) and the $i-th$ molecule. This parameter given by $\Gamma^{(i)}_{\eta\ \sigma} = 2\pi \sum_{\mathbf{k}} |V_{\eta\mathbf{k}}|^2 \delta(\epsilon - \epsilon_{\mathbf{k}\sigma\ \eta})$ will be assumed energy independent (wideband limit) [61]. In particular, the tunneling rate between molecules and the host surface will be set equal to $\Gamma^{(i)}_{host\ \sigma} = \Gamma_0$ where Γ_0 is a constant value and will be taken as our energy scale. On the other hand, the tunneling rate between the tip and molecules assumes the form $\Gamma^{(i)}_{tip\ \sigma} = \lambda\Gamma_0\ \epsilon^{-(\frac{R-id}{R_0})^2}$, where we have included the parameter λ to account for the asymmetry between tip-molecule and host-molecule coupling. Here in particular λ is much smaller than one since we expect very asymmetric tunneling coupling parameters, with tip-molecule coupling being weaker ($\Gamma^{(i)}_{tip\ \sigma} \ll \Gamma^{(i)}_{host\ \sigma}$). The Gaussian profile in $\Gamma^{(i)}_{tip\ \sigma}$ is to account for a stronger coupling between the tip and site (i) whenever the tip is on top ($R = id$) of that site. R is the tip position along the surface, d the typical molecule separation, i the molecule index and R_0 is the phenomenological coupling decay distance between tip and i-th molecule. This Gaussian profile gives rise to a peak in the total current

$$I_{tip} = \sum_{i=1}^{N} I^{(i)}_{tip}, \tag{2.5-21}$$

whenever the tip is on top of a molecule. Here N is the total number of molecules.

Since we are interested in the steady state transport we must have $\dot{\rho}^{(i)}$ equal zero. So $\rho^{(i)}_{\mathbf{0}}$ will be the eigenvector corresponding to zero eigenvalue of $\mathbf{M}^{(i)}$ matrix. More specifically, $\mathbf{M}^{(i)} = \mathbf{M}^{(i)}_{tip} + \mathbf{M}^{(i)}_{host}$, which is given by matrix $\mathbf{M}^{(i)}_{\eta}$. In Table (2.1) we list all the parameters used in the transport model.

$$\mathbf{M}^{(i)}_{\eta} = \begin{pmatrix} -\Gamma^{(i)}_{\eta\uparrow} f_{\eta\uparrow} - \Gamma^{(i)}_{\eta\downarrow} f_{\eta\downarrow} & \Gamma^{(i)}_{\eta\uparrow}(1-f_{\eta\uparrow}) & \Gamma^{(i)}_{\eta\downarrow}(1-f_{\eta\downarrow}) & 0 \\ \Gamma^{(i)}_{\eta\uparrow} f_{\eta\uparrow} & -\Gamma^{(i)}_{\eta\uparrow}(1-f_{\eta\uparrow}) - \Gamma^{(i)}_{\eta\downarrow}\tilde{f}_{\eta\downarrow} & 0 & \Gamma^{(i)}_{\eta\downarrow}(1-\tilde{f}_{\eta\downarrow}) \\ \Gamma^{(i)}_{\eta\downarrow} f_{\eta\downarrow} & 0 & -\Gamma^{(i)}_{\eta\uparrow}\tilde{f}_{\eta\uparrow} - \Gamma^{(i)}_{\eta\downarrow}(1-f_{\eta\downarrow}) & \Gamma^{(i)}_{\eta\uparrow}(1-\tilde{f}_{\eta\uparrow}) \\ 0 & \Gamma^{(i)}_{\eta\downarrow}\tilde{f}_{\eta\downarrow} & \Gamma^{(i)}_{\eta\uparrow}\tilde{f}_{\eta\uparrow} & \Gamma^{(i)}_{\eta\uparrow}\tilde{f}_{\eta\uparrow} + \Gamma^{(i)}_{\eta\downarrow}\tilde{f}_{\eta\downarrow} - (\Gamma^{(i)}_{\eta\uparrow} + \Gamma^{(i)}_{\eta\downarrow}) \end{pmatrix}$$

2.5.1 Electronic Transport

In Fig.2.6 we present the measured currents for the (a) HPOT and (c) HPYT molecules along with the theoretically calculated current as a function of the tip position. Our one-

Parameter	Physical Meaning	Values	
		HPYT	HPOT
$\epsilon_\sigma^{(i)}$	Adatoms energy levels	-3.92	-3.46
U	Coulomb Energy	0	0
μ_{tip}	Tip chemical potential	0	0
μ_{host}	Host chemical potential	$\mu_{tip}-eV$	$\mu_{tip}-eV$
k_BT	System temperature	2.58×10^{-2}	2.58×10^{-2}
eV	Bias voltage	1.0V	1.0V
V_0	Tunneling coupling parameter	1.0	1.0
d	Adatoms separations	0.53nm	0.56nm
R_0	Decaying factor	0.1nm	0.1nm
λ	Asymmetry parameter	1.15×10^{-8}	1.05×10^{-7}

Table 2.1: Phenomenological parameters used in transport calculation. Energies in units of Γ_0. In the present system Γ_0 typically is around 1 eV.

dimensional theoretical model reproduces satisfactorily the current profile obtained as the tip moves along the direction indicated by the black line in Fig.2.5. The current peaks whenever the tip is located on top of a HPYT or HPOT group. This is so because of the fall off the tunneling V_{tip}^i with distance. It can be noted that both the period and the shape of the experimental curves are to some extent reproduced by the theoretical model approach. The noise in the experimental data comes from irregularities of the molecule array and possible defects along the surface and thermal effects. The tip changes structure during the scanning and some areas in the image have a dimmer contrast. Further improvements of the model, such as considering different coupling parameters between the molecules and the surface, among others, may help to obtain even better agreement between theory and experiments and will be the subject of later studies.

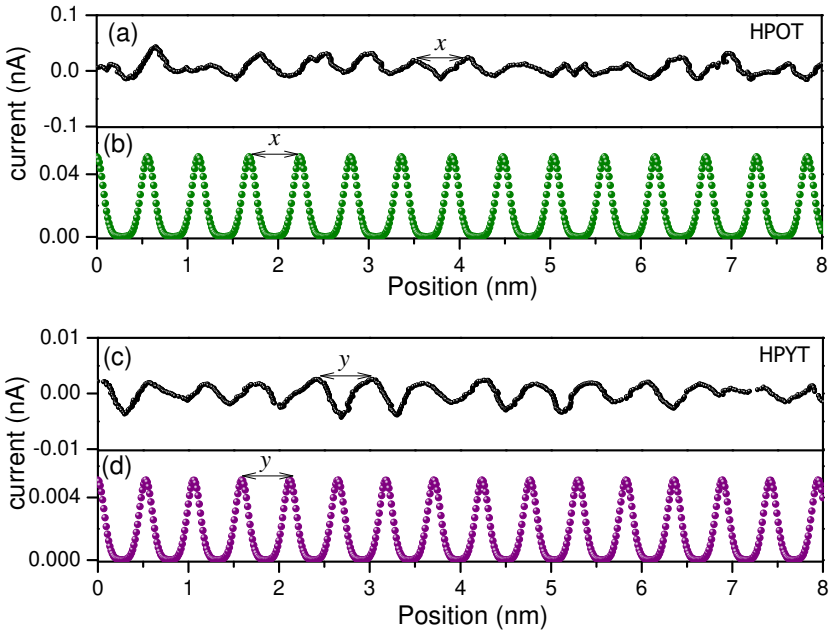

Figure 2.6: (a) Current through HPOT on Au(111) with section profile (Bias Voltage 200 mV) and tunneling current of 0.1 nA. (b) computed STM current HPOT, $x \approx 0.53$nm. (c) Current through HPYT on Au(111), section profile (Bias Voltage 500 mV) and tunneling current of 0.005 nA and (d) computed of the STM current of HPOT, $y \approx 0.56$nm. The molecules are sitting on Au(111) and the calculated currents were found using the transport model proposed in this work.

Chapter 3

Electronic transport in conjugated chains

3.1 Introduction

The field of molecular electronics has been characterized by the search for novel carbon-based materials with low dimensionality, such as fullerenes, carbon nanotubes and graphene, which may be useful as electronic components. These materials with amazing electronic and magnetic properties promise to minimize power consumption, to enhance operation speeds and may be components of future electronic devices. [62–64]. Graphene and graphene nanoribbons have been intensively studied due their unique structure and quantum confinement effects [65–67]. In particular the properties of graphene nanoribbons are strongly dependent on its edges [73].

3.2 Lattice structure

A carbon atom has six electrons, occupying the atomic orbitals $1s^2$, $2s^2$ and $2p^2$. The electrons in the $1s^2$ orbital are strongly bonded and are called core electrons. $2s^2$ and $2p^2$ has four valence electrons. Is the energy difference between $2s$ and $2p$ level is much smaller than their binding energy, then the wave function for these four electrons can blend up easily in a process called hybridzation. Graphene is a single sheet of carbon atoms arranged in the well known honeycomb structure. The carbon atom has four valence electrons, of which three are used for the sp^2 bonds. In a graphene layer the carbon

atoms are distributed at the edges of regular hexagons. The unit cell contains two carbon atoms, labelled A and B as we shown in Fig.3.1(a). The unit vectors are

$$\vec{a}_1 = \left(\frac{\sqrt{3}}{2}a, \frac{a}{2}\right), \vec{a}_2 = \left(\frac{\sqrt{3}}{2}a, \frac{a}{2}\right), \tag{3.2-1}$$

where the lattice constant $\vec{a} = 1.42 \times \sqrt{3} = 2.46$, so that $|\vec{a}_1| = |\vec{a}_2| = a$. This gives us a reciprocal lattice that is also hexagonal, rotated 60° from the Bravais lattice. The reciprocal lattice has with a lattice constant $4\pi/\sqrt{3}a$ and unit vectors shown in Fig.3.1(b)

$$\overrightarrow{b}_1 = \left(\frac{2\pi}{\sqrt{3}a}, \frac{2\pi}{a}\right), \vec{b}_2 = \left(\frac{2\pi}{\sqrt{3}a}, \frac{2\pi}{a}\right). \tag{3.2-2}$$

The particular importance for the physics of graphene are the two points K and $K^{'}$ at the corners of the graphene Brillouim zone (BZ). These are named Dirac points. This approach has been thoroughly described and interested readers are directed to the original article [72].

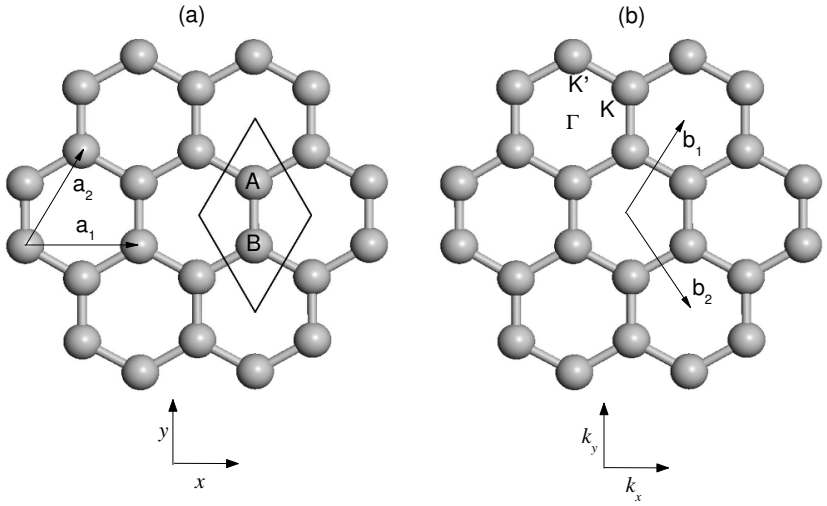

Figure 3.1: Honeycomb lattice for a single plane of grafhite. (a) Carbon atoms are located at each crossings and the lines indicate the chemical bonds, the length of the carbon-carbon bond is known to be 1.42Å , which are derived from sp^2-orbitals. Also shown are the primitive lattice vectors $\vec{a}_1$ and $\vec{a}_2$ und the unit-cell. There are two carbon atoms per unit-cell, denoted by A and B. (b) Reciprocal lattice of graphene with the Brillouin zone, $\vec{b}_1$ and $\vec{b}_1$ are the primitive lattice vectors.

Away from the edges, each carbon atom in a sheet of graphene make up a σ bond with three neighbors. If the graphene lies in the x-y plane. The sp^2 hybridization corresponds to

three σ bonds formed from the $2s$, $2p_x$ and $2p_y$ orbitals. The orbital $2p_z$, is perpendicular to the plane (z-axis), form π covalent bonds. The resulting π energy bands are the main contribution to the electronic structure of graphene. These bands result from the one electron per atom which is not involved in nearest-neighbor σ bonding, so in calculations of the band structure, we consider only this one electron per carbon atom. Note here the similarities between the electronic orbitals in graphene and in conjugates melecule with sp^2 hybridization, such as polyacetylene [69, 74]. Both geometries are our focus in this chapter.

We carry out a LCAO calculation on the lattice described above in order to find the electronic band structure. The wave function that represent the atoms in lattice is:

$$\psi_{\vec{k}} = \sum_{R\in\Re} e^{i\vec{k}.\vec{R}}\phi(\vec{x}-\vec{R}), \tag{3.2-3}$$

where $\vec{R}$ denotes the set of lattice vectors that represent a Bloch wave. $\psi_{\vec{k}}$ is also called Wannier function [7]. The $\phi(\overrightarrow{x})$ is the atomic wave function. In this representation has two orbitals such in the unit-cell, ϕ_A and ϕ_B, respectively. It is important to remember that LCAO approximation assumes that the atomic wave-function are well localized at the position of the atom. The linear combination between ϕ_A and ϕ_B is the total function,

$$\phi(\vec{x}) = b_1\phi_A(\vec{x}) + b_2\phi_B(\vec{x}) = \sum_n b_n\phi(\vec{x}). \tag{3.2-4}$$

We saw in Chapter 2 the description of a many body Hamiltonian of many-body system time independent. Now we are going to consider the Hamiltonian for a single electron in the atomic potential by all the carbon atoms, as the Hartree Fock approximation [49].

$$\hat{H} = \frac{p^2}{2m} + \sum_{\vec{R}\in\Re}[V_{at}(\vec{x}-\vec{x}_A-\vec{R}) + V_{at}(\vec{x}-\overrightarrow{x_B}-\vec{R})], \tag{3.2-5}$$

where $x_{A,B}$ is the postion of the two carbon atoms. The energy resulting after applying H in $\phi_{A,B}$ is:

$$\hat{H}\phi_A = \epsilon_A\phi_A + \left(\underbrace{\sum_{\vec{R}\neq 0} V_{at}(\vec{x}-\vec{x}_A-\vec{R}) + V_{at}(\vec{x}-\vec{x_B}-\vec{R})}_{\Delta U_A}\right)\phi_A, \tag{3.2-6}$$

and,

$$\hat{H}\phi_B = \epsilon_B\phi_B + \left(\underbrace{\sum_{\vec{R}\neq 0} V_{at}(\vec{x}-\vec{x}_A-\vec{R}) + V_{at}(\vec{x}-\vec{x_B}-\vec{R})}_{\Delta U_B} \right) \phi_B, \tag{3.2-7}$$

where $\epsilon_{A,B}$ is the energy value for the atomic state p_z. The second term is a potential value and now we can abbreviate it as $\Delta U_{A,B}\phi_{A,B}$. The potential $\Delta U_{A,B}$ is smaller and than $\Delta U_{A,B}\phi_{A,B}$ is smaller also. The equation which are the starting point of the LCAO calculation is:

$$\hat{H}\phi_{A,B} = \epsilon_{A,B} + \Delta U_{A,B}\phi_{A,B}. \tag{3.2-8}$$

For simplification we use $\epsilon_A = \epsilon_B = 0$. The new equation will read,

$$\hat{H}\phi_{A,B} = \Delta U_{A,B}\phi_{A,B}. \tag{3.2-9}$$

In this point we have an equation for the potential. It is necessary to solve the Schrödinger equation.

$$\hat{H}\psi_k = E(k)\psi_k. \tag{3.2-10}$$

The projection of ψ_k on the two states $\phi_{A,B}$,

$$E(k)\langle\phi_{A,B}|\psi_k\rangle = \langle\phi_{A,B}|\Delta U_{A,B}|\psi_k\rangle. \tag{3.2-11}$$

To calculate the terms $\langle\phi_{A,B}|\psi_k\rangle$ let us to assume that only nearest-neighbour overlap integrals have to be taken into account. We can represent the overlap integral:

$$\gamma_0 = \int \phi_A^*\phi_B(\vec{x}-\vec{a_1}) \tag{3.2-12}$$

and assuming the $\gamma_0 \in \Re$, we obtain two equations,

$$\langle\phi_A|\psi\rangle = b_A + b_B\left(\gamma_0\right)\ \left(1 + e^{-i\vec{k}.\vec{a}_1} + e^{-i\vec{k}\vec{a}_2}\right), \tag{3.2-13}$$

and

$$\langle \phi_B|\psi\rangle = b_B + b_A\left(\gamma_0\right)\ \left(1 + e^{i\vec{k}.\vec{a}_1} + e^{i\vec{k}\vec{a}_2}\right), \tag{3.2-14}$$

Now we calculate to calculated $\langle \phi_{A,B}|\Delta U_{AB}|\psi\rangle$, we can use the same condition used in (3.2-12)

$$\gamma_A = \gamma_B = \int \phi_A^* \Delta U_A \phi_B = \int \phi_B^* \Delta U_B \phi_A. \tag{3.2-15}$$

The integral is equal due to symmetry and also $\gamma_{A,B} \in \Re$. The expected value for $\Delta U_{A,B}$ is:

$$\langle \phi_A|\Delta U_A|\psi\rangle = b_2\gamma_A - \left(1 + e^{-i\vec{k}\vec{a}_1} + e^{-\vec{k}\vec{a}_2}\right), \tag{3.2-16}$$

and

$$\langle \phi_B|\Delta U_A|\psi\rangle = b_1\gamma_A - \left(1 + e^{i\vec{k}\vec{a}_1} + e^{\vec{k}\vec{a}_2}\right). \tag{3.2-17}$$

The eigenvalue finally can be formulated by:

$$\alpha(\vec{k}) = 1 + e^{-i\vec{k}\vec{a}_1} + e^{-i\vec{k}\vec{a}_2}, \tag{3.2-18}$$

In this case the dispersion relation $E(\vec{k})$ is obtained when $det = 0$,

$$\begin{bmatrix} E(\vec{k}) & \alpha(\gamma_0 E(\vec{k}) - \gamma_A) \\ \alpha^*(\gamma_0 E(\vec{k}) - \gamma_A) & E(\vec{k}) \end{bmatrix} \begin{bmatrix} b_1 \\ b_2 \end{bmatrix} = \begin{bmatrix} 0 \\ 0 \end{bmatrix}. \tag{3.2-19}$$

the trivial solution is when, $\gamma_0 = \gamma_A = 0$ this way $E(\vec{k}) = 0$

Using γ_0 really small, we can give (as an approximation) the very simple dispersion relation:

$$E(\vec{k}) = \pm\gamma_A|\alpha(\vec{k})|, \tag{3.2-20}$$

Where the magnitude of α, is

$$E(\vec{k}) = \pm\gamma_A\sqrt{3 + 2\cos(\vec{k}\cdot\vec{a}_1) + 2\cos(\vec{k}\cdot\vec{a}_2) + 2\cos(\vec{k}\cdot(\vec{a}_2 - \vec{a}_1))}, \tag{3.2-21}$$

If we write in cartesian in $\vec{k}$ components Fig 3.1 (a)

$$E(\vec{k}_x, \vec{k}_y) = \pm\gamma_A \sqrt{1 + 4\cos\left(\frac{\sqrt{3}a \cdot \vec{k}_y}{2}\right)\cos\left(\frac{a \cdot \vec{k}_x}{2}\right) + 4\cos^2\left(\frac{a \cdot \vec{k}_x}{2}\right)}, \quad (3.2\text{-}22)$$

where $\vec{a}_{1,2}$ is a lattice constant $\vec{a} = \sqrt{3}\ \vec{a}_0$

Draw the reciprocal lattice, the primitive vectors $\vec{b}_1$ and $\vec{b}_2$ and 1^{st} Brillouin zone (BZ). The BZ is hexagonal. There are six corner points located at the BZ boundary. These points are called K-points.

$$|\vec{b}_{1,2}| = \frac{4\pi}{3a_0}. \quad (3.2\text{-}23)$$

In Fig 3.1(b) one K-point is show with its respective wavevector $\vec{k}$ pointing along the x-axis:

$$\vec{k} = \frac{4\pi}{3\sqrt{3}a_0}\vec{e}_{\vec{x}}, \quad (3.2\text{-}24)$$

The eigenvalue is zero for all $\vec{K}$-points, $E(\vec{k}) = 0$, but the important question is this case is how large is the dimension of the Eigenvalue. In order to answer this question, one has to have a look at Eq.3.2-19. The $\vec{b}_1$ and $\vec{b}_2$ can be choosen arbitrarily. It is a common practice (also in view of the symmetry of the states at $\vec{K} = 0$), to use normalized symmetric and antisymmetric wavefunctions. If $p_z(\vec{x})$ is the atomic p_z orbital, then we can write $\phi_{1,2}(\vec{x}) = p_z(\vec{x} - \vec{x_{1,2}})$. The symmetric ϕ_s and the antisimmetric ϕ_a wavefunctions are:

$$\phi_{s,a} = \frac{1}{\sqrt{2}}\left(p_z(\vec{x} - \vec{x}_1) \pm p_z(\vec{x} - \vec{x}_1)\right), \quad (3.2\text{-}25)$$

There are two degenerate wavefunctions at $\vec{k} = \vec{K}$:

$$\psi_{\vec{K}(s,a)}(\vec{x}) = \sum_{\vec{R}\in G} e^{i\vec{K}\cdot\vec{R}}\phi_{(s,a)}(\vec{x} - \vec{R}), \quad (3.2\text{-}26)$$

3.3 The properties of graphene nanoribbon

The first theoretical works on graphene nanoribbons and the discussion an their band gaps appeared several years before graphene was discovered. In 1987, Tanaka et. al.

[69] carried out tight binding calculations for polymer chains called "One-dimensional graphite", and noted a decrease in the band gap for molecules with a wider graphene structure added to the polymer backbone. Stein et. al. [74] studied hexagonally symmetric aromatic molecules, essentially small pieces of graphene, and found a decrease in the HOMO-LUMO gap with increasing molecule size. The mid-90s saw some renewed interest in GNRs, sometimes called "nanographites" or "carbon nanoribbons". In particular, the properties of graphene nanoribbons are strongly dependent on the atomic arrangement of their edges [73]. There are two basic types os graphene nanoribbon (GNRs) according to the edge configuration. The nature of the ribbon depend of the direction that is limited: armchair or zigzag. The armchair GNRs are either metallic or semiconducting, depending on the number of chains while zigzag GNRs are always metallic. In Fig3.2 (a)and (b) we have a honeycomb lattice along the $x - y$ direction. If we choose the ribbon infinite in the y direction we produce a graphene *armchair* nanoribbon (AGNR). Otherwise if we choose infinite in the x direction we produce the *zigzag* graphene nanorribon (ZGNR).

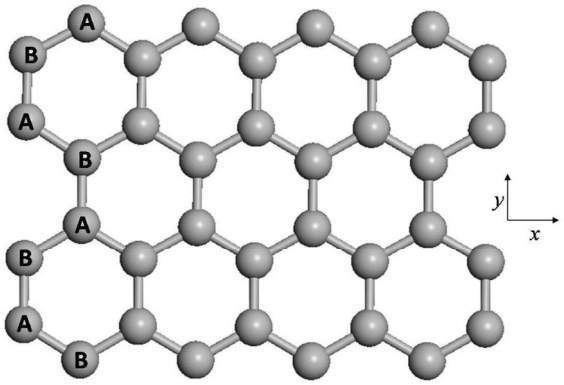

Figure 3.2: Representation for honeycomb lattice where the x-axis produce the zigzag graphene nanorribon and y-axis produce a graphene armchair nanoribbon.

Specifically, the zigzag graphene nanoribbons (ZGNRs) have fascinating properties including magnetic states localized at the Fermi energy (E_F), where the polarized electron spin has antiferromagnetic (AF) ordering that is coupled between the two opposite edges [75]. The degenerate state near the Fermi level comes in the form of a pair of at bands corresponding to localized edge states. These zigzag edge states have been the subject of

much theoretical [76], and some experimental [77] work. We represent the AF and bands structure for 4-ZGNRs.

The AF ordering at the edges can be controlled by an electric field applied across the ribbon and may result in spin selective control over the ZGNRs properties. [78]. The ZGNRs with imperfect edges have been shown to exhibit a strong ferromagnetic behavior and a nonzero spin conductance, [79,80] and these magnetic properties may potentially be applied in spin filtering systems [81–83] that might be controlled by applying an electric field. Recent studies predict that molecular junction systems such as zigzag-armchair [84] and zigzag-zigzag [85] combinations of ZGNRs exhibit half-metallicity and conductance strongly dependent on the nature of the molecular junction.

3.4 ZGNRs and polyacetylene coupling

Technological applications of molecular devices are still far from becoming reality because fundamental issues such as the thermal stability of these devices and the nature of the metal-organic coupling are not yet completely addressed. Inconsistencies exist regarding surface charge distribution, chemical composition and the quality of molecule-metal coupling, which is responsible for charge transfer and reflection effects [86–89]. Experimental and theoretical interference effects can be observed at a molecule attached between metallic electrodes with different anchoring position [90]. The *para*-linkage are known due high dips at transmission around the Fermi energy while the *meta*-linkage benzene species shown lower conductance with [91–93]. This happens at conduction due to the phenomenon of quantum interference [94]. A study has demonstrated that the properties of spin filtering can depend on the linker positions (*para* or *meta*) in benzene rings [95]. The spin filtering is large in systems which have a large spin density [96] and to find this characteristics in molecules is more complicated than ZGNRs where the half-metallicity is a natural behavior. However, these challenges may be overcome by the use of graphene in lieu of metal electrodes. The ZGNRs structure is energetically most stable

for connecting linear carbon chains with sp or sp^2 hybridizations [97,98].

We investigate spin-polarized transport properties of the molecular junction between polyacetylene and ZGNRs by performing calculations using a non-equilibrium Green's function (NEGF) technique combined with density functional theory (DFT). The two-probe geometry corresponds to a central scattering region containing the molecular bridge and it is connected to the semi-infinite ZGNR electrodes, as shown in 3.3(a). Note that the central region also includes parts of each electrode (as buffer layers), which is necessary to ensure smooth electronic potential and density at the boundaries with the electrodes. This arrangement of carbon atoms as electrodes has been shown to have high stability and half-metallicity, [145] and they were selected to solve an important problem of interconnection in molecular transport junction [100].

The connection between the molecular bridge (polyacetylene $CH\,[C_2H_2]_6$) and 4-ZGNRs is a molecular junction in which at the termination of the 4-ZGNRs is a stepped. Since the graphene unit cell contains two non-equivalent carbon atoms which form the A and B sublattices, there are two possibilities for connecting the polyacetylene chain to the 4-ZGNRs leads. Several insights can be realized with these geometries. In one case the bridge can connect to the A atom of the 4-ZGNRs resulting in a local *para*-linkage (BC-P system, 3.3(b)), or the bridge can connect to the B atom of the 4-ZGNRs resulting in a local *meta*-linkage (BC-M system, 3.3(c)), as indicated by the red arrows in 3.3. The BC-P system has a connection in B atom that represent *ortho*/-linkage while the BC-M system is *meta* to both A and B atoms. The goal of this work is to understand how these two different connections affect the spin transport properties in such conjugated bridges.

3.4.1 Computational details

Firstly, our focus is in the electronic structure for the central scattering region system where we created periodic conditions in the z direction (4-ZGNRs). The periodic system is a cubic supercell containing the BC-P or BC-M systems (3.3(b) and (c)) . The electronic structure and geometry optimizations were performed using DFT [101,102] with the

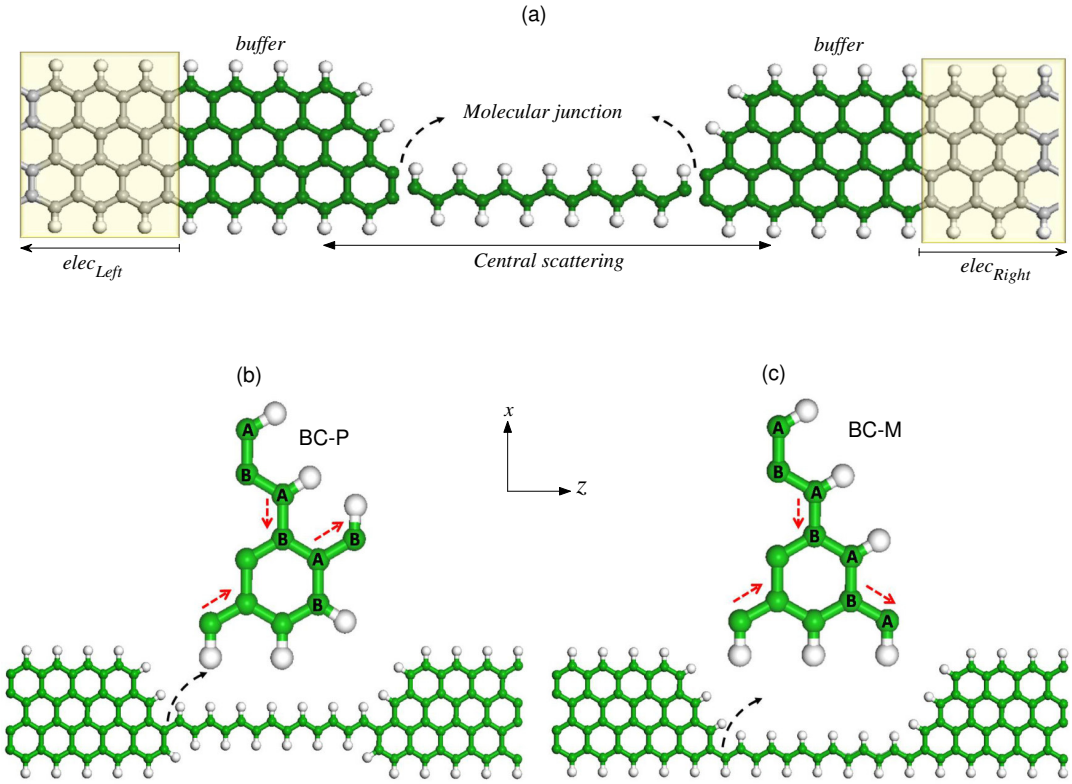

Figure 3.3: (a) Two-probe transport geometry. The central scattering region contains the polyacetylene bridge as well as several buffer layers of each electrode. The shaded regions include the two semi-infinite electrodes. Geometries showing (b) the connection of the polyacetylene bridge to ZGNR to make the BC-P (*para* / *ortho*-linkages) system and (c) the connection to form the BC-M (*meta*-linkage to both A and B atoms). A and B represent the different A/B sublattice carbon atoms.

SIESTA code [103], which provides self-consistent calculations expanding the Kohn-Sham (KS) orbitals as a linear combination of atomic orbitals (LCAO) for valence electrons. The norm-conserving Troullier-Martins pseudopotentials [104] were used to describe the core electrons. The valence electronic orbitals of the systems were described using a double-ζ polarized basis set [105]. Exchange-correlation is taken into account within the local spin density approximation (LSDA) [106–108]. A cut-off energy of 150 Ry was used and, in all cases, the relaxed atomic configuration was obtained using a convergence force criterion of less than 0.05 eV/Å on each atom. An external electric field varying from 0.0 V/nm to 0.5 V/nm was applied across the ribbon along the x-axis (in-plane). These values are enough to keep antiferromagnetic (AF) ordering since it has been shown that both the

spin polarization and half-metallicity are destroyed under so strong external electric field ($\vec{E}_{ext} > 0.8\ V/nm$) [109]. The Brillouin zone (BZ) was sampled as a Monkhorst-Pack grid [110] using $1 \times 1 \times 100$ k points.

The electronic transport properties are obtained by using the TranSiesta code, [111] which employs the non-equilibrium Green's function (NEGF) technique within the Keldysh formalism in combination with DFT [112]. This technique is applied to a two-probe system, as shown in 3.3(a). Note that in our calculation all atoms are described self-consistently at the same level of theory for the central region and the electrodes. This approach has been thoroughly described and interested readers are directed to the original articles [23, 113–118]. Details about this formulations we rediscussed in chapter 2.

Our focus here is on the electron transmission around the Fermi energy at zero bias $[T_\sigma(E, V = 0)]$, where σ is the spin (up/down). The Landauer-Büttiker transmission [6] probability can be calculated as the trace over the matrix product of the coupling matrices $\Gamma_{L/R,\sigma}$ [120] and the $(G/G^\dagger)$ Green's function of the central region

$$T_\sigma(E, V) = \mathrm{Tr}(\Gamma_{R,\sigma} G_\sigma \Gamma_{L,\sigma} G_\sigma^\dagger), \tag{3.4-27}$$

which represents the probability that an electron with a given energy E transmits from the left electrode, through the central region, into the right electrode. The spin filter efficiency [81, 83] (SFE) at the Fermi level is defined as:

$$\mathrm{SFE} = \frac{|T_{up}(E_F) - T_{down}(E_F)|}{T_{up}(E_F) + T_{down}(E_F)}. \tag{3.4-28}$$

We calculated SFE achieved at zero bias under different electric fields for BC-P and BC-M systems.

3.4.2 The BC-P and BC-M systems

It is known that bands near the Fermi level correspond to states near the edges of the graphene nanoribbon giving rise to the half-metallicity states. This result has been discussed extensively in the literature [121]. The interesting and relevant point here

is to know how the electronic structure will be affected by the discontinuity of the 4-ZGNRs at the junctions. We first consider this by studying the electronic structure of the central region shown in Figure 3.3(a), setting the structures shown in Figure 3.3(b,c) to be periodic in the z-direction and calculating the band structure and the projected density of states (PDOS). In the BC-P system, an interesting behavior appears in the bands of this molecular junction (Figure 3.4(a)), especially near the Fermi energy. There is a dispersive band that crosses the Fermi energy and there are also flat bands nearby. The PDOS indicates that this dispersive level is coming from 4-ZGNRs states mixed with bridge states. Differently, in the BC-M system (Figure 3.4(b)) there is a gap in dispersive states near E_{F}. The flat bands near the Fermi energy are confined in the bridge ($\simeq 0.1$ eV). Overall, the relevant contribution comes from dispersive states whether or not they appear near the Fermi energy; an effect due to the junction between 4-ZGNRs and the bridge.

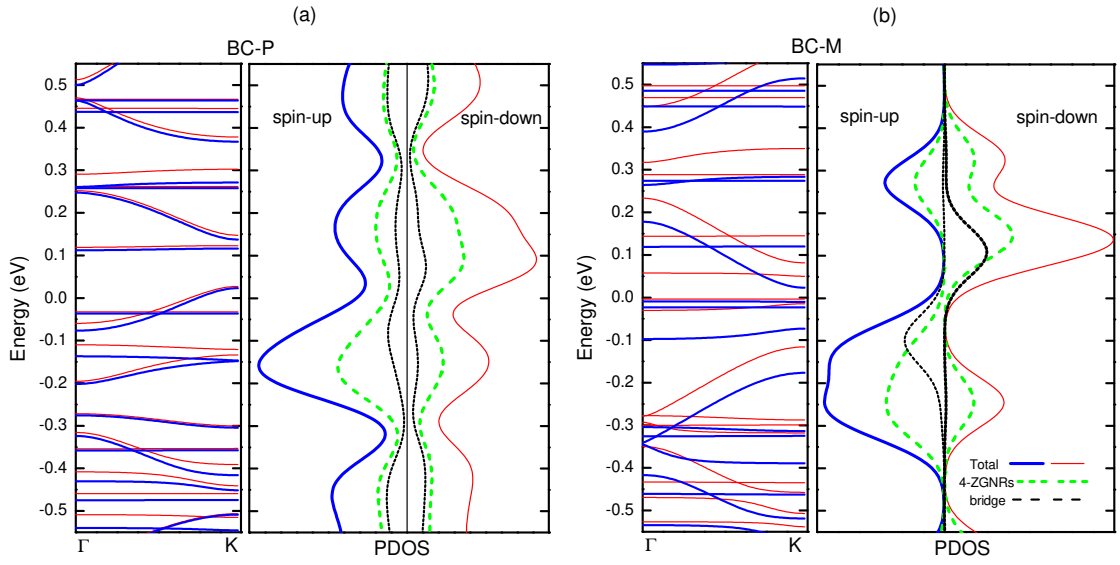

Figure 3.4: Electronic band structure and projected density of states (arb. unit.) for (a) BC-P and (b) BC-M systems at zero electric field. The solid (dark blue) lines and solid (light red) lines denote spin-up and spin-down, respectively. Note the difference in the bands around the Fermi energy ($E_{\mathrm{F}} = 0$) in the BC-P and BC-M system.

In practice, bringing a system to a regime of open conduction channels can be achieved using an electric field as a gate. The field-effect gating in the molecular junction can

control the orbitals with respect to Fermi energy in two different current regimes within a large operation region, resulting in the ability to turn the current on/off. Experimental work has demonstrated a molecular field effect transistor that can be directly tuned by gate voltage [119]. In this work an external electric field ranging from 0.0 V/nm to 0.5 V/nm is applied across the systems in the x-direction. Figure 3.5(a) and (b) show the PDOS of the BC-P and BC-M systems under various field strengths, projected onto the 4-ZGNRs and the polyacetylene molecular bridge. The bridge states shift in energy due to the electric field, as illustrated by the PDOS. The largest contribution comes from the 4-ZGNRs for the BC-P system, while for the BC-M system the gap around the Fermi energy shows an interesting behavior in the bridge for spin-up. The peaks near the Fermi energy are the most relevant states because they describe low-bias transport properties.

Figure 3.5(c) shows the spin density for the BC-P system under different electric fields. The spin density configurations differ slightly from 0.0 to 0.3 V/nm, with most differences being a reduction in the top half and increases in the bridge. Then, with a stronger field of 0.5 V/nm, the spin density is drastically decreased in the top half, while keeping the polarized states on the bridge and bottom half. The BC-M (Figure 3.5(d)) system preserves the AF ordering on the bottom side while local magnetization is reduced on the top half which has mostly spin up configuration. In both cases the systems preserve half metallicity with different values of electric field.

3.4.3 The spectrum of transmission

Several insights can be gained from the geometry. In Figure 3.6, we show the transmission plots of the perfect 4-ZGNRs with electrodes having AF (a,b) and FM (c,d) configurations (solid blue and red lines for spin-up and spin-down, respectively). Typically, transmission peaks are very high due to edge states at zero bias. Figure 3.6(a) shows the transmission for the BC-P system coupled to AF electrodes. In this case there is a transmission gap at the E_{F} of about 0.27 eV for both the spin-up and spin-down. The transmission probability is similar for the two spin channels but on opposite ends of

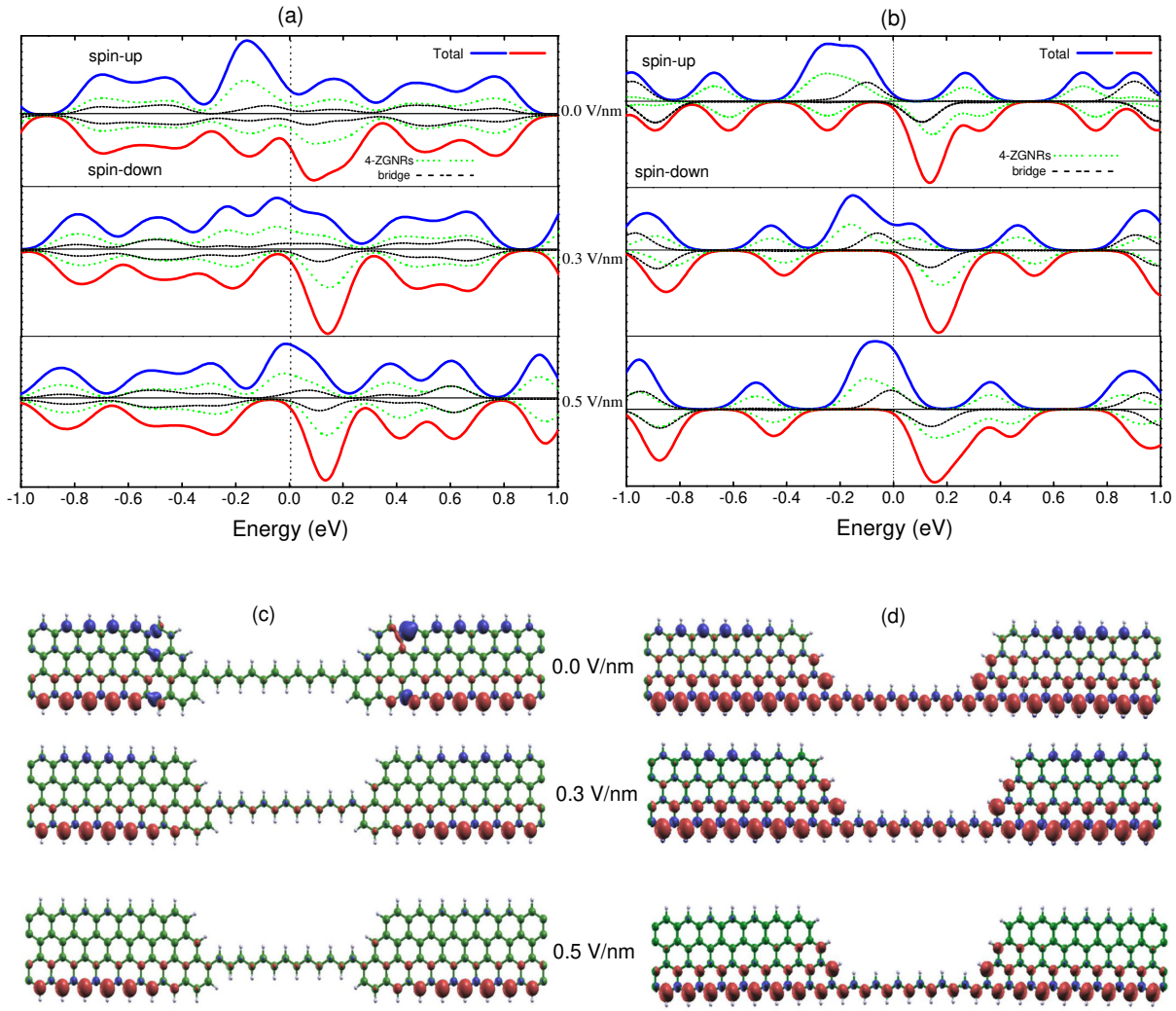

Figure 3.5: Projected density of states for (a) BC-P and (b) BC-M systems under different electric fields. Both systems exposed to electric field exhibit large projections around the Fermi energy. Plots of spin density isosurfaces for the (c) BC-P and (d) BC-M systems. Note that there is a magnetic moment in the bridge, and that the different couplings change the ordering and the extent of the magnetization. The colors blue and red correspond to spin-up and spin-down (orbital contour value is 0.001).

the E_{F}. For instance, the transmission is near unity and broad for spin-up beneath the gap at E_{F}, while the transmission is near unity and broad for spin-down above the gap at E_{F} (compare solid blue and red lines in Figure 3.6(a)). In Figure 3.6(b), we see that the transmission through the BC-M system connected to AF electrodes is much lower due to the binding geometry (*meta*-connection) in this system. It is interesting to note that the spin-down transmission peak (above E_{F}) is considerably larger than the spin-up transmission peak (below E_{F}).

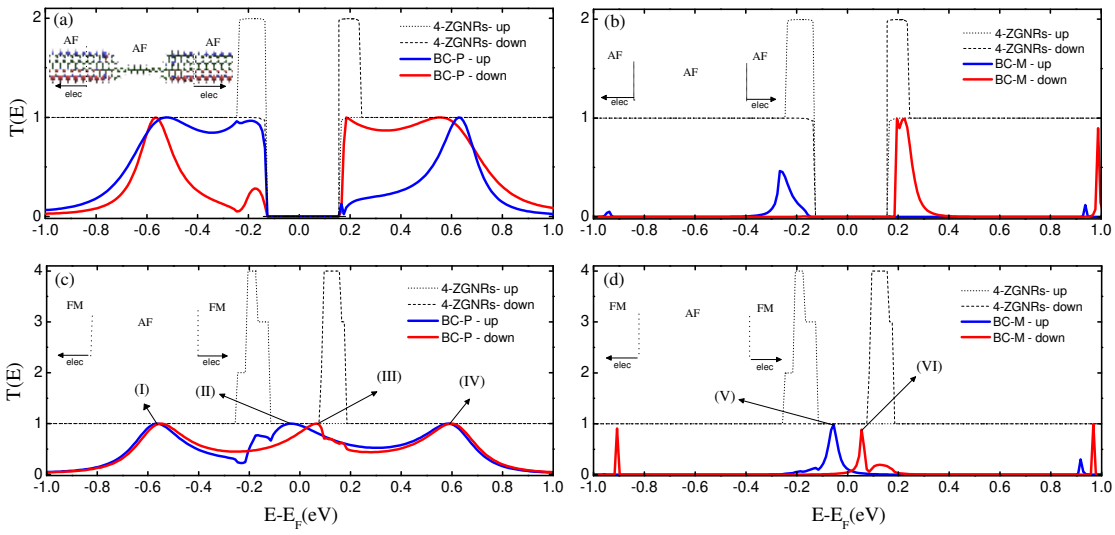

Figure 3.6: The transmission spectra for two-probe systems. Solid lines show spin-up/down (blue/red) transmission through (a) BC-P and (b) BC-M connected to AF electrodes; and (c) BC-P and (d) BC-M connected to FM electrodes. Dotted show transmission through perfect ZGNR for comparison.

Figure 3.6(c) shows the transmission spectrum for the BC-P system coupled to electrodes with FM configurations, which has three broad peaks in the [-1,1] eV range. There is no gap around the Fermi energy, as was also indicated by the projected density of states (PDOS) in Figure 3.4(b). For the BC-M system (Figure 3.6(d)), the spin-up peak localized close to the Fermi energy corresponds to a band centered near -0.1 eV (see Figure 3.4(c)). This peak is the result of a blend between 4-ZGNRs and bridge states, as we showed in Figure 3.5(b). The spin-up and spin-down transmission spectra are quite different near the Fermi level for both structures and in general all states are strongly influenced by the molecular junction.

From here on, we consider the spin configuration consisting of the FM coupling on BC-P and BC-M (AF configuration at the central region. This spin configuration is crucial for the spin filter effect or in a spin valve.

The scattering state wave functions for different transmission peaks through BC-P and BC-M systems coupled to electrodes with FM configuration are plotted in Figure 3.7. They show different modes of transmission through the system for several transmission

peaks in Figure 3.6. The isosurfaces for (I-IV) show scattering states for the BC-P system. Note that the contributions come from the bottom edge and also the top edge of the ZGNR (*para* and *ortho* to polyacetylene bridge, respectively; see Figure 3.3(b)). Clearly, the contribution from peaks (I-IV) will result in high current. Conversely, isosurfaces (V-VI) for the BC-M system do not show any strong contribution from either edge of the ZGNR since these are at meta positions relative to the polyacetylene bridge.

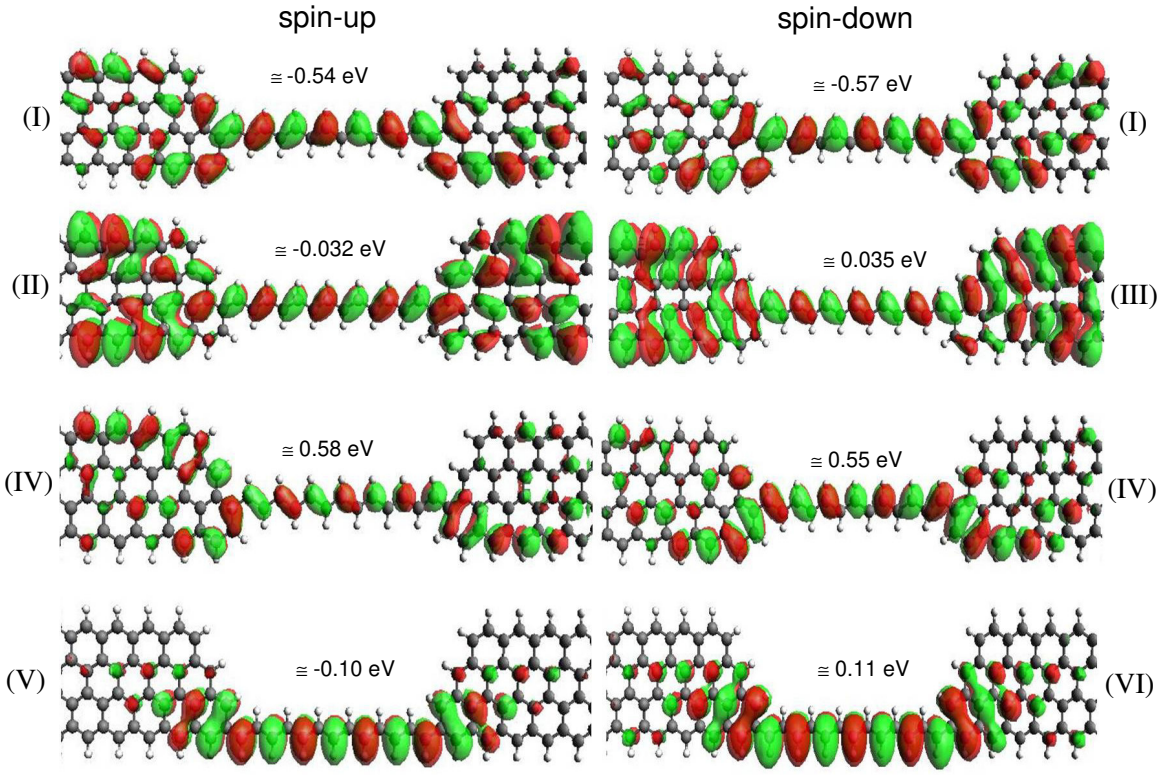

Figure 3.7: The scattering state wave functions for BC-P (I-IV) and BC-M (V-VI) systems. The selected energies correspond to the transmission peaks in 3.6.

For (IV)configuration, the scattering states are distributed throughout the BC-P system, and here it is too complicated to predict a direction for the isosurfaces. The scattering states for spin-up (0.58 eV) cross the system using opposite edges (top to bottom half) and for spin-down cross the bridge using the bottom half (left and right 4-ZGNR's). These configurations represent *para*-linkage having large spin density, represented by isosurfaces characterizing the high conductivity. The BC-M system shows only two peaks in transmission (V and VI). In this system, the more pronounced contribution is from the bridge

as we see in Fig. 3.4(b). These peaks are due to states localized in the bridge that extend along the center in the 4-ZGNRs, clearly, the contribution from I, II, III and IV will result in high current.

To understand if the different transmission channels are preserved, we compare the transmission for systems under electric fields of 0.3 V/nm and 0.5 V/nm. Figure 3.8(a) and (b) shows transmission under different electric fields for the BC-P system with spin-up and spin-down, respectively. One can find transmission peaks in the same range as at 0.0 V/nm, where for spin-up there is a dip around -0.2 eV due to a ring current reversal present in the *para*-benzene system [95]. For this system there is a specific shift when an electric field is applied. In other words, the BC-P system preserves the resonance between different transmission channels and shows broad peaks in the same energy range for spin-up and spin-down. The BC-M system, panel (c) (spin-up), has a transmission peak around the Fermi energy. After applying an electric field of 0.3 V/nm and 0.5 V/nm, the width of the transmission peak decreases with electric field and moves closer to E_{F}. Panel (d) shows the spin-down transmission for the same system. There is a narrow peak above E_{F} that is broadened and shifted away from E_{F} with the application of an external field of 0.3 and 0.5 V/nm.

The characteristics of spin transport shown in Figure 3.8, where the transmission peaks are shifted under external electric field, suggest that these systems might work as spin filters. In Table 1, we list the calculated zero-bias SFE (eq.3.4-28). For BC-P, the SFE at 0.0 V/nm is 9 %, and this value increases to 18 % at 0.3 V/nm. For 0.5 V/nm the spin-up transmission peak passes through E_{F} and the SFE goes down. This variation in SFE suggests that the BC-P (*para*-linkage) system has a shift in the transmission with the help of external electric field and may behave as a weak spin filter.

The BC-M system showed a significant energy shift under the electric field, and the greatest amount of spin-filtering we found was 88 %. For this system, SFE increases with the transverse electric field. In this case, one narrow peak is brought in resonance

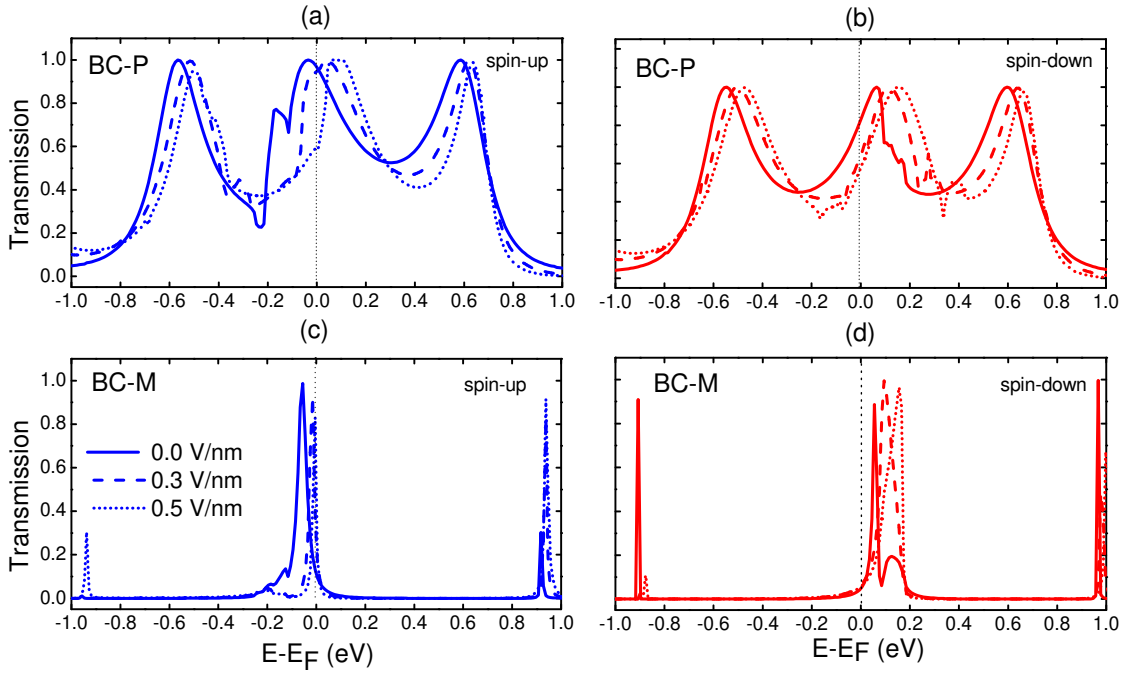

Figure 3.8: Spin dependent transmission spectra under external electric field 0.0, 0.3 and 0.5 V/nm. (a) and (b) the BC-P system. (c) and (d) the BC-M system, for spin-up and spin-down, respectively.

Table 3.1: The Spin Filter Efficiency (SFE) for BC-P and BC-M systems with electric field transverse the systems in x-axis.

Electric Field (V/nm)	BC-P SFE(%)	BC-M SFE (%)
0.0	9	27
0.3	18	70
0.5	3	88

with E_{F}, resulting in high SFE. The strong spin filtering is due to the energy separation between the narrow spin-up and spin-down transmission peaks in this system.

Chapter 4

Electronic transport in conjugated chains with DA groups

4.1 Introduction

Since the pioneering work of Aviram and Ratner [4] on molecular push-pull systems with a donor (D) and an acceptor group (A) bonded via a carbon bridge, electric rectification in molecular systems has been extensively studied by a large number of researchers. One example is the work of Carter [123] on the size reduction of architecture devices. There, the promising switching mechanism is driven by electron tunneling in periodic structures and by soliton switching in conjugated molecules. The first experimental molecular rectifier was proposed by Martin and co-workers [124]. It consisted of a conjugated zwitterionic molecule with platinum and magnesium electrodes. In a different setup, Kergueris et al. [125] showed experimental and theoretical symmetric I-V behavior of thiophene derivatives capped on both sides with sulfur atoms and connected with a gold array. These measurements indicated that nA currents at room temperature can be established in two distinct regimes: a linear regime at bias lower than 0.1 V and a nonlinear regime at voltage higher than 0.1 V. Similarly, experimental and a theoretical study of a benzenedithiolate derivative has shown an increase of rectification at μA currents but without a pronounced field effect transistor (FET) signature [72].

In 2005, several experimental studies indicated that ionic molecules may act like molecular devices and drive the electron transport through biological molecules [126]. Other ob-

servations include a molecular switch controlled by external voltage with nA currents [127], inorganic nanowires as solar cells [128], and a switching device via oxidation/reduction of the molecules between low and high conductance states [129]. Switching rectification with increased conductivity has also been observed and correlated to conformational changes (isomerization from trans to cis induced by an external voltage) of the subject molecule [130].

Specific rules related to the electronic conduction properties of molecules connected to metallic contacts have been derived from extensive theoretical work. For example, a molecular structure composed of gold attached on both sides of a dithiol derivative molecule was examined using density functional theory (DFT) and nonequilibrium Green Function formalism [7]. This study revealed a significant conductance resonance for single and double gold atom connections. The same results were found when increasing the molecule-gold lead separation. A similar methodology was utilized to investigate the mechanism of conduction in thiophene-thiazole rings, showing a rectification mechanism similar a diode-like effect. This phenomenon was explained by a resonant coupling of the electron transfer and by the localized signature of the wave functions for the bound resonant states at the applied voltage [131]. The conduction mechanism in phenylene-ethylene oligomers was examined with a different approach using quasiatomic minimal basis set molecular orbitals where it was shown that the LUMO states are mainly responsible for the conduction mechanism [132]. Also, several experimental studies have discussed the properties of a dielectric nanowire encapsulated in a self-organized gold nanoparticle chain [133] and have also investigated the nature of the interactions between metal electrodes and the organic molecules [134, 135].

From the spectrum of literature discussed above it is clear that a fundamental understanding of the models for integrating metals with molecules and their intrinsic transport properties is crucial. Some years ago, Nitzan and Ratner [136] proposed seven characteristics/requirements needed for optimizing molecular junctions: (1) the temperature

dependence as a function of carrier transport; (2) the evolution of the molecular geometry during the conduction process; (3) the selectivity of junctions produced with different metallic atoms for increased conduction and change in the I-V characteristics; (4) a fundamental understanding of gating; (5) the change in behavior from a single molecule conductance compared with several molecules working together in a device; (6) effects of changing the bridge by doping or other chemical processes; and (7) the behavior in the presence of radiation.

Otherwise there is a limited number of molecular device based in magnets properties. Metal-free molecular magnets offer intriguing benefits in terms of cost, weight, and diversity in magnetic properties and ease in processing and synthesis. However most traditional molecular-based magnets are crystals composed of molecular units that contain a variety of metals or radical.In [137] some studies have been shown that the STM is a powerful candidate to understand the basic mechanism of the magnetic interaction between a molecule and a substate but it is not a device fabrication platafom. In contrast two and three-terminal junctions incorporating magnetic molecules are closer to real devices since both the spin and charging state of the molecule can be altered.

We discussed in chapter 3 that carbon nanoribbon has shown that their magnetic properties as well as spin polarized transport might be a great solution for creating an organic device with magnetic properties and as we know organic free radicals can be good candidates to this application. However, they are very few are stable enough to be used as magnetic devices. We showed that a particular class of organic molecules, containing no radicals or metals, shows a stable magnetic on ground-state [140]. These molecules are zwitterions (betaines) separeted by polyacetylene bridge. The conjugation (π) are in general good candidates for exhibiting magnetic order, [139] but in this betaine system the magnetic properties are independent of the bridge length. [140]. Nevertheless, to preserve these stable magnetic ground-state after coupling at the metallic electrode is a extremely complicated and the difficulties extend beyond of metal/organic coupling. Issues for that

reason we combine the *para* conection (PC) and *meta* conection (MC) systems with this betaine groups.

In this chapter we will show some electronic properties and the transport for PC-DA and MC-DA systems (See figure 4.1)

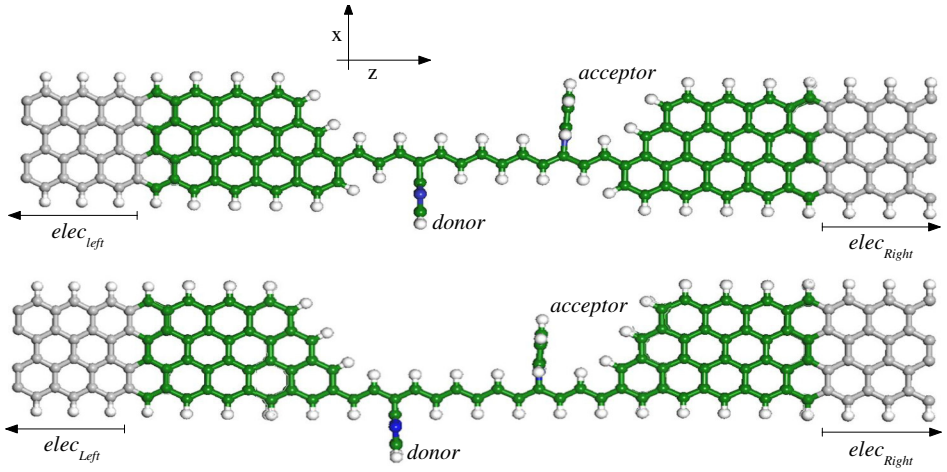

Figure 4.1: Systematic two-probe transport geometry. The central scattering region contains the polyacetylene bridge as well as several buffer layers of each electrode with betaines gorups coupled on the bridge. The shaded regions include the two semi-infinite electrodes. Geometries showing (top) the connection of the polyacetylene bridge to ZGNR to make the PC-DA (*para* connection with donor (D) and acceptor (A) in the bridge) system and (bottom) the connection to form the MC-DA (*meta* connection with DA).

The donor/acceptor groups are coupled in the bridge at specific A/B sublattice carbon. The geometry were structurally prepared in a way that has a bond C-C for donor group at the A carbon sublattice and C-N for acceptor group at B carbon sublattice. How these A/B sublattice carbon atoms influence the propeties of the systems was thoroughly discussed in Chapter 3. We are interested in spin transport properties which includes analysis of density spin polarization in different parts of the geometry under an external electric field and in I-V curves where we range the bias in interval of [0.1,-1.0] V in a step of 0.1 V, performing a self-consistent calculation for each bias. The electron transmission around the Fermi energy was calculated also at zero bias $[T_\sigma(E, V = 0)]$, under the $(\vec{E}_{ext})$ by integrating the transmission coefficient T(E) at zero bias over the bias window to obtain the I-V curves [141, 142]. In this case we consider $(\vec{E}_{ext})$ as a gate voltage.

4.1.1 The donor/acceptor groups

The betaine derivatives are zwitterions with a π-conjugated structure whose variable π bridge length separates the donor and acceptor groups. This molecular system that is composed entirely of C, N and H has a magnetic ground-state. The betaine derivatives are unique because they also have an intrinsic donor and π acceptor at different ends of the molecule. The magnetic properties of these systems are independent of the bridge length [140]. The molecular structure for the betaine derivatives is shown in Fig. 4.2, where the acceptor group (A) is a pyridine (cation) and the donor group (D) is a imidazole (anion) separated by a variable length π-conjugated (polyacetylene). Small pyridinium betaines have large molecular hyper polarizabilities relative to their molecular sizes [143].

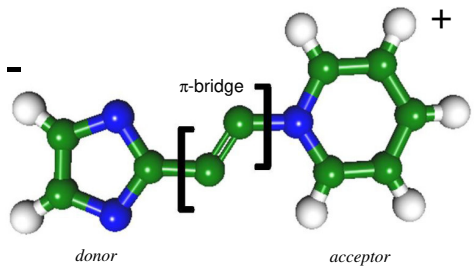

Figure 4.2: A zwitterionic betaine molecule with an imidazol donor (D) and a pyridine acceptor (A) separated by alternating C=C bridge.

In particular, we have demostrated that this molecule with large bridge exhibits an effect of inversion of charge flow from A to D. This is expected to have important consequences not only on the optical, but also on several other electronic properties of these betaines, which constitute a new class of push-pull systems [144]. In addition, previous results demonstrated that these compounds have a surprisingly strong local Heisenberg type magnetic character that originates from the conjugated bridge in cooperation with the donor-acceptor character of the molecule. The localized behavior found in this system is compatible with the π conjugation of the components making up the system, the reason for this is that the anti-ferro magnetic state (Afm) state further stabilizes the

system because the Coulomb energy is diminished by alternating the spins throughout most of the system. Thus, the stabilization of the system is achieved by the resonating nature of the charge density (kinetic energy) and the localization of the Afm state that results in a reduction of the Coulomb energy. The Afm type ordering found on the conjugated bridge is critical in establishing the shortrange local interactions with the donor and acceptor ring structures and the resulting lack of long-range interaction between them. These features are responsible for the stable magnetic configuration as a function of bridge length and could possibly enable the development of a variety of magnetic devices. Furthermore, the magnetic character is not disrupted by conformational disorder. Stable room temperature molecular magnetic materials that are purely organic are rather rare and the betaine derivatives promise to offer a new class of molecular magnetic materials with diverse potential applications including organic spintronics information storage and nanoscale sensors [140].

4.1.2 Hybridization in PC-DA and M-DA

A transverse external electric field ($\vec{E}_{ext}$) varying from 0.0 V/nm to 0.5 V/nm was applied across the PC-DA and MC-DA systems along the x-axis (in-plane). The difference of electrostatic potential at the edge of 4ZGNRs creates a spin polarization (half-metallicity) in the system under $\vec{E}_{ext}$. [145] Important results have been found that the spin-orbit coupling in carbon nanoribbon systems is extremely weak under the magnetic fields and the current-carrying electrons might be controlled under transverse electric field [146]. When the stimulus has a magnetic origin, then the direction is more complicated, simply because a magnetic field is less efficient then an electric field for driving the electron motion [147]. In Fig. 4.3 we show a plot of charge transfer vs. transverse electric field ($\vec{E}_{ext}$) for PC-DA and MC-DA coupled at 4-ZGNRs electrodes. The panel (a) contains the donor groups of the molecular structure PC-DA and MC-DA systems; for the donor group the majority of carriers decreases as a the electric field is applied. At the bridge (panel (b)) we find a small variation only for the MC-DA system; while for the acceptor group, (panel (c))

the majority carriers increases. These results reveal that the charge accumulation can provide, information about charge transfer between D-A groups from left electrode to right electrode crossing the overall system.

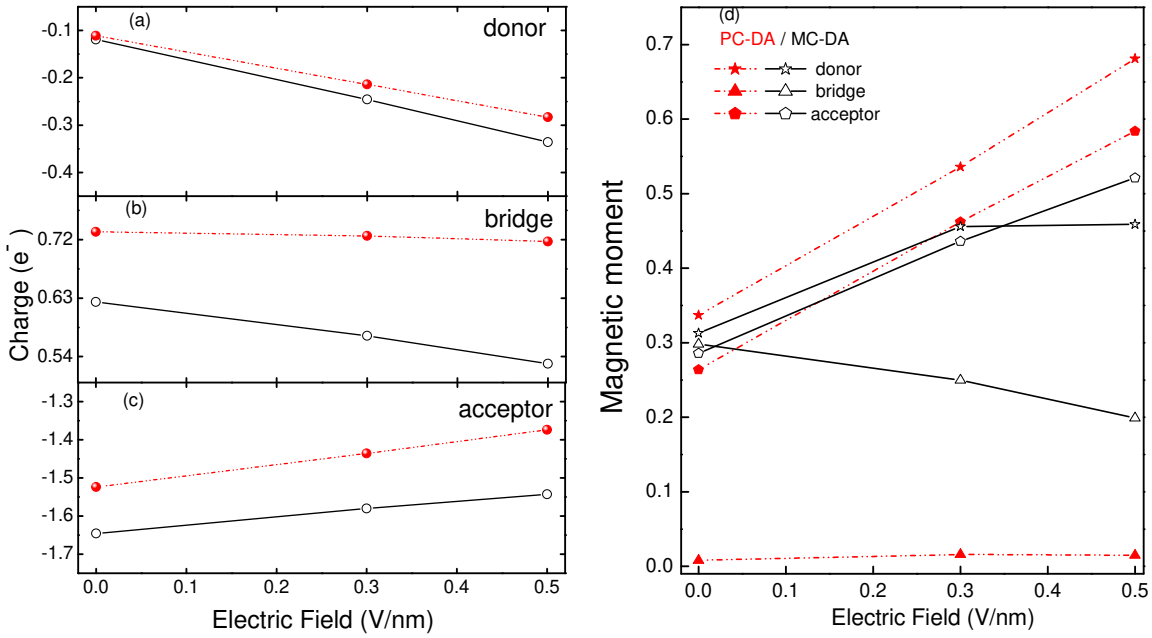

Figure 4.3: The BCP-DA (•) and BCM-DA (○) systems (left side). The charge accumulations for different parts (a) donor, (b) bridge and (c) acceptor. (d) The magnetic moment (μ_B) for DA groups and bridge. Both (charge and μ_B) as a function transverse of electric field.

Fig. 4.3(d) shows the results for the PC-DA and MC-DA systems in the AF ordering where we localized the local magnetic moments for total carbons at the bridge and DA groups. For the PC-DA system the magnetic moment of the groups (DA) as a function electric field increases considerably at the range 0.0 to 0.5 V/nm ($\approx 0.4\ \mu_B$) while in the bridge the invariance around zero of the μ_B under the electric field indicates that the DA groups in this case only interact locally with the first couple of carbon atoms in the bridge. Thus, it seems that the groups D and A in the PC-DA system exhibit the AF ordering independent of the magnetic states of the bridge. The MC-DA system shows a smaller variation for magnetic moment ($\approx\ 0.2\mu_B$); in this case the downfall at magnetic moment of the bridge at 0.5 V/nm induces the change in the D group. As is expected due the position of the bridge (*meta*-linkage) their influence on the groups is considerable.

The density of states around Fermi energy can determine the magnetic properties of the system [84]. For that reason, we focus on the PDOS around the Fermi energy, which is set to zero. As we known, the carbon nanoribbon exhibits half-metallicity under the electric field and we have showed that this half-metallicity is preserved for PC and MC systems.

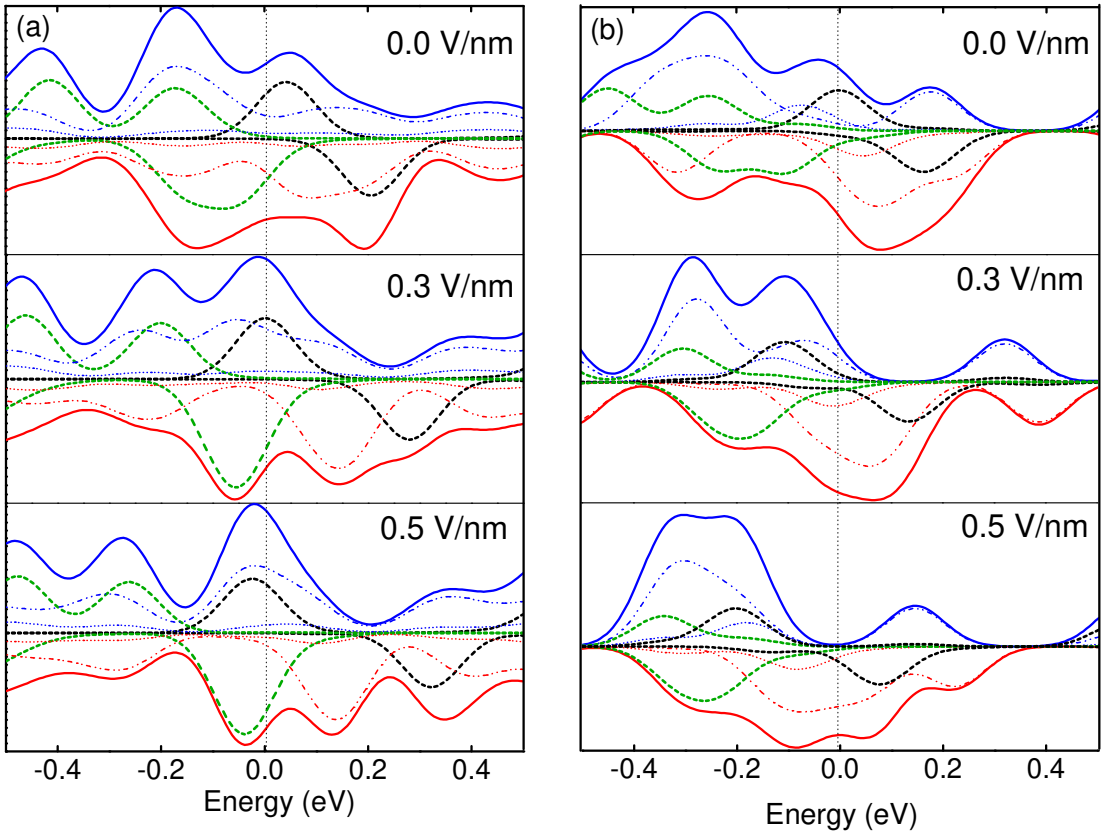

Figure 4.4: Projected density of states for (a) PC-DA and (b) MC-DA systems under the transverse electric field (x-axis). The different parts of system are: 4-ZGNRs (dash-dot-dot), π-bridge (shot-dot), D (short-dash-dot green) and A (dash-dot black). The solid lines (positive and negative) represent the total DOS for spin-up and spin-down respectively.

The PC-DA system has zero magnetic moment to the bridge even under the transverse electric field. In Fig. 4.3(a) the projected density of states at zero field for DA groups exhibits a peaks around the Fermi energy. The peak that correspond the acceptor group shift to the Fermi energy under the $\vec{E}_{ext}$ while the peak for D group presented a small shift and broadening around the Fermi energy. The MC-DA (Fig. 4.3(b)) shows a pronounced

contribution to the bridge under the $\vec{E}_{ext}$. For the donor and acceptor contribution there are peaks around the Fermi energy. These peaks under $\vec{E}_{ext}$ shift to the Fermi energy and clearly reflects that the electrons can be transferred to and from 4-ZGNRs leads.

4.1.3 PC-DA and MC-DA organic devices

The use of single molecule as functional device is the ultimate and the on going trend towards the miniaturization of electronic circuits. Some studies proposed a novel mechanism to control electron transport through single molecular rings: the current is determined by thr degree of destructive or constuctive quantum interference (QI) between the two paths around a symetric molecule [148, 149].

For the PC-DA system the transmission spectrum T(E) is shown in Fig. 4.5(a). At zero bias the high T(E) is $\approx$1 as we expected since the 4-ZGNRS and π-DA groups are symmetric. The spin-up (blue-short dash) exhibits a perfect and destructive QI around -0.2 eV. This anti-resonant peak (narrow dip) follows a resonant broad peak around the Fermi Energy. For spin-down (red-solid) we found two anti-resonant peaks between -0.2 eV to 0.0 eV . The dip around $\varepsilon_F = 0$ indicates an effective destructive interference. In Fig. 4.5(b) we show that I-V curves for spin up and spin-down carries are similar. The current increases under the bias between 0.0 V to 0.2 V then goes down until 0.5 V and increases after this value. In this voltage range we found an interesting negative differential resistance (NDR) characteristic induced by QI mechanism.

In the MC-DA system (Fig. 4.5(c)) for spin-up there is a resonant peak in T(E) around the Fermi energy and this peak represent a constructive QI. For spin-down the transmission spectrum exhibits a rather narrow peak at $E_F = 0$ eV and other peak near to small feature. The I-V curve in Fig. 4.5(d) has characteristic that resembles a field effect device, that is, for spin-down the current firstly increased when applying a bias voltage from 0.0 to 0.2 V and decreases until zero with voltage from 0.3 to 1.0 V . For spin-down the current as a function of voltage from 0.0 to 0.2 V also increases but the current for spin-down is smaller than that of spin-up carries. Before the current goes down it presents

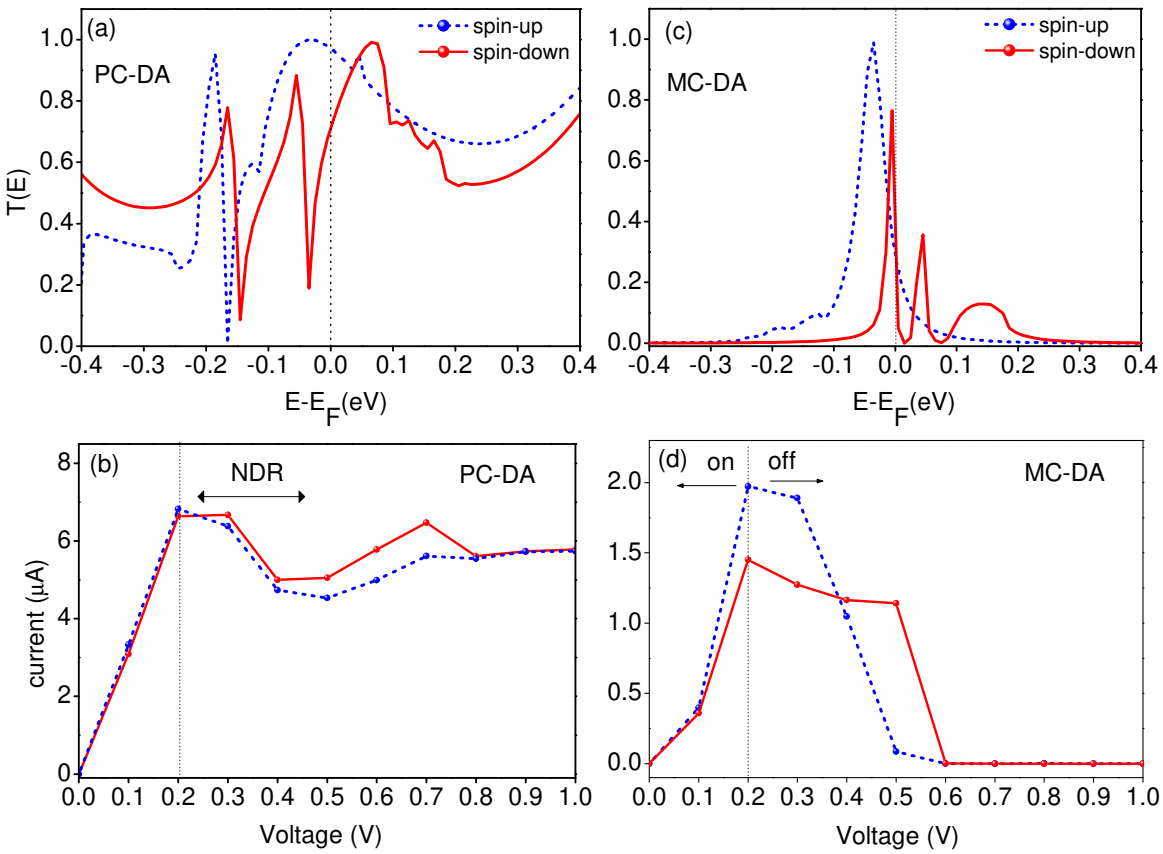

Figure 4.5: Transmission spectrum as a function of energy and current as a function of voltage for the PC-DA and MC-DA. Spin-up and spin-down are represented in short-dash blue and solid line red respectively.

a saturation region between 0.2 to 0.5 V being $\approx$ 1.3 μA.

Is important to note that the MC-DA systems represent the constructive QI effects while the PC-DA represent destructive QI. The effects related with quantum interference usually might be controlled by third terminal with a gate voltage [5]. In this case we have great advantages due the strong coupling (C-C) between bridge and 4-ZGNRs (*meta*/*para*-linkages). Our calculations demonstrate that is possible to control these QI effect with the transverse electric field as a gate voltage. The electron transmission around the Fermi energy was calculated also at zero bias $[T_\sigma(E, V = 0)]$ and under the $(\vec{E}_{ext})$ where integrating the transmission coefficient T(E) is integral at zero bias over the bias window to obtain the I-V. In this case we consider $(\vec{E}_{ext})$ as a gate voltage.

In Fig. 4.6 the spectrum transmission for different intensity of electric field (0.0, 0.3

and 0.5 V/nm) applied transversely to the system. Fig. 4.6 shows for spin-up in panel (a) that the QI peak moves to -0.2 eV under the field 0.3 V/nm and disappear completely for $\vec{E}_{ext} = 0.5$ V/nm. For the spin-down (panel (b)), the transmission spectrum shows that for $\vec{E}_{ext} = 0.3$ V/nm the peaks of QI decreases the width and continues around the Fermi energy while for $\vec{E}_{ext} = 0.5$ V/nm, the width of peaks increase and these peaks start to lose definition. In both cases (spins up/down) the destructive quantum interference can be suprssed by applying transverse electric field higher than 0.5 V/nm and in (spin up/down) the current increases from 0.0 to 1.5 V and around 1.5 to 3.5 V reaches a saturation.

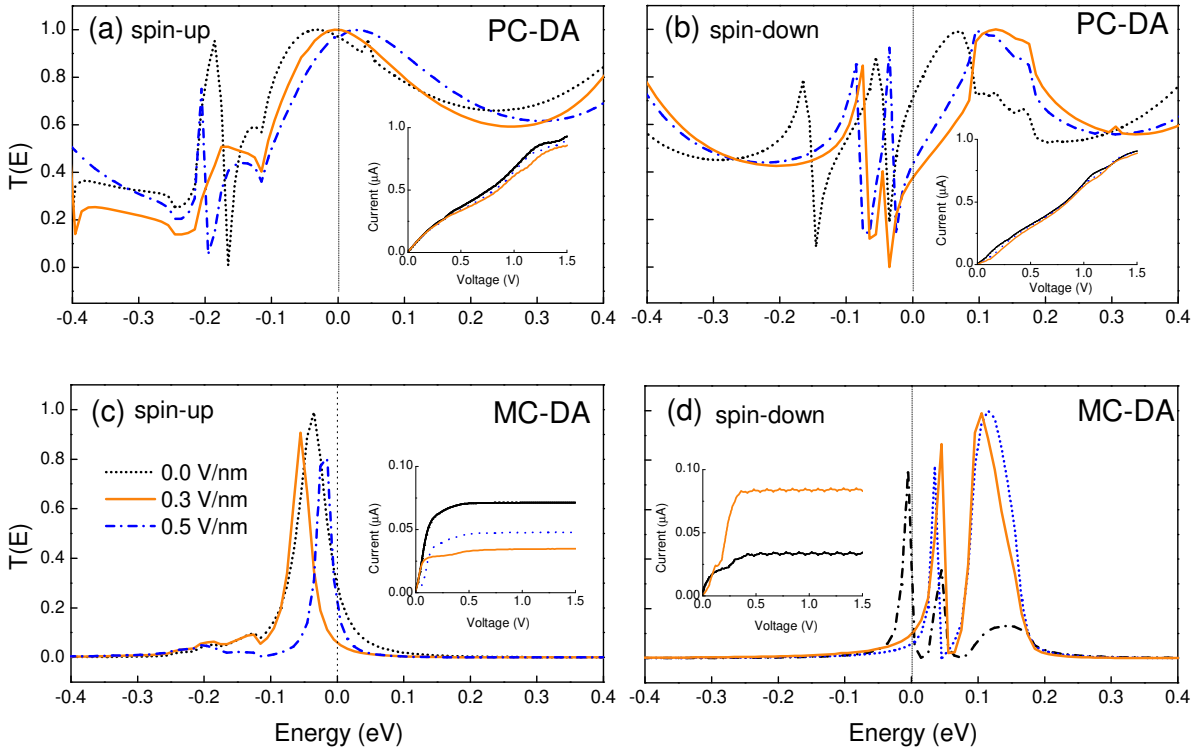

Figure 4.6: The transmission spectra for two-probe systems.(a) and (b) corre

The panel (c) shows spin-up for MC-DA system in here the transmission peak around the Fermi energy after applying an electric field of 0.3 V/nm the narrow peak increases their width and under an electric field of 0.5 V/nm decreases the width and moves closer to the Fermi energy. The transmission spectrum in panel (d) is quite different around

Fermi energy for spin down; the two narrow peaks combine in only one and the small feature under the electric field 0.3 and 0.5 V/nm, resulting in a broader peak at the same range of energy. For MC-DA under $\vec{E}_{ext}$ the current has a small operation and a large saturation region from 0.5 to 3.5 V. The integral of T(E) at zero bias is a good information only when the variation into the conduction window is small as we showed for both systems but as we expect the constructive and destructive QI and the spin filter properties is preserved under a transverse electric field.

Chapter 5

Conclusions

In this Thesis we studied electronic and transport properties of different molecular systems by using ab initio models and non-equilibrium green function technique (NEGF). We use modeling for studying the self-assmbled monolayers of two aromatic molecules deposited on gold surface and transport through conjugated chains connected by carbon nanoribbons electrodes.

In chapter 2 where we have dicussed about one possible erroneous interpretation of STM images in self assembled monolayers on metal surface our last remaks are: HPYT and HPOT are aromatic thiols that adsorb on gold and are able to lift the $22x\sqrt{3}$ reconstruction, forming a slightly distorted $\sqrt{3}x\sqrt{3}R30^o$ structure. The images of STM do not show clear distinction between the two molecules. The images were obtained with high tunneling resistance to avoid layer disruption. In this work we report a comparison between experimental STM measurements of HPYT and HPOT molecules adsorbed on gold with DFT-based calculations of the local density of states and with a simple quantum transport model based on the master equation technique. We suppose that the HPOT and HPYT molecules are attached to the carbon atom by an S-Au bond and that the molecule is tilted relative to the gold surface giving the impression, in the STM measurements, that the molecules are sitting at the three fold hollow site. Striking similarity was found between the STM image and the LDOS calculated by DFT. Finally, we have shown that the quantum transport model used is able to interpret the main features of the molecule-assisted tunneling between the tip and the gold surface.

In chapter 3 and 4 we have used NEGF-DFT to study ZGNRs/polyacetylene coupling in molecular contact. The coupling resulting in a local *para*-linkage benzene (BC-P system) or in a local *meta*-linkage benzene (BC-M system). Nevertheless some combinations of carbon nanoribbon do not return transmissions values as high as what we find in BC-P system. We find also that the channel transmission in BC-M system can be controlled with an external electric field. What we observed here is relevant and to the best of our knowledge it has never been reported before in zigzag graphene nanoribbons. With the application of an external electric field, we find that the BC-P system, which is metallic at zero field, remains metallic. On the other hand, for the BC-M system (semiconductor), an external electric field shifts states to the Fermi energy, and this causes the system to become conducting under a sufficient electric field. The nature of system (conductor or semiconductor) can be controlled in the molecular junction and the high transmission can be explained by using *para* vs *meta* configuration of the benzene-like ring which is bonded to the carbon chain.

Finally, we present here the proof-of-concept on how to build switches and spin filters devices based on polyacetylene chains between carbon nanoribbons electrodes. We demonstrated also that DA groups attached to molecular bridge offer the possibility to modify the transmission probability of BCP and BCA systems in a controlled way. Whereas our study is under the bias in interval of [0.1,-1.0] V in a step of 0.1 V, performing a self-consistent calculation for each bias the systems are completly described. It is possible, for instance, to introduce the groups with magnetic properties and keep the spin polarized, such that up-spin and down-spin orbitals have different energies. This facilitates the construction of a spin valve that lets spin-up or spin-down electrons to move while one is blocking.

In this thesis simulations unveiled that is possible an erroneous interpretation of STM images in self assembled molecule monolayers on metal surface. The understanding of the fundamental interactions between organic molecules and metal surface is of crucial im-

portance in molecular scale electronics and self-assembly, where the competition between molecule-substrate and intermolecular interactions can lead to templates arrangements with specific spectroscopic and transport properties. On that basis, we propose further investigation using density functional theory with the nonlocal van der Waals density functional and the semilocal Perdew-Burke-Ernzerhof functional to find absorption and binding energies for the thiol molecules described in chapter 3. This can be an effective way of understanding the nature of the coupling between metal and molecule in the electronic transport. Regarding the conjugated chain coupled to donor and acceptor groups and bonded to carbon nanoribbons, there are many things to be investigated, becouse the electrical conductance behavior through these systems investigated depends on the nature of the molecular groups. In this case studies where DA groups can change the position on the bridge should be interesting to investigated these systems along with dangling bonds at 4-ZGNRs and in the bridge.

Appendix A

Publication

The work presented in this thesis has been carried out at the Departamento de Física da Universidade Federal do Ceará, Brazil and Department of Chemistry Northwestern University, USA.

A.1 List of papers included in the thesis

Paper I A. Saraiva-Souza1; L. S. Pinheiro, F. W. N. Silva, E. B. Barros, J. S. de Sousa, J. Mendes Filho, J. Del Nero, F. M. Souza, Mark A. Ratner and A. G. Souza Filho, Scanning tunneling microscopy images and charge transport in two molecular periodic arrays, submited.

Paper II Aldilene Saraiva-Souza, Manuel Smeu, H. Terrones, A. G. Souza Filho and Mark A. Ratner, Spin transport of polyacetylene chains bridging zigzag graphene nanoribbon electrodes: structural control and spin filtering, submited.

Paper III Aldilene Saraiva-Souza, Manuel Smeu, A. G. Souza Filho and Mark A. Ratner, Electron transport through Fano resonances in of polyacetylene chains bridging DA groups connected to Graphene nanoribbon electrodes, in preparation.

A.2 List of papers not included in the thesis

Paper IV W. A. Shelton, E. Apra , B. G. Sumpter, A. Saraiva-Souza, A. G. Souza Filho, J. Del Nero, V. Meunier, Theory of zwtterionic molecular-based organic magnets,

Chemical Physics Letters 511, 294-298 (2011).

Paper V MENEZES, M.; SARAIVA-SOUZA, A.; DEL NERO, J.; CAPAZ, R.B.; Proposal for a Single-Molecule Field-Effect Transistor for Phonos, Phisical Review B - Condensed Matter and Materials Physics, American Physical Society. v. 81, p. 012302 (1-4), 2010. Selected paper for virtual Journal of Nanoscale Scienc and anTechnology, 21 (4), (2010).

Paper VI A. Saraiva-Souza, F. M. Souza, V. F. Aleixo, E. C. Girao, J. Mendes Filho, Sumpter, B.G.; Meunier, A. G. Souza Filho, J. Del Nero, A Single Molecule Rectifier with Strong Push-Pull Coupling, The Journal of Chemical Physics, 129, p. 204701 (2008).

Paper VII A. Saraiva-Souza, Sumpter, B.G.; Meunier, A. G. Souza Filho, J. Del Nero, Electrical Rectification in Betaine Derivatives, Journal of Physical Chemistry C American Chemical Society, v. 112, p. 12008, (2008)

Paper VIII A. Saraiva-Souza, F. M. Souza, G. Baldissera, W. E. Silva, L. S. Roman, J. Mendes Filho, J. Del Nero, A. Fazzio and A. G. Souza Filho, Light emission and current rectification in a molecular device: experiment and theory, in press.

Bibliography

[1] Wong, H. S.; Durkan, C.; Chandrasekhar, N. *ACS Nano* **3**, 3455 (2009).

[2] Seferos, D. S.; Blum, A. S.; Kushmerick, J. G.; Bazan, G. C. *J. Am. Chem. Soc.* **128** 11260 (2006).

[3] Damle, P. S.; Ghosh, A. W.; Datta, S.; *Chem. Phys.* **281**, 171 (2002).

[4] Aviram, A.; Ratner, M. A. *Chem. Phys. Lett.* **29**, 277 (1974).

[5] Reed, M. A.; Zhou, C.; Muller, C. J.; Nurgin, T. P.; Tour, J. M. *Science* **278**, 252 (1997).

[6] Datta, S. *in Electronic Transport in Mesoscopic System*, edited by Ahmed, H.; Pepper, M.; Broers, A. (Cambridge University Press, Cambridge, England, **1995**).

[7] Di Ventra, M. *Eletrical Transport in Nanoscale Systems. Cambridge University Press*, (2008).

[8] Samanta, M. P.; Tian, W.; Datta, S.; Henderson, J. I.; Kubiak, C. P. *Phys. Rev. B* **51**, R7626 (1996).

[9] Damle, P. S.; Ghosh, A. W.; Datta, S. *Phys. Rev. B* **64**, 201403 (2001).

[10] Yaliraki, S. N.; Kemp, M.; Ratner, M. A. *J. Am. Chem. Soc.* **121**, 3428 (1999).

[11] Xu, B.; Tao, N. J. *Science*, 301, 1221 (2003).

[12] Gross, L.; Moll, N.; Mohn, F.; Curioni, A.; Meyer, G.; Hanke,F.; Persson, M. *Phys. Rev. Lett.* **107** 086101 (2011).

[13] Geim, A. K. *Sience* **324**, 1530 (2009).

[14] Fuhrer, M. S.; Lau, C. N.; MacDonald, A. H. *MRS Bulletin* **35**, 289 (2010).

[15] Fuhrer, M. S. *Nature MAterials* **9**, 611 (2010)

[16] Nakada, K.; Fujita, M.; Dresselhaus, G.; Dresselhaus, M. S. *Phys. Rev. B* **54**, 17954 (1996)

[17] Son, Y. W.; Cohen, M. L.; Louie, S. G. *Phys. Rev. Lett.* **97**, 216803 (2006)

[18] Son, Y. W.; Cohen, M. L.; Louie, S. G. *Nature* **444**, 347 (2006).

[19] Kim, W. Y.; Kim, K. S. *Nat. Nanotechnol.* **3**, 408 (2008).

[20] Zhang, Z.; Chen, C.; Guo, W. *Phys. Rev. Lett.* **103**, 187204 (2009).

[21] Jin, C. H.; Lan, H. P.; Peng, L. M.; Suenaga, K.; Iijima, S. *Phys. Rev. Lett.* **102**, ??? (2009) .

[22] Chuvilin, A.; Meyer, J. C.; Algara-Siller, G.; Kaiser U. *New J. Phys.* **11**, 083019 (2009)

[23] Taylor, J.; Guo, H.; Wang, J. *Phys. Rev. B.* **63**, 245407 (2001).

[24] Barth, U. V.; Hedin, L. *J. Phys. C* **5**, 1629 (1972).

[25] Pant, M. M.; Rajagopal, A. K. *Solid State Commun.* **10**, 1157 (1972).

[26] Szabó, A.; Ostlund. N.S. **odern quantum chemistry: introduction to advanced electronic structure theory**. Dover Publications, (1996).

[27] Martin, R. M. **Electronic Structure: Basic Theory and Practical Methods**. Cambridge University Press, (2004).

[28] Katrina S. *Phys. Rev. A* **52**, 3397 (1995).

[29] Wang, J.; Stuchebrukhov, A. A. *J. Quantum Chem.* **80**, 591 (2000).

[30] Ashcroft, N. W.; Mermin. N. D. S. **olid state physics. Holt-Saunders International Editions: Science : Physics**. Holt, Rinehart and Winston, (1976).

[31] Payne, M. C.; Teter, M. P.; Allan, D. C.; Arias, T. A.; Joannopoulos. J. D. *Rev. Mod. Phys.* **64**, 1045 (1992).

[32] Hohenberg, P.; Kohn, W. *Physical Review* **136**, 864 (1964).

[33] Vosko, S. H.; Wilk, L; Nusair, M. *Canadian J. Phys.* **58**, 1200 (1980).

[34] Keldysh, L. V. *Sov. Phys. JETP* **20**, 1018 (1965).

[35] Kadanoff, L. P.; Baym, G. *Quantum Statistical Mechanics, Green's Function Methods in Equilibrium and Nonequilibrium Problems*, Benjamin Cummings Publishing Company (1962).

[36] Landauer, R. *IBM J. Res. Dev.* **1**, 223 (1957).

[37] Landauer, R. *IBM J. Res. Dev.* **32**, 306 (1988).

[38] Buttiker, M. *IBM J. Res. Dev.* **32**, 317 (1988).

[39] Buttiker, M. *Phys. Rev. B* **38**, 9375 (1988).

[40] Rabaud, W.; Saminadayar, L.; Mailly, D.; Hasselbach, K.; Benoît, A.; Etienne.; B. P. *Phys. Rev. Lett.***86**, 3124 (2001).

[41] Soler, J. M.; et al. *J. Phys.: Condens. Matter* **14**, 2745 (2002).

[42] Kohn, W.; Sham. L. J. *Phys. Rev.* **140**, 1133, (1965)

[43] Basch, H.; Cohen, R.; Ratner, M. A.; *Nano Lett.* **5**, 1668 (2005).

[44] Frei, M.; Aradhya, S. V.; Koentopp, M.; Hybertsen, M. S.; Venkataraman, L. *Nano Lett.* **11**, 1518 (2011).

[45] Li, G.; Tamblyn, I.; Cooper, V. R.;Gao, H.-J.; Neaton, J. B. *Phys. Rev. B* **85**, 121409 (2012).

[46] Hofmann, O. T.; Egger, D. A.; Zojer, E.; Nano Lett. **2010**, 10, 4369.

[47] Datta, S.; Tian, W.; Hong, S.; Reifenberger, R.; Henderson, J. I.; Kubiak, C. P. *Phys. Rev. Lett.* **79**, 2530 (1997).

[48] Thygesen, K. S.; Rubio, A. *Phys. Rev. Lett.* **102**, 046802 (2009).

[49] Paulsson, M.; Frederiksen, T.; Ueba, H.; Lorente, N.; Brandbyge, M. *Phys. Rev. Lett.* **100**, 226604 (2008).

[50] Binnigt. , G.; Rohrer, H. *Rev. Mod. Phys.* **59**, 615 (1987).

[51] Odom, T. W.; Huang, J-L.; Kim, P.; Lieber. C. M. *Nature* **391**, 62 (1998).

[52] Tersoff, J.; Hamann, D. R. *Phys. Rev. B* **31**, 805 (1985).

[53] Wang, Y.-T.; Tang, G.-M.; Qiang, Z.-W. *Polyhedron* **26**, 4542 (2007).

[54] Tripathi, P.; Pal, A.; Jancik, V.; Pandey, A. K.; Singh, J.; Singh, N. K. *Polyhedron* 26, 2597 (2007).

[55] Han, P.; Kurland, A. R.; Giordano, A. N.; Nanayakkara, S. U.; Blake, M. M.; Pochas, C. M.; Weiss, P. S. *ACS Nano* **3**, 3115 (2009).

[56] Zhenyu, L.; Kosov, D. S. *Phys. Rev. B* 76, 035415 (2007).

[57] Tian, W.; Datta, S.; Hong, S.; Reifenberger, R.; Jason, I.; Kubiak, C. P. *J. Chem. Phys.* **109**, 2874 (1998).

[58] Gurvitz, S. A. *Phys. Rev. B* 57, 6602 (1998).

[59] We extend the formulation developed in Ref. [60] to account for many conducting sites.

[60] Djuric, I.; Dong, B.; Cui, H. L. *IEEE Trans. on Nanotech.* 4, 71 (2005).

[61] Haug, H.; Jauho, A. P. *Quantum Kinetics in Transport and Optics of Semiconductors*, Second Edition, Springer (2008).

[62] Liu, Y.; Li, H.; Tu, D.; Ji, Z.; Wang, C.; Tang, Q.; Liu, M.; Hu, W.; Liu, Y.; Zhu, D. *J. Am. Chem. Soc.* **128**, 12917 (2006).

[63] Lu, J.; Zhang, H.; Shi, W.; Wang, Z.; Zheng, Y.; Zhang, T.; Wang, N.; Tang, Z.; Sheng, P. *Nano Lett.* **11**, 2973 (2011).

[64] Kitaura, R.; Imazu, N.; Kobayashi, K.; Shinohara, H. *Nano Lett.* **8**, 693 (2008).

[65] Campos, L. C.; Manfrinato, V. R.; Sanchez-Yamagishi, J. D.; Kong, J.; Jarillo-Herrero, P. *J. Am. Chem. Soc.* **9**, 2600 (2009).

[66] Guo, B.; Liu, Q.; Chen, E.; Zhu, H.; Fang, L.; Gong, J. R. *J. Am. Chem. Soc. Nano Lett.* **10**, 4975 (2010).

[67] Agapito, L. A.; Kioussis, N. *J. Phys. Chem. C* **115**, 2874 (2011).

[68] Nakada, K.; Fujita, M.; Dresselhaus, G.; Dresselhaus, M. S. *Phys. Rev. B* **54**, 17954 (1996).

[69] Tanaka, K.; Yamashita, S.; Yamabe, H.; Yamabe, T. *Synthetic Metals* **17**, 143 (1987).

[70] Stein, S. E.; Brown, R. L. *Journal of the American Chemical Society* **109**, 3721 (1987).

[71] Ezawa, M. *Physical Review B* **73**, 045432 (2006).

[72] Castro Neto, A. H.; Guinea, F.; Peres, N. M. R.; Novoselov, K. S.; Geim, A. K. *The Am. Phys. Soc.* **81**, 109 (2009)

[73] Nakada, K.; Fujita, M.; Dresselhaus, G.; Dresselhaus, M. S. *Phys. Rev. B* 54, 17954 (1996).

[74] Stein, S. E.; Brown, R. L. *J. Am. Chem. Soc.* **109**, 3721 (1987).

[75] Son, Y.-W.; Cohen, M. L.; Louie, S. G. *Nature* **444**, 347 (2006).

[76] Son, Y.-W.; Cohen, M. L.; Louie, S. G. *Phys. Rev. Lett.* **97**, 216803 (2006).

[77] Ritter, K. A.; Lyding, J. W. *Nature Materials* **8**, 235 (2009).

[78] Rudberg, E.; Salek, P.; Luo, Y. *Nano Lett.* **8**, 2211 (2007).

[79] Wimmer, M.; Adagideli, I.; Berber, S.; Toánek, D.; Richter, K. *Phys. Rev. Lett.* **100**, 177207 (2008).

[80] Evaldsson, M.; Zozoulenko, I. V.; Xu, H.; Heinzel, T. *Phys. Rev. B* **78**, 161407 (2008).

[81] Shen, X.; Sun, L.; Benassi, E.; Shen, Z.; Zhao, X.; Sanvito, S.; Hou, S. *J. Chem. Phys.* **132**, 054703 (2010).

[82] Smeu, M.; DiLabio, G. A. *J. Phys. Chem. C* **114**, 17874 (2010).

[83] Wu, J.-C.; Wang, X.-F.; Zhou, L.; Da, H.-X.; Lim, K. H.; Yang, S.-W.; Li, Z.-Y. *J. Phys. Chem. C* **113**, 7913 (2009).

[84] Botello-Méndez, R. A.; Cruz-Silva, E.; López-Urías, F.; Sumpter, B. G.; Meunier, V.; Terrones, M.; Terrones, H. *ACS Nano* **11**, 3606 (2009).

[85] Botello-Méndez, R. A.; Cruz-Silva, E.; López-Urías, F.; Romo-Herrera, J.; Terrones, M.; B. G.; Meunier, Terrones, H.; Charlier, J.-C.; Meunier, V. *Nano Lett.* **11**, 3058 (2011).

[86] Basch, H.; Cohen, R.; Ratner, M. A. *Nano Lett.* **5**, 1668 (2005).

[87] Frei, M.; Aradhya, S. V.; Koentopp, M.; Hybertsen, M. S.; Venkataraman, L. *Nano Lett.* **11**, 1518 (2011).

[88] Li, G.; Tamblyn, I.; Cooper, V. R.;Gao, H.-J.; Neaton, J. B. *Phys. Rev. B* **85**, 121409 (2012).

[89] Hofmann, O. T.; Egger, D. A.; Zojer, E.; *Nano Lett.* **10**, 4369 (2010).

[90] Kiguchi, M.; Nakamura, H.; Takahashi, Y.; Takahashi, T.; Ohto, T. *J. Phys. Chem. C* **114**, 22254 (2010).

[91] Hermann, C.; Solomon, G. C.; Ratner, M. A. *J. Am. Chem. Soc.* **132**, 3682 (2010).

[92] Koleini, M.; Paulsson, M.; Brandbyge, M. *Phys. Rev. Lett.* **2007**, ???,197202.

[93] Rajica, A.; Shiraishi, K.; Pink, M.; Rajca, S. *Phys. Rev. Lett.* **129**, 7232 (2007).

[94] Nichols, R. J.; Higgins, S. J. *Nature Nanotechology* **7**, 281 (2012).

[95] Hermann, C.; Solomon, G. C.; Ratner, M. A. *J. Chem. Phys. C* **134**, 224306 (2011).

[96] Hermann, C.; Solomon, G. C.; Ratner, M. A. *J. Am. Chem. Soc.* **132**, 3682 (2010).

[97] Jin, C.; Lan, H.; Peng, L.; Suenaga, K.; Iijima, S. *Phys. Rev. Lett.* **102**, 205501 (2009).

[98] Chen, W.; Andreev, A. V. *Phys. Rev. B* **80**, 085410 (2009).

[99] Chuvilin, A.; Meyer, C. J.; Algara-Siller, G.; Kaiser, U. *New J. of Phys.* **11**, 083019 (2009).

[100] Tongay, S.; Senger, R. T.; Dag, S.; Ciraci, S. *Phys. Rev. Lett.* **93**, 136404 (2004).

[101] Kohn, W.; Sham, L. *J. Phys. Rev.* **140**, 1333 (1965).

[102] Hohenberg, P.; Kohn, W. *Phys. Rev. B* **136**, 864 (1964).

[103] Soler, J. M.; Artacho, E.; Gale, J. D.; Garcia, A.; Junquera, J.; Ordejon, P.; Sanchez-Portal, J. *J. Phys: Condens. Matter* **14**, 2745 (2002).

[104] Troullier, N.; Martins, J. L. *Phys. Rev. B* **43**, 1993 (1991).

[105] Junquera, J.; Paz, O.; Sanchez-Portal, D.; Artacho, E. *Phys. Rev. B* 64, 235111 (2001).

[106] von Barth, U.; Hedin, L. *J. Phys. C* 5, 1629 (1972).

[107] Gunnarsson, O.; Lundqvist, B. I. *Phys. Rev. B* **13**, 4274 (1976).

[108] Rajagopal, A. K. J. *Phys. C* **11**, 943 (1978).

[109] Kan, E.-J.; Li, Z.; Yang, J.; Hou, J. G. *Appl. Phys. Lett* **91**, 243116 (2007).

[110] Monkhorst, H. J.; Pack, J. D. *Phys. Rev. B* **13**, 5188 (1976).

[111] Brandbyge, M.; Mozos, J.-L.; Ordejon, P.; Taylor, J.; Stokbro, K. *Phys. Rev. B* **65**, 165401 (2002).

[112] Datta, S. *Superlattices Microstruct.* **28**, 253 (2000).

[113] Yoshizawa, K.; Tada, T.; Staykov, A. *J. Am. Chem. Soc.* **130**, 9413 (2008).

[114] Deng, W.-Q.; Muller, R. P.; Goddard, W. A. *J. Am. Chem. Soc.* **126**, 13562 (2004).

[115] Shen, L.; Zeng, M.; Yang, S.-W.; Zhang, C.; Wang, X.; Feng, Y. *J. Am. Chem. Soc.* **132**, 11481 (2010).

[116] Ie, Y.; Hirose, T.; Nakamura, H.; Kiguchi, M.; Takagi, N.; Kawai, M.; Aso, Y. *J. Am. Chem. Soc.* **133**, 3014 (2011).

[117] Yeganeh, S.; Galperin, M.; Ratner, M. A. *J. Am. Chem. Soc.* **129**, 13313 (2007).

[118] Aravena, D.; Ruiz, E. *J. Am. Chem. Soc.* **134**, 777 (2012).

[119] Song, H.; Kim, Y.; Jang, Y. H.; Jeong, H.; Reed, M. A.; Lee, T. *Nature* **462**, 1039 (2009).

[120] Sancho, M. P. L.; Sancho, J. M. L.; Rubio, J. *J. Phys. F: Met. Phys.* **14**, 1205 (1984).

[121] Wimmer, M.; Adagideli, I.; Berber, S.; Tománek, D.; Richter, K. *Phys. Rev. Lett.* **93**, 177207 (2008).

[122] An, Y.; Ji, W.; Yang, Z. *J. Phys. Chem. C* 116, 5915 (2012)

[123] Carter, F. L. J. *Vac. Sci. Technol. B* **1983**, 1, 959.

[124] Martin, A. S.; Sambles, J. R.; Ashwell, G. J. *Phys. ReV. Lett.* **1993**, 70, 218.

[125] Kergueris, C.; Bourgoin, J. P.; Palacin, S.; Esteve, D.; Urbina, C.; Magoga, M.; Joachim, C. *Phys. Rev. B***1999**, 59, 12505.

[126] Piva, P. G.; DiLabio, G. A.; Pitters, J. L.; Zikovsky, J.; Rezeq, M.; Dogel, S.; Hofer, W. A.; Wolkow, R. A. *Nature* **2005**, 435, 658.

[127] Blum, A. S.; Kushmerick, J. G.; Long, D.P.,.; Patterson, C. H.; Yang, J.C.,.; Henderson, J. C.; Yao, Y.; Tour, J. M.; Shashidhar, R.; Ratna, B. R. *Nat. Mater.* **2005**, 4, 167.

[128] Law, M.; Greene, L. E.; Johnson, J. C.; Saykally, R.; Yang, P. *Nat. Mater.* **2005**, 4, 455.

[129] Xu, B. Q.; Li, X. L.; Xiao, X. Y.; Sakaguchi, H.; Tao, N. J. *Nano Lett.* **2005**, 5, 1491.

[130] Troisi, A.; Ratner, M. A. *Nano Lett.* **2004**, 4, 59

[131] Matsunaga, N. J. *Comput. Theor. Nanosci.* **2006**, 3, 957.

[132] Hu, M.-S.; Chen, H.-L.; Shen, C.-H.; Hong, L.-S.; Huang, B.-R.; Chen, K.-H.; Chen, L.-C. *Nat. Mater.* **2006**, 5, 102.

[133] Boyen, H.-G.; Ziemann, P.; Wiedwald, U.; Ivanova, V.; Kolb, D. M.; Sakong, S.; Gross, A.; Romanyuk, A.; Buttner, M.; Oelhafen, P. *Nat. Mater.* **2006**, 5, 394.

[134] Lang, N. D.; Kagan, C. R. *Nano Lett.* **2006**, 6, 2955.

[135] Jiang, F.; Zhou, Y. X.; Chen, H.; Note, R.; Mizuseki, H.; Kawazoe, Y. *Phys. ReV. B* **2005**, 72, 155408.

[136] Nitzan, A.; Ratner, M. A. *Science* **2003**, 300, 1384

[137] S. Blundell, Magnetism in Condensed Matter (Oxford University Press, 2001).

[138] Ovchinnikov, A. A. *Theoret. Chim. Acta.* **1978**, 47, 297.

[139] Ovchinnikov, A. A. *Theoret. Chim. Acta.* **1978**, 297.

[140] Shelton, W. A.; Apra, E.; Sumpter, B. G.; Saraiva-Souza, A.; Souza Filho, A. G.; Del Nero, J., Meunier, V. *Am. Chem. Soc.* **2011**, 511, 294.

[141] Brandbyge, M.; Mozos,J.-L.; Ordejon, P.; Taylor, J.; Stokbro, K. *Phys. ReV. B* **2002**, 65, 165401.

[142] Sanchez-Portal, D.; Ordejon, P.; Artacho, E.; Soler, J. *Int. J. Quantum Chem.* **1999**, 65, 453.

[143] Abe, J.; Shirai, Y. *J. Am. Chem. Soc.* 118 (1996) 4705.

[144] Saraiva-Souza, A.; De Melo, C. P.; Peixoto, P.; Del Nero, J. *Opt. Mat.* **2007**, 29, 1010.

[145] Chuvilin, A.; Meyer, C. J.; Algara-Siller, G.; Kaiser, U. *New J. of Phys.* **2009**, 11, 083019.

[146] Son1, Y.-W.; Cohen, M. L.; Louie, S. G. *Nature* **2006**, 444, 347.

[147] Sanvito, S. *Chem. Soc. Rev.***2010**, 40, 3336.

[148] Cardamone, D. M.; Stafford, C. A.; Mazumdar, S. *Nano. Lett.***2006**, 6, 2422.

[149] Stafford, C. A.; Cardamone, D. M.; Mazumdar, S. Nanotechnology **2007**, 18, 424014.